Advances in Civil Engineering

Vulnerability and Reliability Evaluation of Steel and Concrete Structures Under the Action of Strong Earthquakes

Lead Guest Editor: Alfredo Reyes-Salazar
Guest Editors: Sonia E. Ruiz, Edén Bojórquez, Francisco López-Almansa, and Jorge Ruiz-Garcia

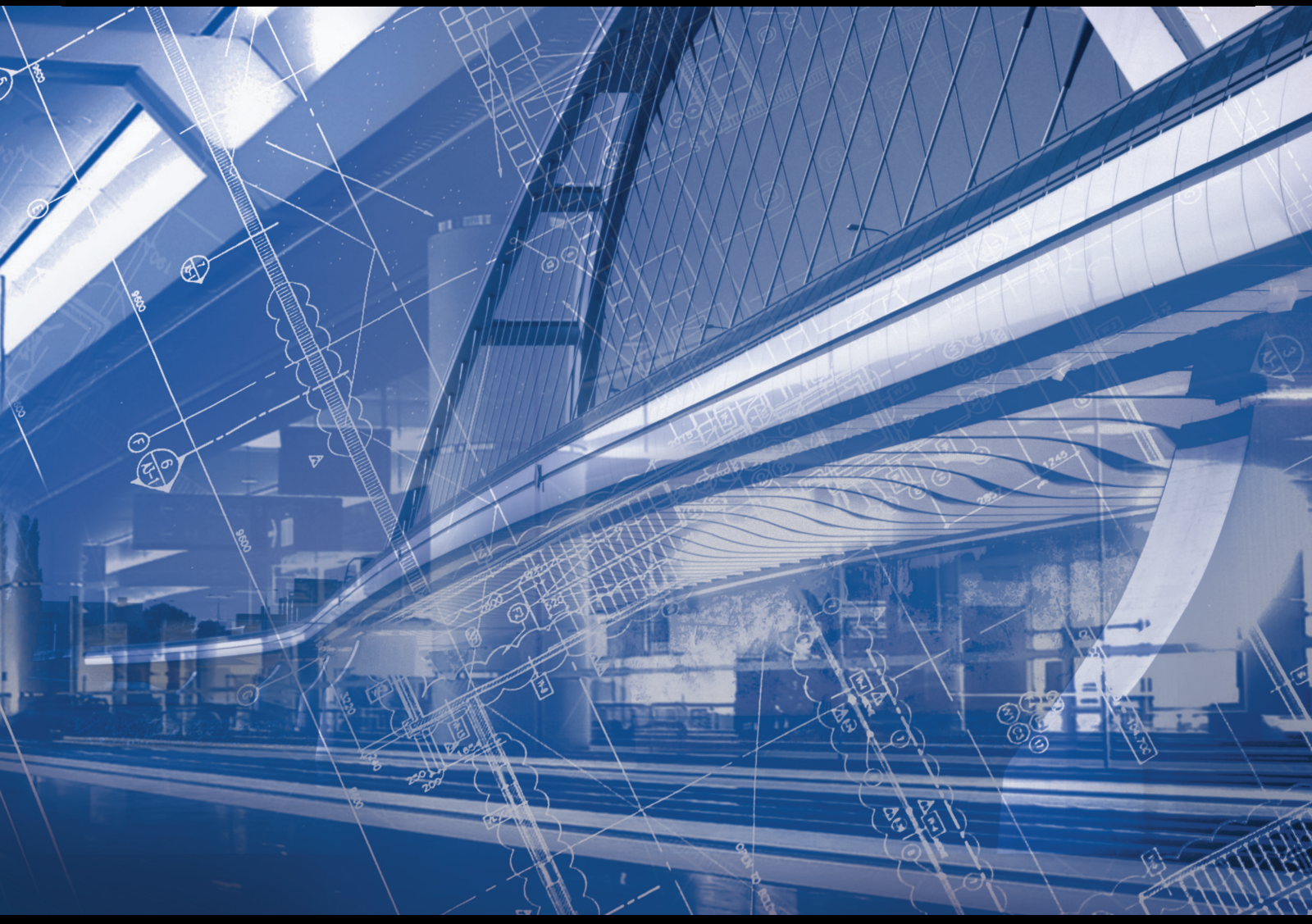

Vulnerability and Reliability Evaluation of Steel and Concrete Structures Under the Action of Strong Earthquakes

Advances in Civil Engineering

Vulnerability and Reliability Evaluation of Steel and Concrete Structures Under the Action of Strong Earthquakes

Lead Guest Editor: Alfredo Reyes-Salazar
Guest Editors: Sonia E. Ruiz, Edén Bojórquez, Francisco López-Almansa, and Jorge Ruiz-Garcia

Contents

Hindawi
Advances in Civil Engineering
Volume 2021, Article ID 2601087, 17 pages
https://doi.org/10.1155/2021/2601087

Research Article

Comparing Hysteretic Energy and Ductility Uniform Annual Failure Rate Spectra for Traditional and a Spectral Shape-Based Intensity Measure

Joel Carvajal,[1] Edén Bojórquez,[1] Sonia Ruiz,[2] Juan Bojórquez,[1] Alfredo Reyes-Salazar,[1] Ali Rodríguez,[2] Mauro Niño,[2] Jorge Ruiz-García,[3] Francisco López-Almansa,[4] and José Torres[1]

[1]*Facultad de Ingeniería, Universidad Autónoma de Sinaloa, Culiacán 80040, Mexico*
[2]*Instituto de Ingeniería, Universidad Nacional Autónoma de México, México 04510, Mexico*
[3]*Facultad de Ingeniería Civil, Universidad Michoacana de San Nicolás de Hidalgo, Morelia 58040, Mexico*
[4]*Architecture Technology Department, Technical University of Catalonia, Barcelona 08028, Spain*

Correspondence should be addressed to Edén Bojórquez; eden@uas.edu.mx and Juan Bojórquez; juanbm@uas.edu.mx

Received 5 October 2021; Revised 10 November 2021; Accepted 12 November 2021; Published 15 December 2021

Academic Editor: Qian Chen

In this study, with the objective to develop a reliability-based seismic design tool, ductility and dissipated hysteretic energy uniform annual failure rate (UAFR) spectra are obtained and compared using the spectral acceleration at first mode of vibration of the structure $Sa(T_1)$ and the well-known spectral shape-based intensity measure I_{Np}. Notice that this is the first time in the literature that UAFR spectra are obtained for the advanced spectral shape intensity measure I_{Np}. For this aim, 110 simulated ground motions recorded from the soft soil of Mexico City were selected due to their large energy amount demanded to the structures; moreover, four elastoplastic hysteretic behavior models are considered for the dynamic analyses with post-yielding stiffness of 0, 3, 5, and 10%. It is observed that the use of elasto-perfectly plastic models provided similar UAFR spectra in comparison with hysteretic models with different post-yielding stiffness. This conclusion is valid for the two selected intensity measures. In addition, the lateral resistance required to achieve similar structural reliability levels is larger when the I_{Np} intensity measure is used, especially for buildings with vibration periods equal or larger than the soil period, in such a way that the traditional use of $Sa(T_1)$ could provide structures with less structural reliability levels.

1. Introduction

One of the main features to design structures subjected to earthquakes is the use of design or response spectra. The spectra provided by the seismic regulations are determined in most of the cases through single-degree-of-freedom (SDOF) systems with elastic behavior subjected to a set of seismic records, which are reduced to account for nonlinear behavior via ductility reduction factors. The current version of Mexico City Building Code (MCBC) and most of the codes around the world use the spectral acceleration at first mode of vibration of the structure $Sa(T_1)$ to estimate the design lateral resistance and stiffness demand of buildings under earthquakes and to control the maximum lateral displacement demand. However, it is known that $Sa(T_1)$ presents some limitations when it is used as intensity measure due to its lack of efficiency to predict the nonlinear structural response [1–4]. For example, $Sa(T_1)$ does not consider the effect of the elongation of the vibration period when nonlinear behavior occurs. For this reason, Bojórquez and Iervolino [5] proposed a spectral shape parameter named N_p and the I_{Np} intensity measure toward more efficient parameters. Several researchers have demonstrated the great potential of the I_{Np} intensity measure [1, 6–11]. In general, the studies have concluded that the most efficient scalar or vector-valued intensity measures are those based on

the N_p spectral shape parameter as in the case of I_{Np}. Thus, it is important to provide new design or response spectra based on more efficient parameters such as I_{Np}. In addition, another two important issues should be accounted for seismic-resistant design of structures. The first one is the inclusion of plastic deformation demands through energy concepts. The use of energy for this purpose was initially discussed by Housner [12]. This concept has been used by various researchers to propose energy-based methodologies aimed to provide the structure with a capacity higher or equal to that demanded by earthquakes [13–20]. In particular, the hysteretic or normalized hysteretic energy has been selected for energy-based design because it is related to the structural damage [21, 22]. On the other hand, the current seismic designs do not take into account explicitly the specific reliability levels in the designed structures. Most of the regulations around the world are mainly based on studies of SDOF systems with elasto-perfectly plastic hysteretic behavior for seismic design of structures, and they do not guarantee the same failure rate on structures as observed in previous studies [23–25]. The seismic design spectra of structures proposed by current codes are not usually associated with specific reliability levels or annual failure rates [26, 27].

This work is motivated by the need to consider the cumulative damage, the structural reliability level, and efficient ground motion intensity measures for earthquake-resistant design of buildings based on the use of uniform annual failure rate spectra. For this reason, in this study ductility and normalized hysteretic energy uniform annual failure rate spectra based on I_{Np} and $Sa(T_1)$ are obtained and compared. To achieve the objectives of this study, nonlinear systems with different post-yielding stiffness, ductility, and normalized hysteretic energy capacities and several structural reliability levels are studied. To compute the uniform annual failure rate spectra, the structures are subjected to 110 simulated narrowband ground motions of the soft soil of the Valley of Mexico, and the results of UAFR spectra are presented for the case of ductility and normalized hysteretic energy. Notice that the study can be expanded using other types of ground motion records, such as those recommended in several works or ground motion selection procedures [28–33]. This study is limited to these seismic records because in order to obtain just one spectrum for a specific intensity measure, ductility value, or hysteretic energy and hysteretic curve, the authors required more than 5 million of nonlinear dynamic analyses, which is a high computational work. In addition, the implications of using simplified models such as the well-known elasto-perfectly plastic behavior to obtain the lateral resistance requirements when the two intensities $Sa(T_1)$ vs. I_{Np} are used are estimated. Finally, it is important to say that this is the first time in the literature that UAFR spectra are obtained for the advanced spectral shape intensity measure I_{Np} toward future energy-based seismic design taken into account the structural reliability.

2. Methodology

2.1. Estimation of UAFR Spectra. The ductility and hysteretic energy UAFR spectra were estimated via the previous works developed by Esteva [34] and Cornell [35] based on the total probability theorem, where the annual failure rate can be defined as next:

$$\nu_F = \int P(Q \geq 1|y) \left| \frac{\mathrm{d}\nu_Y(y)}{\mathrm{d}y} \right| \mathrm{d}y, \tag{1}$$

where $|\mathrm{d}\nu_Y(y)/\mathrm{d}y|$ corresponds to the absolute value of the derivative of the site seismic hazard curve; Q expressed the relationship between demand and capacity; and $P(Q \geq 1|y)$ is the conditional probability of failure given a seismic intensity y. Notice that the structural failure occurs when the capacity is smaller than demand, and in other words: demand/capacity $= Q \geq 1$

The procedure to compute the UAFR spectra is as follows:

(1) Selection of the structural systems

For this study, four elastoplastic-based hysteretic behaviors are considered for the nonlinear models with different post-yielding stiffness ratios. The first single-degree-of-freedom system selected corresponds to the elasto-perfectly plastic hysteretic behavior, and this model can exhibit a linear elastic behavior until a value of strength called yielding point and then behave in a plastic mode until a maximum displacement is obtained. In addition, three elastoplastic models with different post-yielding stiffness ratios corresponding to 3, 5, and 10% have been selected (see Figure 1).

(2) Selection of the simulated earthquake ground motion records

In the seismic design of structures, it is necessary to have seismic records of different magnitudes, and in a sufficient quantity so that it is possible to characterize, in a precise way, the seismic hazard; for this, it is required to identify and take into account all the seismic sources with potential influence in the study site. Unfortunately, the short time of observation and the lack of instrumentation in many regions make it difficult to obtain such records, particularly for large earthquakes. This has motivated the development of several methodologies of seismic simulation to obtain synthetic records of great magnitude earthquakes [36, 37]. In particular, the methods of seismic simulation that use a stochastic summation approach with Green's empirical functions (FGE) are widely accepted in structural engineering, due to their easy application to generate synthetic records. Such methodologies have their origin in 1978 thanks to Hartzell [38].

In this study, it was selected to use the methodology developed by Niño et al. [39]. They propose a source model defined by two corner frequencies and a summation scheme divided into two stages [40, 41], to obtain more accurate spectra to the conditions that affect Mexico City, as well as to improve the definition of the changes

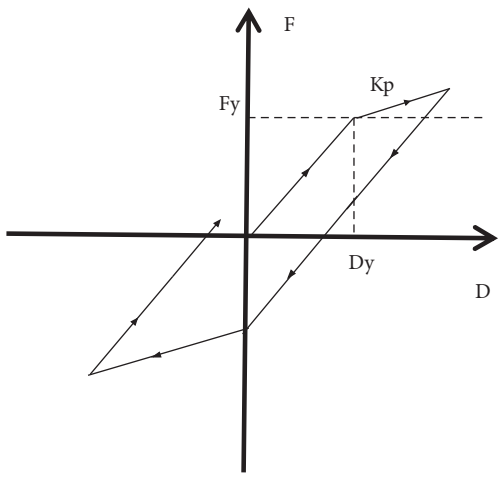

Figure 1: Hysteretic model and cyclic responses of the four analyzed systems, and the nonlinear models correspond to elasto-plastic with post-yielding stiffness $K_p = 0$, 3, 5, and 10%.

in the amplitudes, according to the size of the source and the total duration of the seismic event [42]. With this method, 110 seismic records were simulated for different moment magnitudes M_w from 7.2 to 8.2, with a magnitude increase $\Delta M = 0.1$. For the purpose of this study, the record of the seismic event of April 29, 1989, obtained in the SCT station was used as seed for the simulations; in addition, a stress drop $\Delta\sigma =$ 150 bars was considered. The corresponding parameters of moment of magnitude, M_w, and the two corner frequencies for each stage for the events employed as seed and each of the simulated magnitudes are presented in Table 1.

The average response spectra of the simulated ground motion records are illustrated in Figure 2 for each selected magnitude. Notice the large amplifications of the pseudo-acceleration in a well-defined region of the spectra (1.5–2.5 s). Figure 3 shows the elastic pseudo-acceleration response spectra for all the simulated ground motion records and 5% of damping ratio; moreover, the mean, 25th percentile, and 75th percentile earthquake response spectra also are illustrated.

(3) Selection of the ground motion intensity measures

As it was previously indicated, the most used intensity measure by most of the seismic design codes is the spectral acceleration at first mode of vibration (especially for low-rise structures) [2, 5], because it is the perfect predictor of the response of elastic single-degree-of-freedom systems and multi-degree-of-freedom systems dominated by the first mode of vibration. Nevertheless, $Sa(T_1)$ does not provide information about spectral shape in other regions of the spectrum, which is essential for nonlinear behavior of structures or for which their behavior is dominated by higher modes (modes with periods below than T_1). On the other hand, in recent studies some researchers have proposed parameters to define appropriate intensity measures, which are related to the spectral shape due to its relationship with the structural response.

Recently, following the approach to develop spectral shape parameter as intensity measure, Bojórquez and Iervolino [5] proposed the well-known spectral shape parameter N_p, which takes into account the nonlinear behavior of the structures by including several points of a response spectrum. The N_p spectral shape parameter is defined as the ratio of the geometrical mean between the periods T_1 and T_N $Sa_{avg}(T_1, \ldots, T_N)$ normalized with respect to

Table 1: Magnitudes and corner frequencies for each stage for the seismic events used as seed.

	First stage		Second stage	
M_w	ω_a	ω_b	ω_a	ω_b
7.2	0.2013	3.5899	0.2203	3.9287
7.3	0.1721	3.3353	0.1939	3.7567
7.4	0.1471	3.0987	0.1706	3.5922
7.5	0.1258	2.8789	0.1501	3.4349
7.6	0.1075	2.6747	0.1320	3.2845
7.7	0.0919	2.4850	0.1162	3.1407
7.8	0.0786	2.3088	0.1022	3.0032
7.9	0.0672	2.1450	0.0899	2.8717
8.0	0.0574	1.9929	0.0791	2.7460
8.1	0.0491	1.8515	0.0696	2.6258
8.2	0.0420	1.7202	0.0613	2.5108

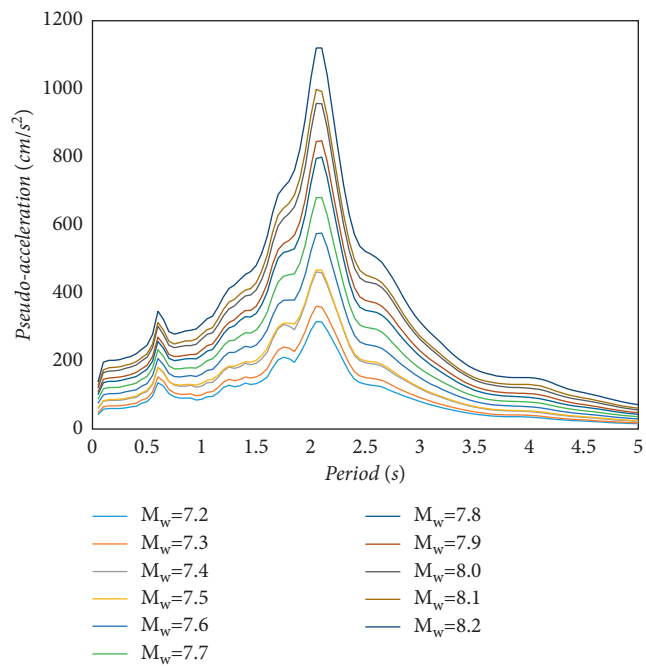

Figure 2: Average response spectra of the selected simulated ground motion records for different moment magnitudes Mw.

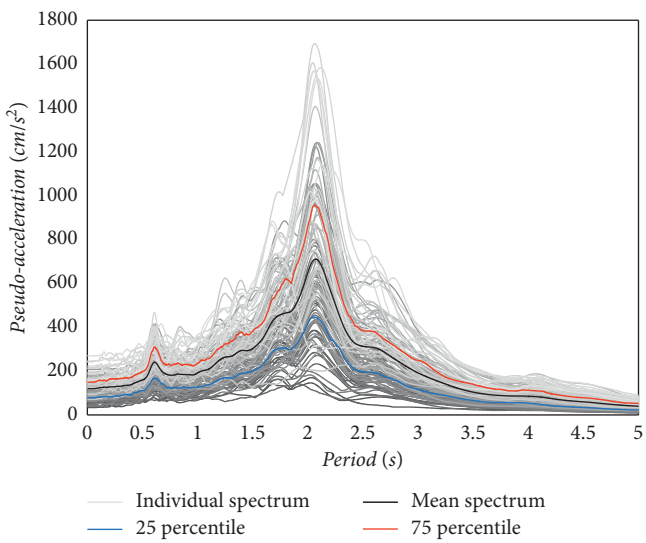

Figure 3: Seismic response spectra of all the selected simulated ground motion records including mean, and 25th and 75th percentiles.

$Sa(T_1)$ as it is illustrated in the following equation:

$$N_p = \frac{Sa_{\text{avg}}(T_1 \ldots T_N)}{Sa(T_1)}. \quad (2)$$

The information given by the N_p equation is that if we have one or n records with a mean N_p value close to one, we can expect an average spectrum near flat in the period range between T_1 and T_N. For a mean N_p lower than one, it is expected an average spectrum with a negative slope, and finally, N_p values larger than one are representative of spectra with positive slope increasing the spectral ordinates.

To incorporate the influence of nonlinear behavior in the prediction of structural response, Bojórquez and Iervolino proposed a new scalar ground motion intensity measure based on $Sa(T_1)$ and N_p, which is described by the following equation:

$$I_{Np} = Sa(T_1) \cdot N_P^{\alpha}. \quad (3)$$

In (3), I_{Np} is a scalar ground motion intensity measure, $Sa(T_1)$ is the commonly known intensity measure, and N_p is the spectral shape parameter, and the α value must be calibrated according to the structure and the selected seismic demand parameter. Different researchers have demonstrated the great potential of the I_{Np} intensity measure [1, 6, 7, 43]. For this reason, in this study, the two selected ground motion intensity measures are $Sa(T_1)$ and I_{Np} to propose new UAFR spectra based on ductility and dissipated hysteretic energy.

(4) Selection of the performance parameters (ductility and hysteretic energy)

In this work, the ductility and normalized hysteretic energy were selected as performance parameters.

Ductility

The ductility is defined as the ability of a system to be deformed without significant loss of resistance. The term ductility factor μ is defined as a measure of the amount of energy dissipation capacity as follows:

$$\mu = \frac{u_{\max}}{u_y}, \quad (4)$$

where $u_{\max}$ is the maximum absolute displacement achieved by the system and u_y is the yielding displacement. For this study, ductility capacity values of 2, 3, and 4 have been selected according to the recommendations of the Mexican City Building Code.

Normalized hysteretic energy

Energy-based methodologies focus on providing structures with energy dissipation capacities larger than or equal to their expected energy demands [13, 14]. The energy most related to the structural damage is the hysteretic energy E_H. The dissipated hysteretic energy can be interpreted physically by considering that it is equal to the area enclosed by each of the hysteresis loops that the structure develops during a seismic excitation. Although hysteretic energy provides an approximate idea of the accumulated plastic deformation demands, this response parameter by itself does not provide sufficient information to evaluate the structural behavior, so it is convenient to normalize it as follows:

$$E_N = \frac{E_H}{F_y \delta_y}, \quad (5)$$

where F_y and δ_y are the strength and displacement at first yield, respectively. E_N is a parameter that correlates best with the structural damage [44, 45]. In this work, the normalized hysteretic energy is considered as a parameter to control the accumulated damage. Thus, E_N UAFR spectra are computed.

(5) Estimation of the structural response of the system by incremental dynamic analysis (IDAs) [46] for a selected period T_1 and yield force coefficient Cy (defined as the yielding force divided by the total weight of the system) subjected to ground motion records scaled in terms of $Sa(T_1)$ or I_{Np}. The seismic responses obtained in this study are the ductility and normalized dissipated hysteretic energy as it was previously discussed.

(6) Proposing specific values of ductility capacity or normalized dissipated hysteretic energy. In this work, the ductility capacity values correspond to those indicated by the Mexico City Building Code. On the other hand, different values for the

normalized hysteretic energy capacity are suggested in Bojórquez et al. [18]. For this reason, in this study the values of 3, 6, 9, and 12 of the normalized hysteretic energy capacity have been selected, which are representative of reinforced concrete and steel buildings according to Terán and Jirsa [21] and Bojórquez et al. [18, 47].

(7) Assessment of the failure probability by dividing the number of ground motion records in which the ductility of energy demanded is larger than the capacity (step 6) between the total numbers of records used for a specific intensity level.

(8) Selection of the seismic hazard curve based on the seismic intensity measures $Sa(T_1)$ and I_{Np}. For the present word, the seismic hazard curves computed by Rodríguez et al. have been used [48, 49].

(9) Numerical assessment of the annual failure rate using (1). The steps for other structural periods and Cy to obtain the structural annual failure rate curves are repeated.

(10) The UAFR spectra for a specific value are calculated for each of the parameters here studied.

Finally, Figure 4 shows a flow chart of the procedure to compute the UAFR spectra.

3. Numerical Results

The numerical results obtained in this work are presented in this section. It is important to say that all the UAFR spectra illustrated correspond to the spectra obtained via the 110 simulated narrowband earthquake ground motions. Notice that the selection of the seismic hazard curves based on the intensity measure $Sa(T_1)$ and I_{Np} is a very important issue to compute the UAFR spectra. The seismic hazard curves are used frequently to represent the seismic hazard of a specific site. They indicate the annual rate of exceeding a variety of intensity levels of a ground motion parameter at a site of interest (i.e., $Sa(T_1)$ and I_{Np}). The procedure to compute a ground motion hazard curve is based on the total probability theorem [34, 35, 50–52]. As it was indicated previously, the seismic hazard curves for $Sa(T_1)$ and I_{Np} developed by Rodríguez et al. 2021 [40, 41] have been selected to compute the uniform annual failure rate spectra. For example, Figure 5 illustrates the seismic hazard curves for the SCT site corresponding to soft soil of Mexico City for periods ranging from 0.2 to 2 seconds and both selected intensity measures.

3.1. Influence of Ductility in the UAFR Spectra in terms of Sa(T1). The ductility UAFR spectra when $Sa(T_1)$ is used as intensity measure and for all the hysteretic models under consideration are illustrated in Figure 6. Furthermore, the UAFR spectra are compared for different ductility capacity levels. While Figure 6(a) shows the results for the elasto-perfectly plastic hysteretic model, Figures 6(b)–6(d) correspond to elastoplastic with 3%, 5%, and 10% of post-yielding stiffness, respectively.

All the spectra are associated with a UAFR $\nu_F = 0.004$. It is observed that as the ductility increases, the required lateral resistance or seismic coefficient (Cy) decreases, especially for structures close to the soil period (Ts = 2s). The largest differences are observed in the intervals of the structural periods ranging from 1.3 to 2 seconds. For example, in Figure 6(a), when $T = 0.8$ seconds (structures with periods smaller than the soil period, which is equal to 2s) and $\mu = 2$, the Cy is equal to 0.25, and for $\mu = 4$, the Cy is equal to 0.21, indicating a reduction of 16% when the ductility increases from 2 to 4. On the other hand, if the structure is close to the soil period, for example, for a system with $T = 1.6$s and $\mu = 2$, the Cy is equal to 0.41 and for $\mu = 4$ the Cy is equal to 0.24. Thus, a reduction of 41.4% is obtained if the ductility capacity increases. Therefore, the structures with vibration period close to the soil period require special attention; in particular, this type of building is more sensitive to the ductility capacity. Similar results are observed for the elastoplastic models with different post-yielding stiffness analyzed in this study as observed in Figures 6(b)–6(d).

3.2. Influence of Post-Yielding Stiffness in the UAFR Spectra in terms of Sa Intensity Measure. The influence of post-yielding stiffness is obtained by comparison of the elasto-perfectly plastic and elastoplastic model with 3% (BL03), 5% (BL05), and 15% (BL15) of post-yielding stiffness. Figures 7 and 8 compare the UAFR spectra with $\nu_F = 0.004$ and $\nu_F = 0.008$ for two different ductility capacities ($\mu = 2$ and $\mu = 4$). The selected ductility values are representative of structures with low and high levels of ductility capacity. It is observed that in both cases, the spectra are similar for all the post-yielding stiffness; therefore, it can be concluded that the post-yielding stiffness has low influence to compute the UAFR spectra, except in the case of structures with period near or about the soil period. For these cases, it is observed that as the post-yielding stiffness increases the seismic coefficient (Cy) decreases in low ratio for structures with moderately low ductility capacity ($\mu = 2$) (see Figures 7(a) and 8(a)). On the other hand, it is shown that for structures with high ductility ($\mu = 4$) (see Figures 7(b) and 8(b)), the effect of post-yielding stiffness in all the analyzed models is more evident. However, the elasto-perfectly plastic hysteretic behavior model provides reasonable results to estimate the required lateral strength in comparison with the elastoplastic model with different post-yielding stiffness.

3.3. Effect of the Annual Failure Rate (ν_F) in the Spectra in terms of Sa Intensity Measure. In this section, the influence of the annual failure rate in the UAFR spectra is studied. For this aim, three failure rates are selected: $\nu_F = 0.008$, $\nu_F = 0.00$, and $\nu_F = 0.0025$, respectively. Figure 9 illustrates for a ductility value equal to 2 and the elasto-perfectly plastic hysteretic model the effect to compute spectra for the selected annual failure rates. It is observed that as the annual failure rate decreases, the seismic coefficient tends to increase, especially for

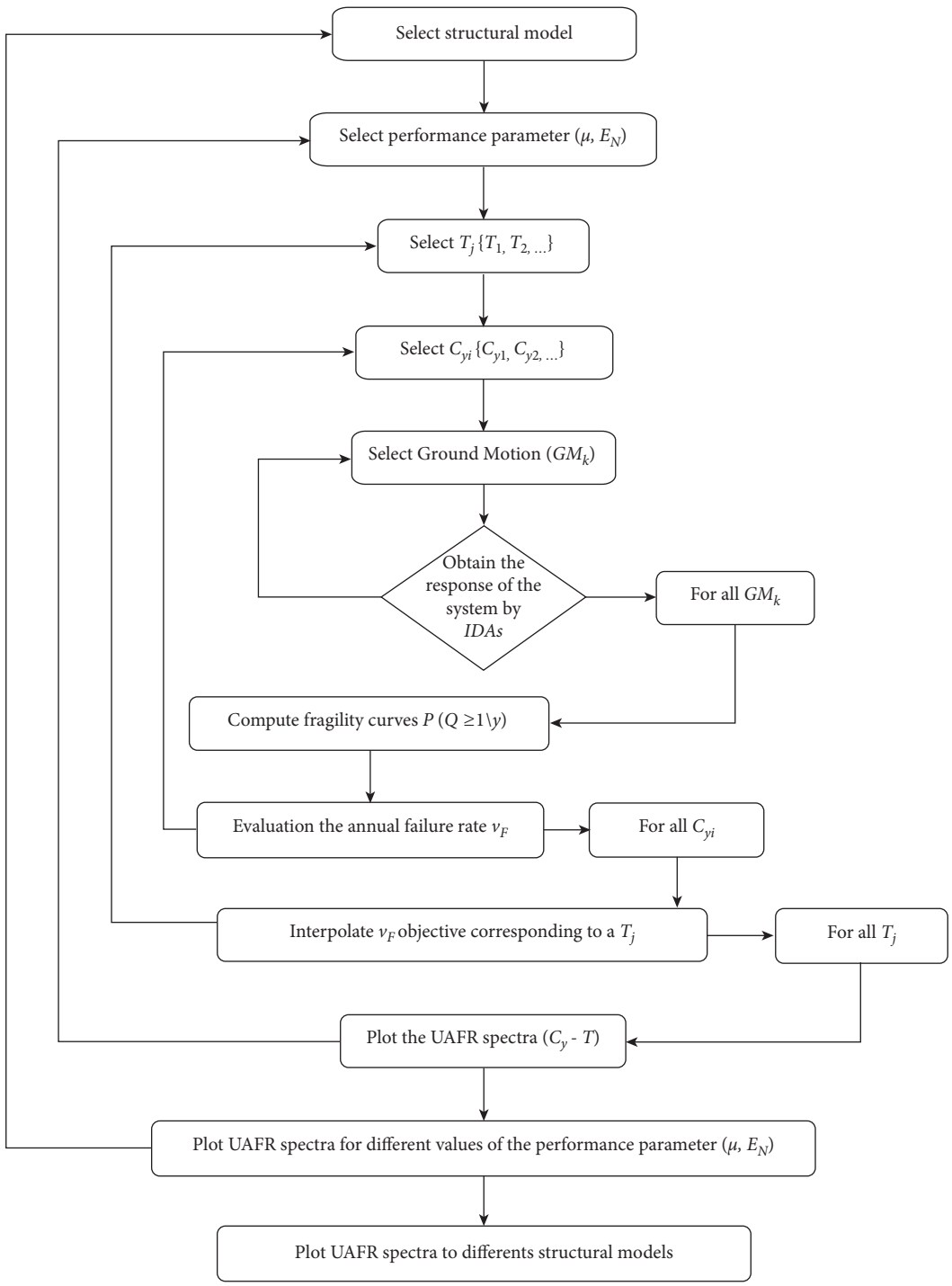

Figure 4: Flow chart of the procedure to compute the UAFR spectra.

structural periods smaller or equal to the soil period. For this reason, if the designed buildings require larger structural reliability levels, it is required to increase the lateral resistance. For example, when $T = 1.0$ seconds with $\nu_F = 0.008$, Cy is equal to 0.20; on the other hand, if $\nu_F = 0.0025$, Cy = 0.33. Therefore, Cy increases about 65%, while for a $T = 3.0$ seconds with $\nu_F = 0.008$, Cy is equal to 0.09 and for $\nu_F = 0.0025$ the Cy = 0.13, and for this case, the percentage is 44.4% larger. In conclusion, it is observed that for structural periods larger or very larger than the soil period, the influence of the uniform annual failure rate selected to compute Cy tends to be despicable.

3.4. Influence of the Hysteretic Energy in the UAFR Spectra in terms of the Sa Intensity Measure. The normalized hysteretic energy UAFR spectra when *Sa* is used as intensity measure for all the models with different post-yielding stiffness under

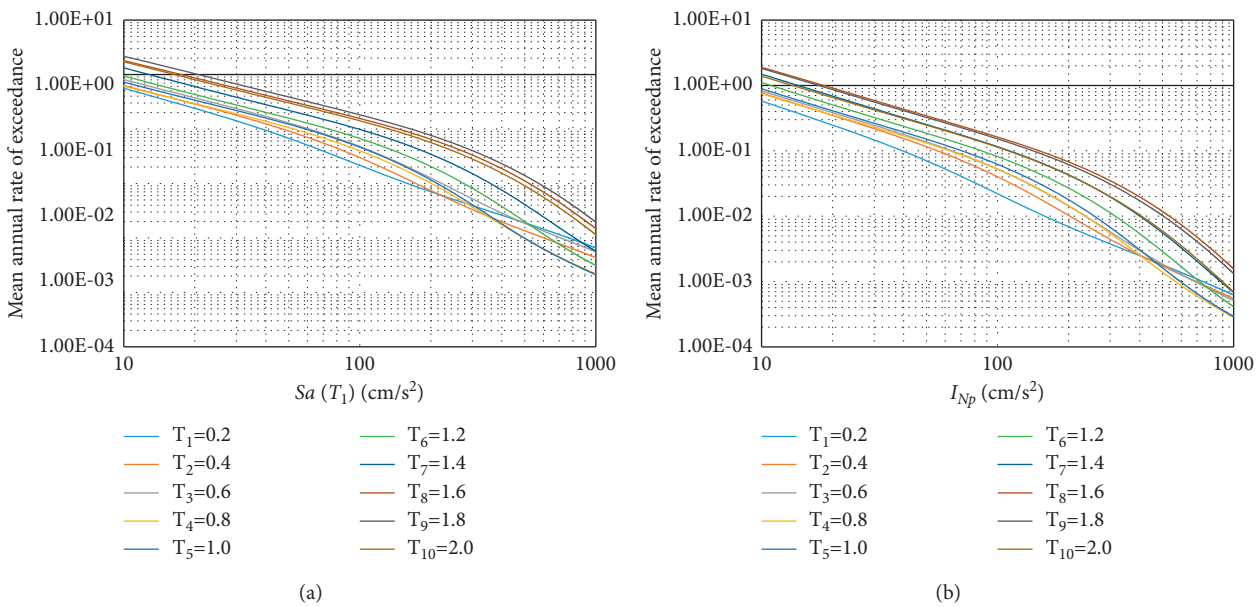

Figure 5: Example of the selected seismic hazard curves for (a) $Sa(T_1)$ and (b) I_{Np}.

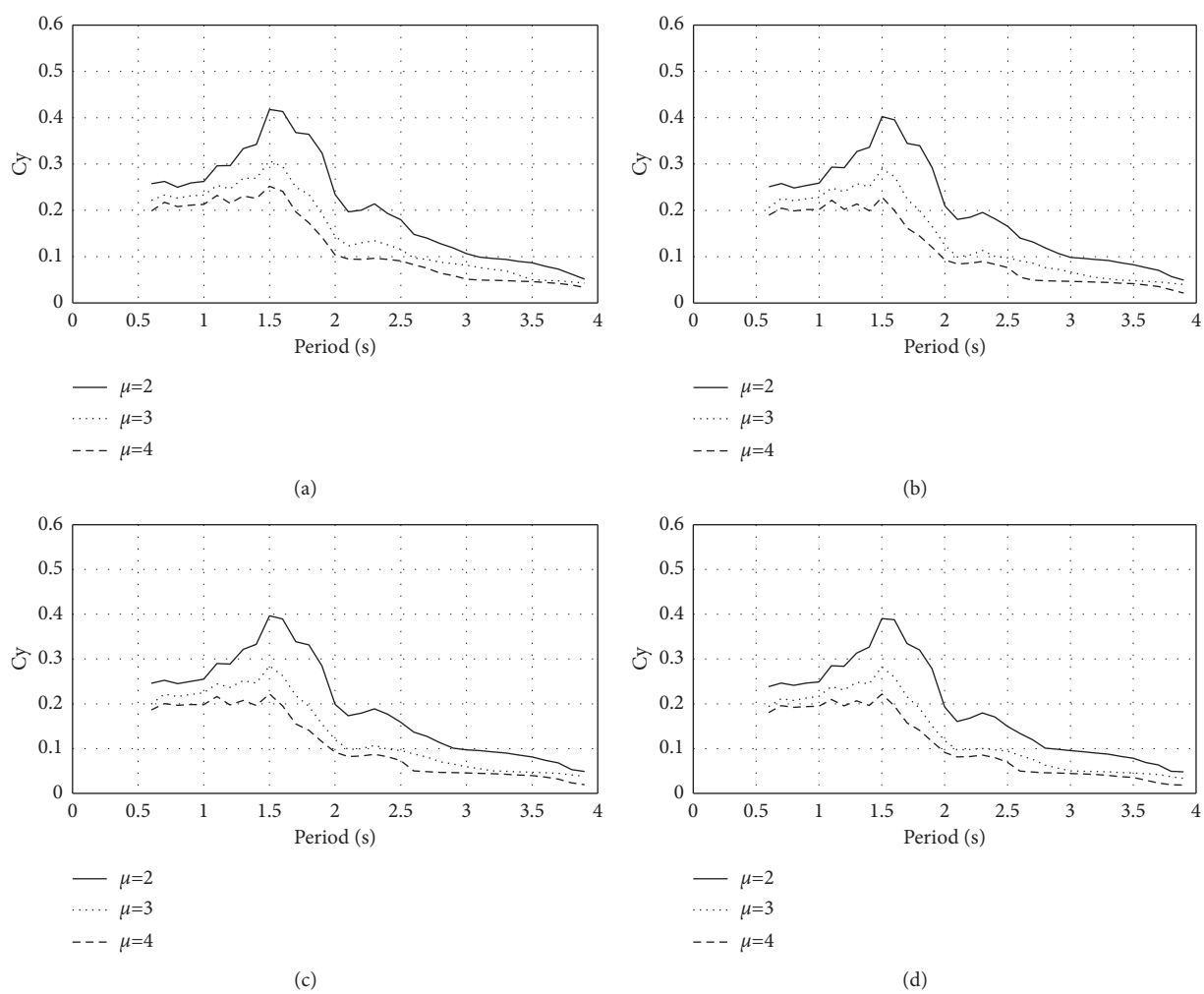

Figure 6: Ductility UAFR spectra for $\nu_F = 0.004$ and the nonlinear hysteretic models: (a) elasto-perfectly plastic and elastoplastic with (b) 3%, (c) 5%, and (d) 10% of post-yielding stiffness.

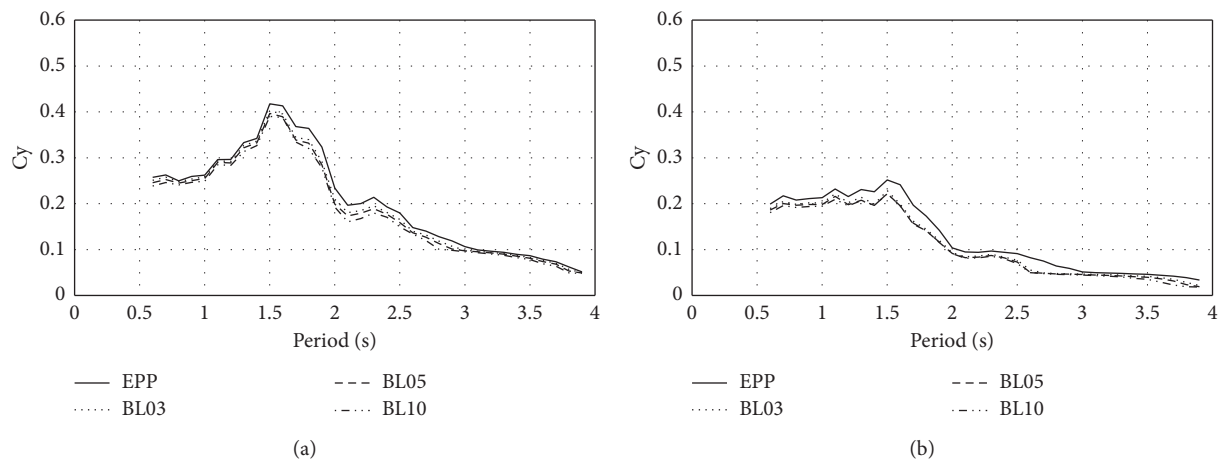

Figure 7: Ductility UAFR spectra with $\nu_F = 0.004$ (250 years of return period) and different levels of post-yielding stiffness. (a) Spectrum for $\mu = 2$. (b) Spectrum for $\mu = 4$.

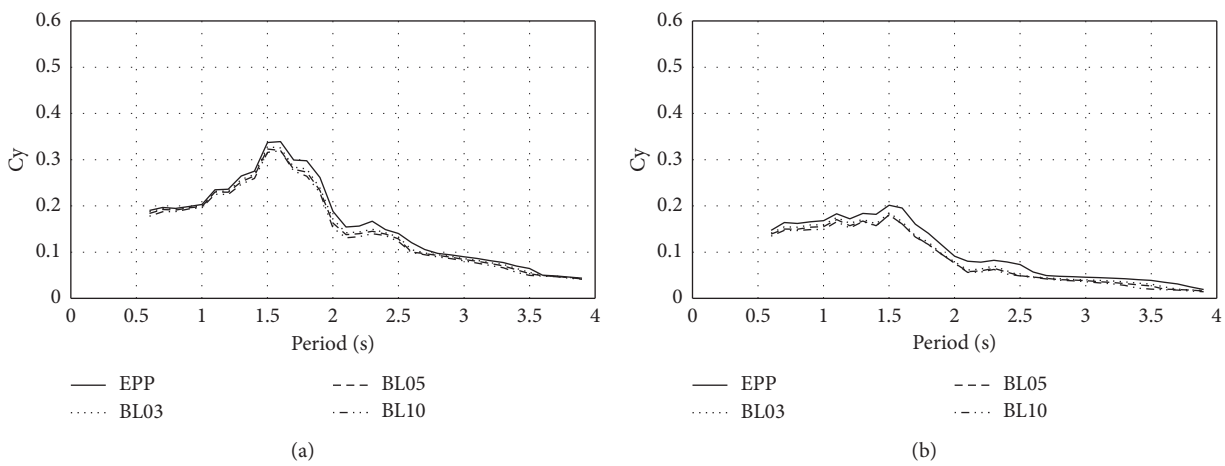

Figure 8: Ductility UAFR spectra with $\nu_F = 0.008$ and different levels of post-yielding stiffness. (a) Spectrum for $\mu = 2$. (b) Spectrum for $\mu = 4$.

consideration are illustrated in Figure 10. The UAFR spectra are compared for different levels of energy capacity for the nonlinear models. Figure 10(a) shows the results for the elasto-perfectly plastic model and Figures 10(b)–10(d) for 3%, 5%, and 10% of post-yielding stiffness. Notice that all the spectra are associated with a UAFR $\nu_F = 0.004$. It is observed that as the energy increases, the required lateral resistance decreases, particularly in the region of periods close to the soil period. The same trend is observed for the different post-yielding stiffness selected in this study.

The influence of post-yielding stiffness on the behavior models in the UAFR spectra is compared in Figures 11 and 12, with $\nu_F = 0.004$ and $\nu_F = 0.008$. It is very interesting to observe that the figures suggest that the UAFR spectra are similar for the different post-yielding stiffness. This conclusion is also valid if the energy capacity selected or annual failure rate is different.

3.5. Effect of Failure Rates in Hysteretic Energy UAFR Spectra in terms of Sa Intensity Measure. In this section, the influence of the annual failure rate in the UAFR spectra in terms of the dissipated hysteretic energy capacity is studied. For this aim, three failure rates are selected: $\nu_{\mathbf{F}} = 0.008$, $\nu_{\mathbf{F}} = 0.004$, and $\nu_{\mathbf{F}} = 0.0025$ respectively; see Figure 13. It is observed that as the failure rates decrease, the required lateral resistance increases. Similar results were found for all the periods under consideration. It is important to say that similar results were obtained when comparing the UAFR spectra in terms of I_{Np} as intensity measure with respect to the previously mentioned parameters. The following section compares the results obtained for Sa and I_{Np} intensity measures.

4. Comparison of Ductility UAFR Spectra: *Sa* vs. I_{Np}

In this part, the results of ductility UAFR spectra for the previously mentioned intensity measures are compared. In Figures 14 and 15, the elasto-perfectly plastic behavior for different ductility values with annual failure rates equal to 0.004 and 0.008 is used to compare the UAFR spectra. Figure 14(a) shows the UAFR spectra for a ductility value equal to 2. It is observed that the lateral resistance required

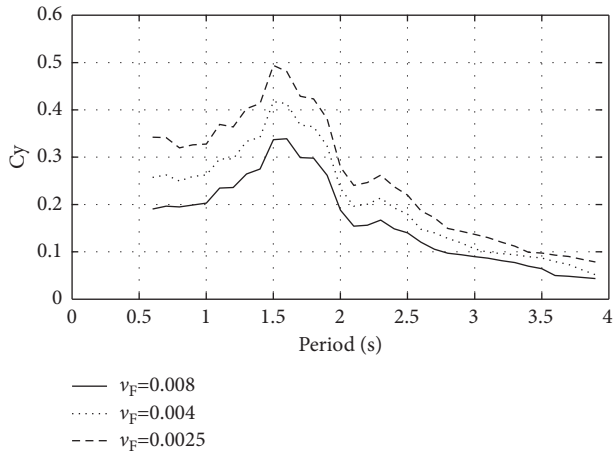

Figure 9: Ductility UAFR spectra for elasto-perfectly plastic model and $\mu = 2$ and three different annual failure rates ($\nu_F = 0.0025$, $\nu_F = 0.004$, and $\nu_F = 0.008$).

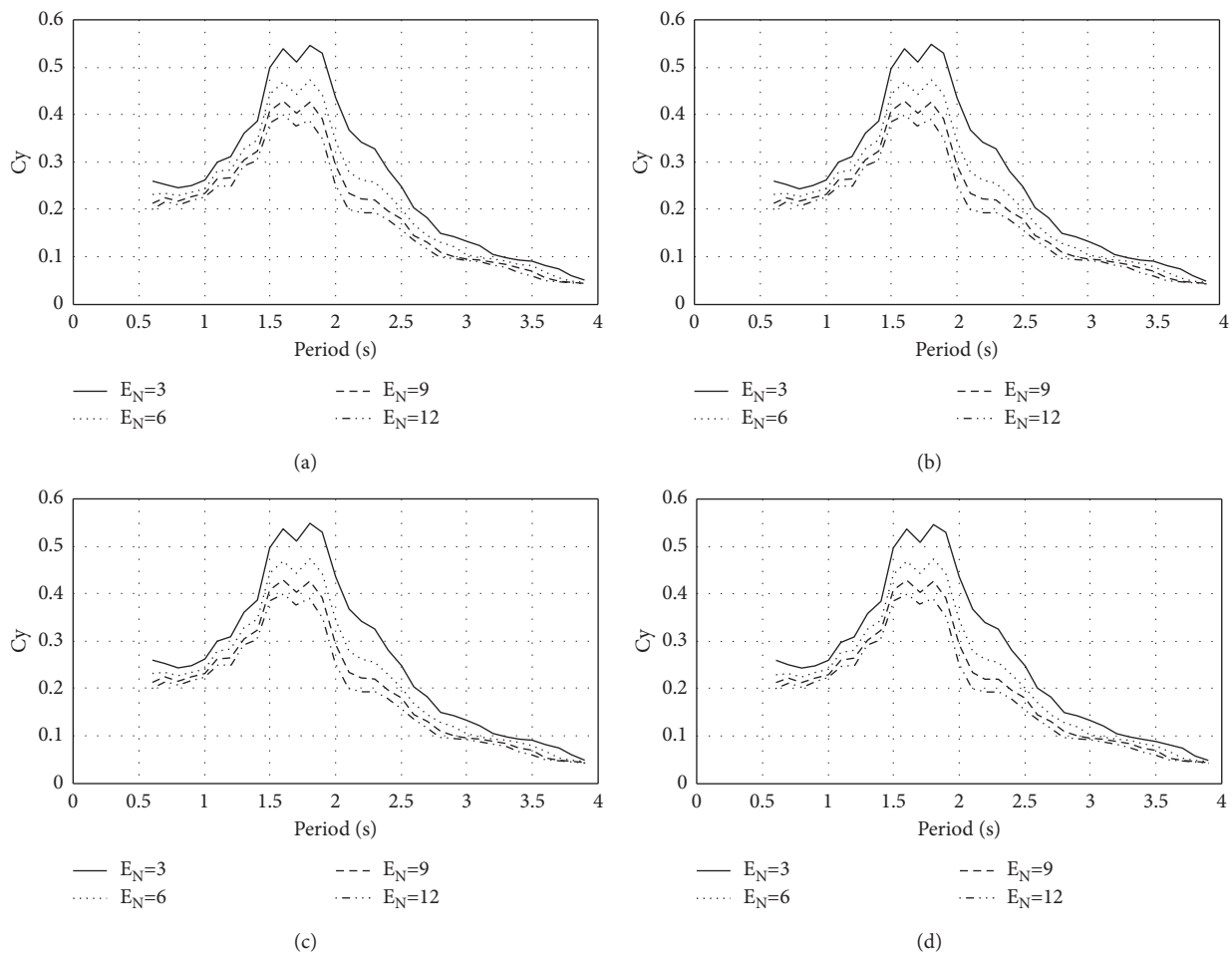

Figure 10: Normalized hysteretic energy UAFR spectra with $\nu_F = 0.004$ for the nonlinear models: (a) elasto-perfectly plastic and elastoplastic with (b) 3%, (c) 5%, and (d) 10% of post-yielding stiffness.

for both intensity parameters is similar for periods less than 1.6 seconds, while for periods between the ranges of 1.6 and 2.5 seconds a significant difference is observed when using both intensity measures selected to compute the lateral resistance required. For example, from Figure 14(a) and a period equal to 1.3 seconds, the values of Cy = 0.31 for I_{Np} and Cy = 0.33 for *Sa* have a difference of 6%, and for a period equal to 2.0 seconds, a Cy = 0.23 is obtained for *Sa* and

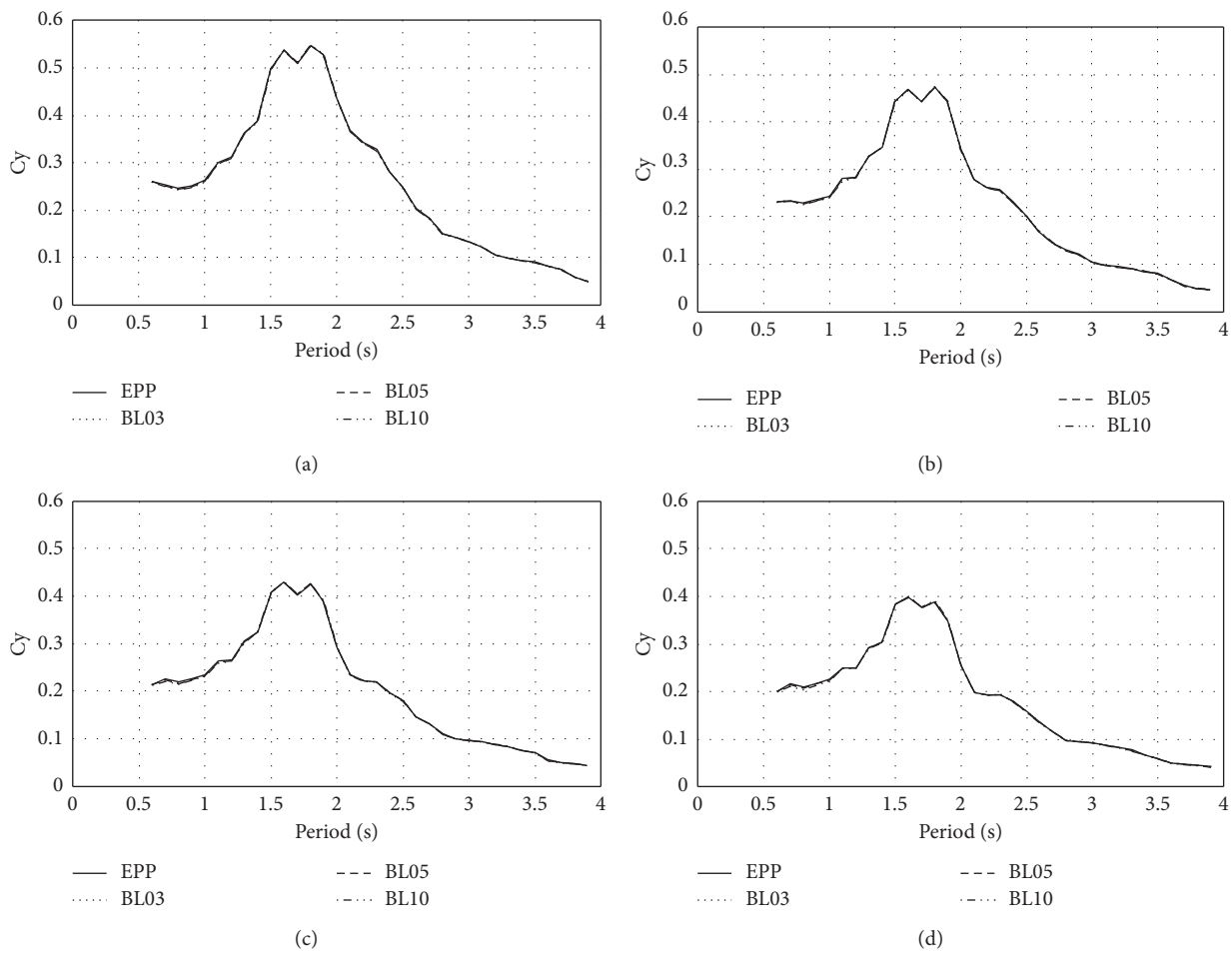

Figure 11: Normalized hysteretic energy UAFR spectra with $\nu_F = 0.004$ and different levels of post-yielding stiffness for (a) $E_N = 3$, (b) $E_N = 6$, (c)$E_N = 9$, and (d)$E_N = 12$.

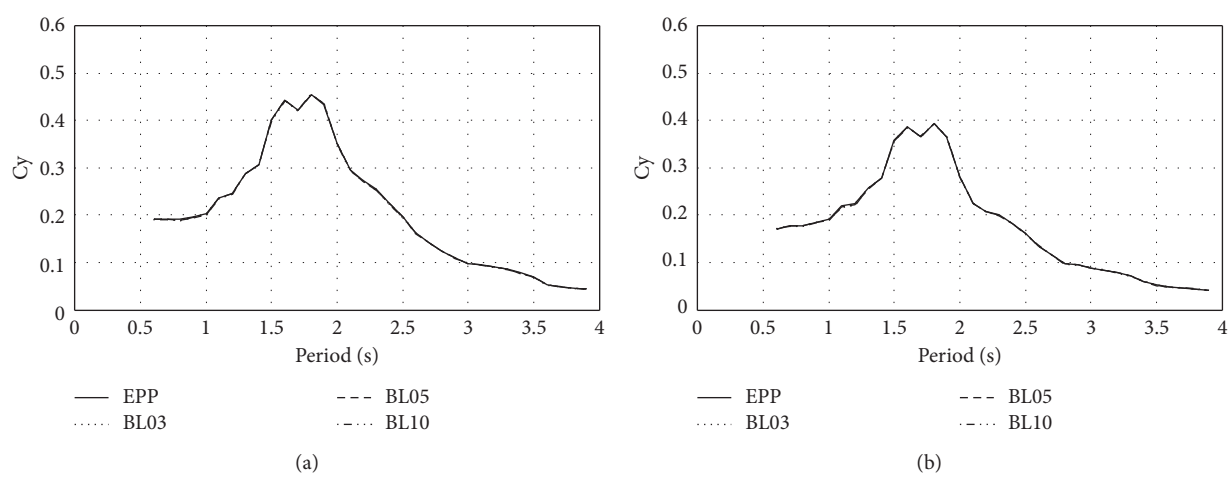

Figure 12: Continued.

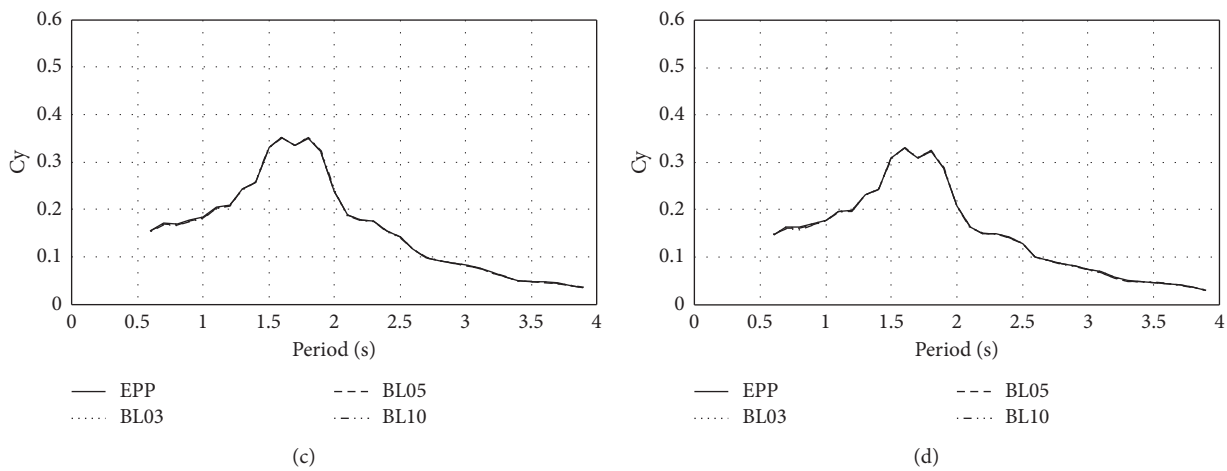

Figure 12: Normalized hysteretic energy UAFR spectra with $\nu_F = 0.008$ and different levels of post-yielding stiffness for (a) $E_N = 3$, (b) $E_N = 6$, (c)$E_N = 9$, and (d)$E_N = 12$.

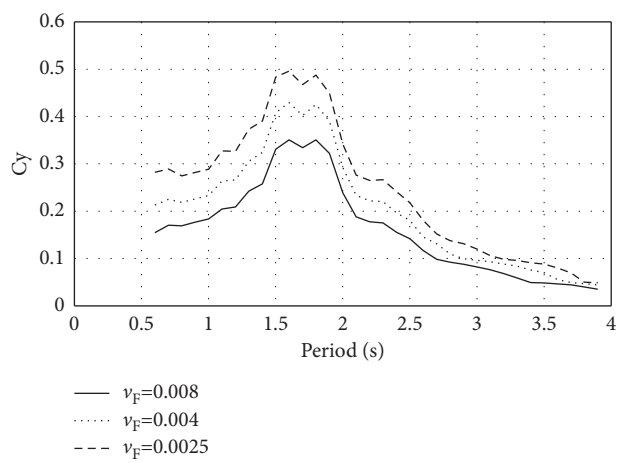

Figure 13: Comparison of normalized hysteretic energy UAFR spectra with $E_N = 9$ for the elasto-perfectly plastic hysteretic model and different annual failure rates.

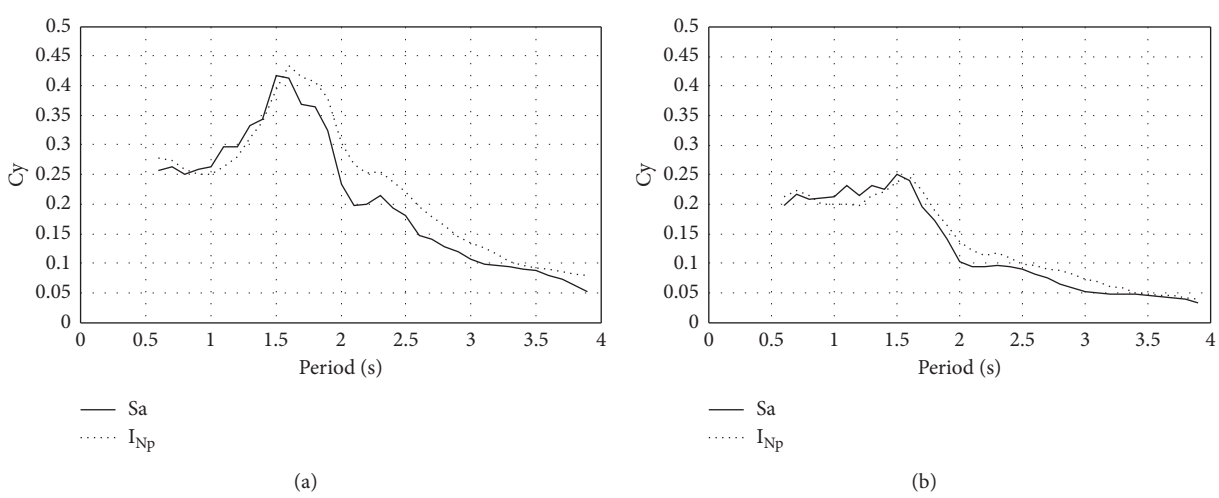

Figure 14: Ductility UAFR spectra for the elasto-perfectly plastic hysteretic model with annual failure rate equal to 0.004 and two different ductility values. (a) Spectrum for $\mu = 2$. (b) Spectrum for $\mu = 4$.

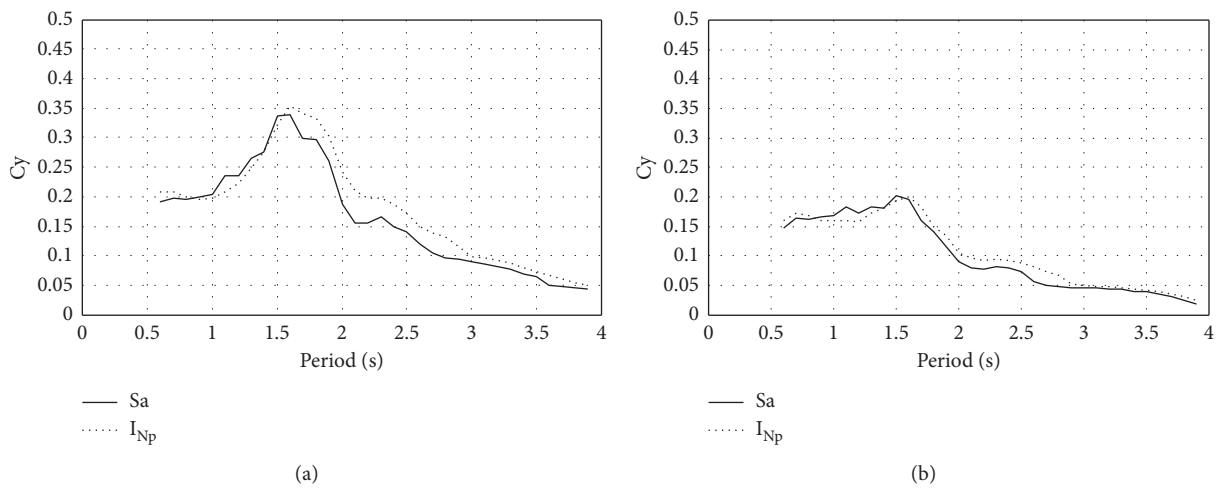

Figure 15: Ductility UAFR spectra for the elasto-perfectly plastic hysteretic model with annual failure rate equal to 0.008 and two different ductility values. (a) Spectrum for $\mu = 2$. (b) Spectrum for $\mu = 4$.

Cy = 0.30 for I_{Np}, and this difference represents about 30%. On the other hand, Figure 14(b) shows the UAFR spectra for ductility equal to 4, where both intensity measures are compared. The results suggest that the value of Cy is very similar for all the periods of the systems under consideration.

The effect of the influence of the ductility value is compared in Figures 14(a) and 14(b). It is found that as the ductility increases, the required lateral resistance decreases considerably for all periods of the systems analyzed in this study, varying from 30% to 60% as the ductility value increases from $\mu = 2$ to $\mu = 4$, respectively. Similar results are found in Figures 15(a) and 15(b) for annual failure rate equal to 0.008. In general, the results suggest that for structures with low ductility capacity such as masonry or reinforced concrete buildings, the selection of an appropriate intensity measure is very important in the case of ductility UAFR spectra at least when several ground motion records are used to compute the average spectrum. It is important to say that the authors will study in future works the importance of efficient intensity measures and the number of records used for nonlinear dynamic analysis to compute the UAFR spectra.

Figures 16 and 17 show the UAFR spectra for ductility values 2 and 4, respectively, where the influence of failure rates ($\nu_F = 0.004$ and $\nu_F = 0.008$) also is compared. It is observed that as the values of the annual failure rate decrease, the required lateral resistance increases up to 30% for structural periods less or equal to the soil period, and the increment is up to 20% higher for periods larger than the soil period. This observation applies for both ground motion intensity measures studied in this work (see Figures 16 and 17).

5. Comparison of Normalized Hysteretic Energy UAFR Spectra: *Sa* vs. I_{Np}

The normalized hysteretic energy UAFR spectra are compared in Figures 18 and 19 for the intensity measures *Sa* and I_{Np} and the elasto-perfectly plastic behavior model with one annual failure rate and different levels of energy capacities. Figures 18(a) and 18(b) show the UAFR spectra associated with annual failure rate equal to 0.004. A similar effect is observed for both intensity measures for the structures with periods less than 1.5 seconds. However, for structural periods between 1.6 and 2.3 seconds (particularly in the region of periods close to the soil period), an important effect is found when using *Sa* or I_{Np}, where the seismic coefficient Cy increases more in the case of I_{Np} compared with *Sa*. This conclusion is valid for the annual failure rate equal to 0.004 and 0.008 (see Figures 18 and 19).

The following figures (Figures 20 and 21) compare the influence of the annual failure rate at different normalized hysteretic energy values. Figures 20 and 21 show the UAFR spectra for E_N equal to 6 and 9, respectively, where the influence of failure rates ($\nu_F = 0.004$ and $\nu_F = 0.008$) is compared. The figures illustrate that as the values of ν_F decrease, the required lateral resistance increases up to 20% for structural periods close to the soil period. Finally, because I_{Np} is a more efficient intensity measure in comparison with the most used intensity measure $Sa(T_1)$, the results indicate that in the case of cumulative demands such as hysteretic energy, the lateral resistance required is larger when an appropriate intensity measure such as I_{Np} is selected. In fact, for example for a structural period equal to 2 (the soil period), the seismic coefficient could be up to 34% larger when using I_{Np} instead of *Sa*. Thus, the use of the intensity measure $Sa(T_1)$ could provide a lateral resistance that produces unsafety structural designs accounting for cumulative plastic deformation demands. In other words, for energy-based design or energy-based spectra it is concluded that I_{Np} should be used as intensity measure. Finally, Figure 22 compares the ratio of the seismic coefficient obtained for the normalized hysteretic energy UAFR spectra in terms of I_{Np} divided by that obtained via the spectral acceleration in the case of the elasto-perfectly plastic model with annual failure rate equal to 0.004 and different values of E_N. This figure confirms that the seismic coefficient could be as larger as 45% when using I_{Np} in comparison with $Sa(T_1)$.

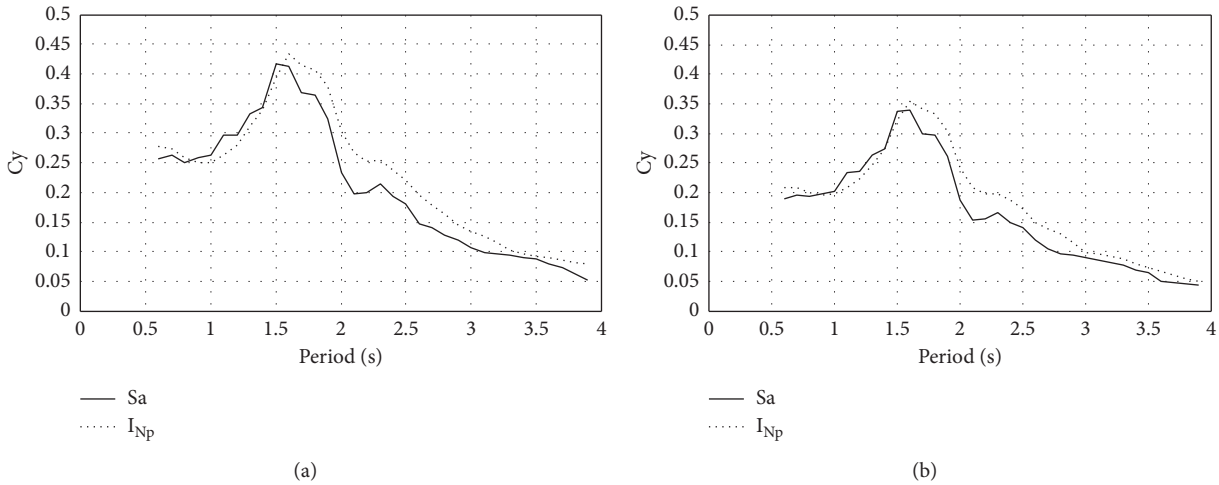

Figure 16: Ductility UAFR spectra for the elasto-perfectly plastic hysteretic model with $\mu = 2$. (a) Spectrum for $\nu_F = 0.004$. (b) Spectrum for $\nu_F = 0.008$.

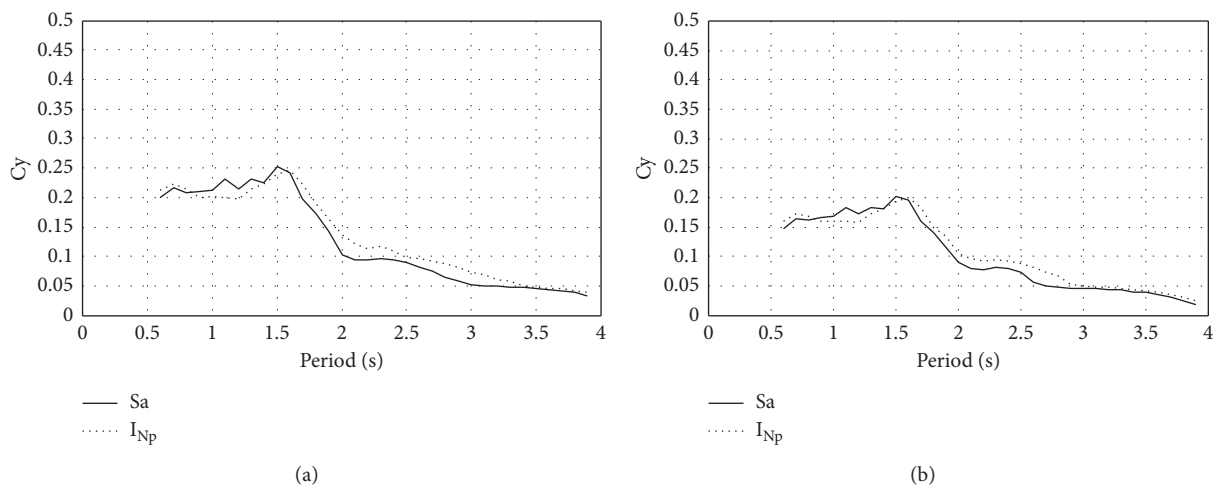

Figure 17: Ductility UAFR spectra for the elasto-perfectly plastic hysteretic model with $\mu = 4$. (a) Spectrum for $\nu_F = 0.004$. (b) Spectrum for $\nu_F = 0.008$.

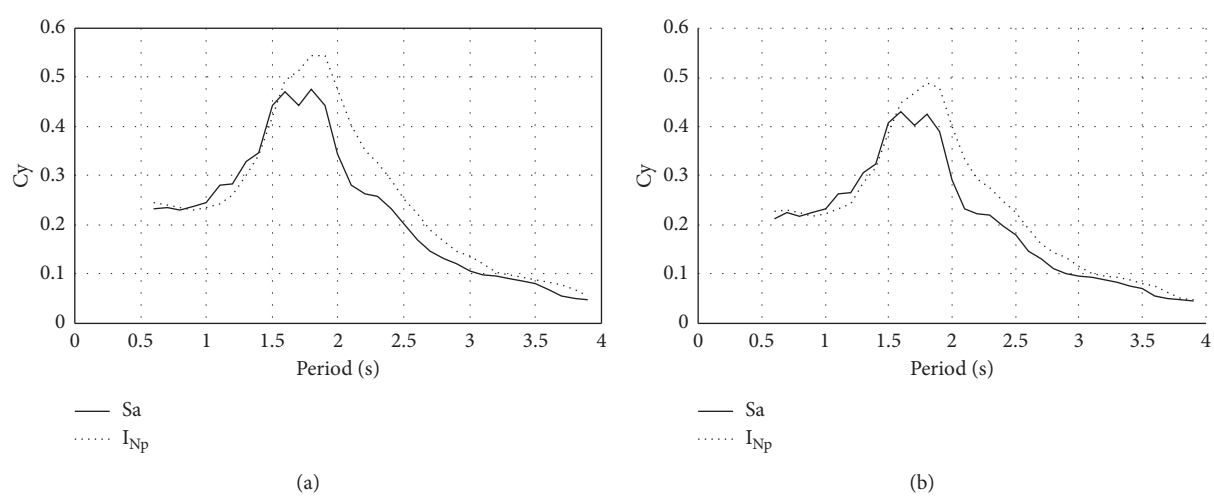

Figure 18: Normalized hysteretic energy UAFR spectra for the elasto-perfectly plastic model with annual failure rate equal to 0.004 and two values of E_N. (a) Spectrum for $E_N = 6$. (b) Spectrum for $E_N = 9$.

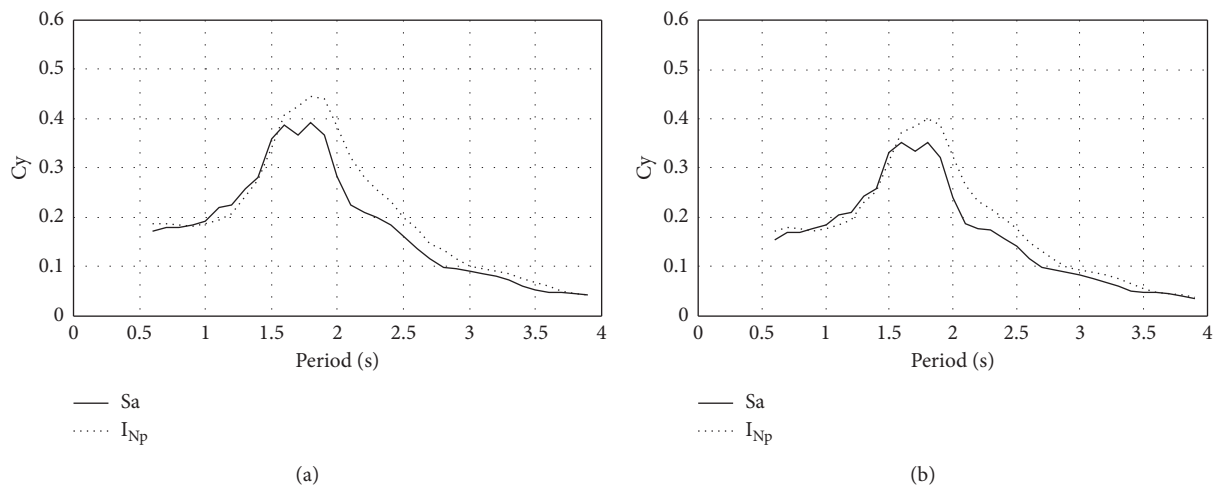

Figure 19: Normalized hysteretic energy UAFR spectra for the elasto-perfectly plastic model with annual failure rate equal to 0.008 and two values of E_N. (a) Spectrum for $E_N = 6$. (b) Spectrum for $E_N = 9$.

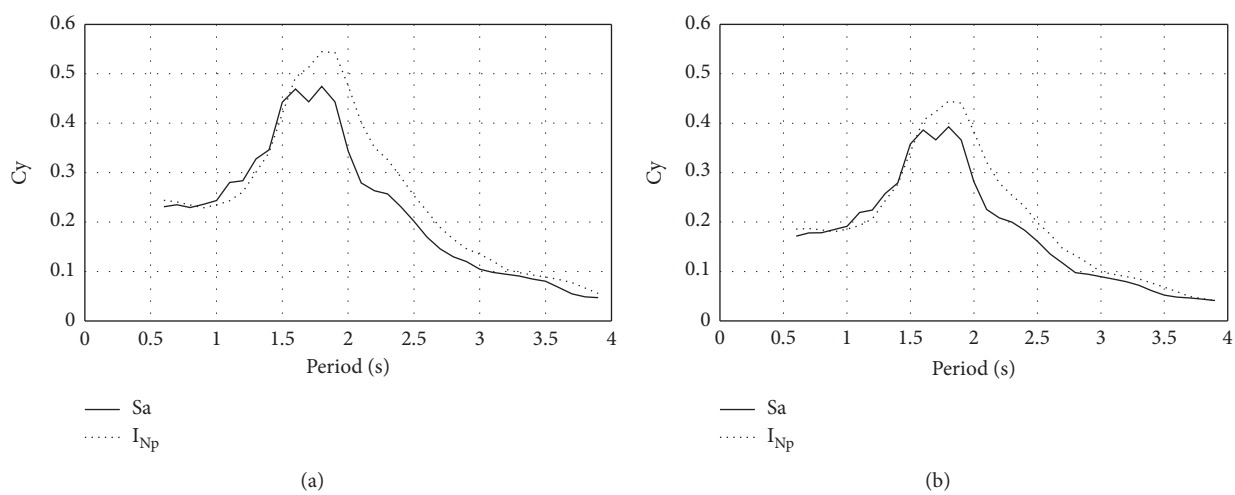

Figure 20: Normalized hysteretic energy UAFR spectra for the elasto-perfectly plastic model with $E_N = 6$. (a) Spectrum for $\nu_F = 0.004$. (b) Spectrum for $\nu_F = 0.008$.

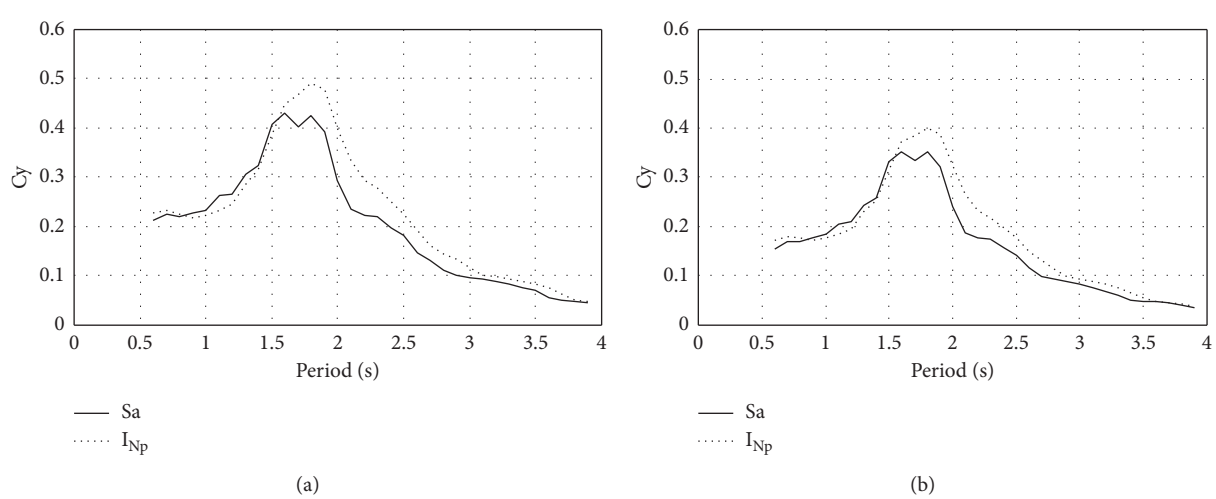

Figure 21: Normalized hysteretic energy UAFR spectra for the elasto-perfectly plastic model with $E_N = 9$. (a) Spectrum for $\nu_F = 0.004$. (b) Spectrum for $\nu_F = 0.008$.

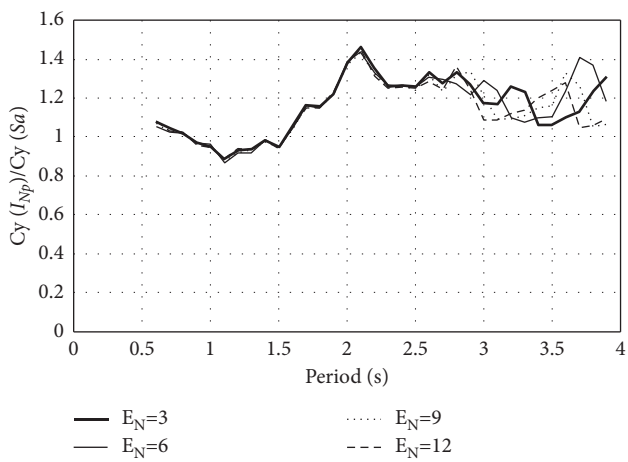

Figure 22: Ratio of Cy (I_{Np}) divided by Cy (Sa) for the normalized hysteretic energy UAFR spectra for the elasto-perfectly plastic model with annual failure rate equal to 0.004 and different values of E_N.

6. Conclusions

In this study, ductility and dissipated hysteretic energy UAFR spectra have been computed and compared using spectral acceleration at first mode of vibration and the well-known I_{Np} intensity measures. The results obtained for ductility and hysteretic energy UAFR spectra are as follows.

6.1. Ductility.

(i) The ductility UAFR spectra when Sa and I_{Np} are used as intensity measures were computed. It was observed that as the ductility increases, the required lateral resistance decreases, where the largest differences occurred for structures close to the soil period. Therefore, the structures with vibration period close to the soil period require special attention; in particular, this type of building is more sensitive to the ductility capacity.

(ii) The influence of post-yielding stiffness also is analyzed. It was observed that the ductility spectra are very similar for the selected hysteretic models with different post-yielding stiffness, in such a way that the elasto-perfectly plastic behavior model can give reasonable results for estimating the Cy with bilinear behavior and different percentages of post-yielding stiffness.

(iii) In the case of the influence of the annual failure rate in the UAFR spectra, it was found that as the annual failure rates are reduced, the Cy increases in a reasonable rate. For this reason, if the designed buildings require larger structural reliability levels, it is necessary to increase the required lateral resistance.

(iv) Finally, for the case of ductility UAFR spectra, the results suggest that for structures with low ductility capacity such as masonry or reinforced concrete buildings, the selection of an appropriate intensity measure is very important at least when several ground motion records are used to compute the average spectrum.

6.2. Normalized Hysteretic Energy.

(i) For the case of normalized hysteretic energy UAFR spectra and both intensity measures used, it is concluded that as the E_N increases, the required lateral resistance decreases, particularly in the region of periods close or larger to the soil period. Notice that the same trend is observed for all the selected post-yielding stiffness under consideration.

(ii) As in the case of ductility, no influence of the post-yielding stiffness was observed to compute the average normalized hysteretic energy UAFR spectra.

(iii) As it was expected, as the annual failure rate decreases (structures with large reliability levels) the required lateral resistance increases.

(iv) Finally, the use of the intensity measure $Sa(T_1)$ could provide a lateral resistance that produces unsafety structural designs accounting for cumulative plastic deformation demands. In other words, for energy-based design or energy-based spectra it is concluded that I_{Np} should be used as intensity measure.

Data Availability

The data used to support the findings of this study are available from the corresponding authors upon request.

Conflicts of Interest

The authors declare that there are no conflicts of interest regarding the publication of this study.

Acknowledgments

The financial support given by the Universidad Autónoma de Sinaloa under Grant PROFAPI 2022 is appreciated. The authors express their gratitude to the Consejo Nacional de Ciencia y Tecnología (CONACYT) in Mexico for funding the research reported in this study under Grant Ciencia Básica 287103 and for the scholarships given to the PhD students. The support of the UNAM-DGAPA-PAPIIT under Project No. IN100320 is appreciated.

References

[1] N. Buratti, "A comparison of the performances of various ground-motion intensity measures," in *Proceedings of the the 15th World Conference on Earthquake Engineering*, pp. 24–28, Lisbon, Portugal, September, 2012.

[2] E. Bojórquez, I. Iervolino, A. Reyes-Salazar, and S. E. Ruiz, "Comparing vector-valued intensity measures for fragility analysis of steel frames in the case of narrow-band ground motions," *Engineering Structures*, vol. 45, pp. 472–480, 2012.

[3] M. De Biasio, S. Grange, F. Dufour, F. Allain, and I. Petre-Lazar, "A simple and efficient intensity measure to account for nonlinear structural behavior," *Earthquake Spectra*, vol. 30, no. 4, pp. 1403–1426, 2014.

[4] M. Kohrangi, S. R. Kotha, and P. Bazzurro, "Ground-motion models for average spectral acceleration in a period range: direct and indirect methods," *Bulletin of Earthquake Engineering*, vol. 16, no. 1, pp. 45–65, 2017.

[5] E. Bojórquez and I. Iervolino, "Spectral shape proxies and nonlinear structural response," *Soil Dynamics and Earthquake Engineering*, vol. 31, no. 7, pp. 996–1008, 2011.

[6] N. Buratti, *Confronto tra le performance di diverse misure di intensitá dello scuotimento sísmico*, Congreso Nacional de Ingeniería de Italia, ANIDIS, Pisa, Italia, 2011.

[7] A. Modica and P. J. Stafford, "Vector fragility surfaces for reinforced concrete frames in Europe," *Bulletin of Earthquake Engineering*, vol. 12, no. 4, pp. 1725–1753, 2014.

[8] M. Yakhchalian, A. Nicknam, and G. G. Amiri, "Optimal vector-valued intensity measure for seismic collapse assessment of structures," *Earthquake Engineering and Engineering Vibration*, vol. 14, no. 1, pp. 37–54, 2015.

[9] K. Kostinakis and A. Athanatopoulou, "Incremental dynamic analysis applied to assessment of structure-specific earthquake IMs in 3D R/C buildings," *Engineering Structures*, vol. 125, pp. 300–312, 2016.

[10] H. R. Jamshidiha, M. Yakhchalian, and B. Mohebi, "Advanced scalar intensity measures for collapse capacity prediction of steel moment resisting frames with fluid viscous dampers," *Soil Dynamics and Earthquake Engineering*, vol. 109, pp. 102–118, 2018.

[11] S. Minas and C. Galasso, "Accounting for spectral shape in simplified fragility analysis of case-study reinforced concrete frames," *Soil Dynamics and Earthquake Engineering*, vol. 119, pp. 91–103, 2019.

[12] G. W. Housner, "Limit design of structures to resist earthquakes," in *Proceedings of the First World Conference on Earthquake Engineering*, Berkeley, CA, USA, June, 1956.

[13] H. Akiyama, *Earthquake-Resistant Limit-State Design for Buildings*, University of Tokyo Press, Tokyo, Japan, 1985.

[14] C.-M. Uang and V. V. Bertero, "Evaluation of seismic energy in structures," *Earthquake Engineering & Structural Dynamics*, vol. 19, no. 1, pp. 77–90, 1990.

[15] B. Akbas, J. Shen, and H. Hao, "Energy appproach in peformance-based seismic design of steel moment resisting frames for basic safety objective," *The Structural Design of Tall Buildings*, vol. 10, no. 3, pp. 193–217, 2001.

[16] L. D. Decanini and F. Mollaioli, "An energy-based methodology for the assessment of seismic demand," *Soil Dynamics and Earthquake Engineering*, vol. 21, no. 2, pp. 113–137, 2001.

[17] H. Choi and J. Kim, "Energy-based seismic design of buckling-restrained braced frames using hysteretic energy spectrum," *Engineering Structures*, vol. 28, no. 2, pp. 304–311, 2006.

[18] E. Bojórquez, A. Reyes-Salazar, A. Terán-Gilmore, and S. E. Ruiz, "Energy-based damage index for steel structures," *Steel and Composite Structures*, vol. 10, pp. 331–348, 2009.

[19] Y. Lieping, C. Guangy, and Q. Zhe, "Study on energy-based seismic design method and the application for steel braced frame structures," in *Proceedings of the Sixth International Conference on Urban Earthquake Engineering*, Tokyo Institute of Technology, Tokyo, Japan, March, 2009.

[20] M. G. Mezgebo and E. M. Lui, "A new methodology for energy-based seismic design of steel moment frames," *Earthquake Engineering and Engineering Vibration*, vol. 16, no. 1, pp. 131–152, 2017.

[21] A. Teran-Gilmore and J. O. Jirsa, "Energy demands for seismic design against low-cycle fatigue," *Earthquake Engineering & Structural Dynamics*, vol. 36, no. 3, pp. 383–404, 2007.

[22] E. Bojorquez, S. E. Ruiz, and A. Teran-Gilmore, "Reliability-based evaluation of steel structures using energy concepts," *Engineering Structures*, vol. 30, no. 6, pp. 1745–1759, 2008.

[23] T. Inoue and C. A. Cornell, "Seismic hazard analysis of MDOF structures," in *Proceedings of the International Conference on Acoustics, Speech and Signal Processing 6*, vol. 1, pp. 437–444, Ciudad de México, México, April, 1991.

[24] L. Esteva, S. E. Ruiz, and J. L. Rivera, "Reliability and performance-based design of structures with energy-dissipating devices," in *Proceedings of the 9th World Seminar on Seismic Isolation, Energy Dissipation and Active Vibration Control of Structures*, Kobe, Japan, June 2005.

[25] E. Bojorquez, J. Bojorquez, S. E. Ruiz, A. Reyes-Salazar, and J. Velazquez-Dimas, "Response transformation factors for deterministic-based and reliability-based seismic design," *Structural Engineering and Mechanics*, vol. 46, pp. 755–773, 2013.

[26] Y. K. Wen, "Building reliability and code calibration," *Earthquake Spectra*, vol. 11, no. 2, pp. 269–296, 1995.

[27] C. A. Cornell, "Reliability-based earthquake-resistant design: the future," in *Proceedings of the 11th World Conference on Earthquake Engineering, Balkema Rotterdam*, Acapulco, Mexico, June 1992.

[28] F. Naeim, A. Alimoradi, and S. Pezeshk, "Selection and scaling of ground motion time histories for structural design using genetic algorithms," *Earthquake Spectra*, vol. 20, no. 2, pp. 413–426, 2004.

[29] X. Ye and D. Wang, "Selection of real earthquake accelerograms for structural dynamic analysis and energy evaluation," *Science China Technological Sciences*, vol. 54, no. 11, pp. 2878–2885, 2011.

[30] I. Iervolino, C. Galasso, R. Paolucci, and F. Pacor, "Engineering ground motion record selection in the Italian accelerometric archive," *Bulletin of Earthquake Engineering*, vol. 9, no. 6, pp. 1761–1778, 2011.

[31] E. Bojórquez, A. Reyes-Salazar, S. E. Ruiz, and J. Bojórquez, "A new spectral shape-based record selection approach using and genetic algorithms," *Mathematical Problems in Engineering*, vol. 2013, Article ID 679026, 9 pages, 2013.

[32] R. K. Mohammadi, M. Mirtaheri, M. Salkhordeh, E. Mosaffa, G. Mahdavi, and M. A. H. Ardebili, "Seismic mitigation of substation cable connected equipment using friction pendulum systems," *Structural Engineering & Mechanics*, vol. 72, no. 6, pp. 785–796, 2019.

[33] M. Salkhordeh, E. Govahi, and M. Mirtaheri, "Seismic fragility evaluation of various mitigation strategies proposed for bridge piers," *Structure*, vol. 33, pp. 1892–1905, 2021.

[34] L. Esteva, "Criterios para la construcción de espectros para diseño por sismo," in *Boletín del Instituto de Materiales y Modelos Estructurales*Universidad Central de Venezuela, Caracas, Venezuela, 1967.

[35] C. A. Cornell, "Engineering seismic risk analysis," *Bulletin of the Seismological Society of America*, vol. 58, no. 5, pp. 1583–1606, 1968.

[36] S. H. Hartzell, "Simulation of ground accelerations for may 1980 mammoth lakes California earthquakes," *Bulletin of the Seismological Society of America*, vol. 72, pp. 2381–2387, 1982.

[37] K. Irikura, *Semi-Empirical Estimation of Strong Ground Motions During Large Earthquakes*, Bulletin of the Disaster Prevention Research Institute, Kyoto, Japan, 1983.

[38] S. H. Hartzell, "Earthquake aftershocks as Green functions," *Geophysical Research Letters*, vol. 5, pp. 1–4, 1978.
[39] M. Niño, G. Ayala, and M. Ordaz, "Ground-motion simulation by the empirical Green's function method with a source defined by two corner frequencies and a two-stage summation scheme," *Bulletin of the Seismological Society of America*, vol. 108, no. 2, pp. 901–912, 2018.
[40] M. Ordaz, J. Arboleda, and K. Singh, "A scheme of random summation of an empirical Green's function to estimate ground motions from future large earthquake," *Bulletin of the Seismological Society of America*, vol. 85, pp. 1635–1647, 1995.
[41] D. García, K. Singh, M. Herraiz, F. Pacheco, and M. Ordaz, "Inslab earthquakes of central Mexico: Q, source spectra and stress drop," *Bulletin of the Seismological Society of America*, vol. 94, no. 3, pp. 789–802, 2004.
[42] R. J. Archuleta and C. Ji, "Moment rate scaling for earthquakes 3.3≤ M ≤5.3 with implications for stress drop," *Geophysical Research Letters*, vol. 43, no. 12, pp. 4–12, 2016.
[43] E. Javadi and M. Yakhchalian, "Selection of optimal intensity measure for seismic assessment of steel buckling restrained braced frames under near-fault ground motions," *Journal of Rehabilitation in Civil Engineering*, vol. 7-4, pp. 1–20, 2018.
[44] H. Krawinkler and A. Nassar, "Seismic design based on ductility and cumulative damage demands and capacities," in *Nonlinear Seismic Analysis and Design of Reinforced Concrete Buildings*, H. Krawinkler and P. Fajfar, Eds., Elsevier Applied Science, London, U.K., 1992.
[45] A. Teran-Gilmore and R. Simon, "Use of constant cumulative ductility spectra for performance-based seismic design of ductile frames," in *Proceedings of the 8th U.S. National Conference on Earthquake Engineering*, San Francisco, CA, USA, April 2006.
[46] D. Vamvatsikos and C. A. Cornell, "Incremental dynamic analysis," *Earthquake Engineering & Structural Dynamics*, vol. 26, no. 3, pp. 701–716, 2002.
[47] E. Bojórquez, A. Terán-Gilmore, S. E Ruiz, and A. Reyes-Salazar, "Evaluation of structural reliability of steel frames: interstory drift versus plastic hysteretic energy," *Earthquake Spectra*, vol. 27, no. 3, pp. 661–682, 2011.
[48] A. Rodríguez-Castellanos, S. E. Ruiz, E. Bojórquez, and A. Reyes-Salazar, "Influence of spectral acceleration correlation models on conditional mean spectra and probabilistic seismic hazard analysis," *Earthquake Engineering & Structural Dynamics*, vol. 50, pp. 1–20, 2020.
[49] A. Rodríguez-Castellanos, S. E. Ruiz, E. Bojórquez, M. A. Orellana, and A. Reyes-Salazar, "Reliability-based strength modification factor for seismic design spectra considering structural degradation," *Natural Hazards and Earth System Sciences*, vol. 21, pp. 1445–1460, 2021.
[50] R. K. McGuire, "Probabilistic seismic hazard analysis and design earthquakes: closing the loop," *Bulletin of the Seismological Society of America*, vol. 85, no. 5, pp. 1275–1284, 1995.
[51] S. L. Kramer, *Geotechnical Earthquake Engineering*, Prentice-Hall, Hoboken, NJ, USA, 1996.
[52] J. W. Baker, *Probabilistic Seismic Hazard Analysis*, Independently Published, Chicago, Illinois, 2013.

Hindawi
Advances in Civil Engineering
Volume 2021, Article ID 9868956, 1 page
https://doi.org/10.1155/2021/9868956

Corrigendum

Corrigendum to "Explosive Performance Assessment of Buried Steel Pipeline"

Seyed-Mohammad Seyed-Kolbadi,[1] Mohammad Safi,[2] Ayoub Keshmiri,[3] S. Mahdi S. Kolbadi,[4] and Masoud Mirtaheri[4]

[1]*Department of Civil Engineering, Technical and Vocational University (TVU), Tehran, Iran*
[2]*Shahid Beheshti University, Department of Civil and Environmental Engineering, Tehran, Iran*
[3]*Department of Civil Engineering, Branch of Aliabad, University of Golestan, Aliabad, Iran*
[4]*Department of Civil Engineering, KN Toosi University of Technology, Tehran, Iran*

Correspondence should be addressed to S. Mahdi S. Kolbadi; mahdi_kolbadi@sina.kntu.ac.ir

Received 18 October 2021; Accepted 18 October 2021; Published 31 October 2021

In the article titled "Explosive Performance Assessment of Buried Steel Pipeline" [1], the author Seyed-Mohammad Seyed-Kolbadi was affiliated to Department of Civil Engineering, Branch of Shahid Chamran, Technical and Vocational University of Golestan, Gorgan, Iran, which is incorrect.

The correct affiliation for this author is "Department of Civil Engineering, Technical and Vocational University (TVU), Tehran, Iran."

The corrected list of affiliations is shown in the author information above.

References

[1] S.-M. Seyed-Kolbadi, M. Safi, K. Ayoub, S. M. S. Kolbadi, and M. Mirtaheri, "Explosive performance assessment of buried steel pipeline," *Advances in Civil Engineering*, vol. 2021, Article ID 6638867, 24 pages, 2021.

Hindawi
Advances in Civil Engineering
Volume 2021, Article ID 6475942, 10 pages
https://doi.org/10.1155/2021/6475942

Research Article

Analysis Using High-Precision Airborne LiDAR Data to Survey Potential Collapse Geological Hazards

Jinxing She,[1,2] Awei Mabi,[3] Zhongming Liu,[3] Mingqiang Sheng,[3] Xiujun Dong,[1] Fei Liu,[2] and Shiyang Wang[4]

[1]*Chengdu University of Technology, Chengdu 610059, China*
[2]*Technology Service Center of Surveying and Mapping, Sichuan Bureau of Surveying, Mapping and Geoinformation, Chengdu 615000, China*
[3]*Nanchang Institute of Science and Technology, Nanchang 330000, China*
[4]*32023 Troops, Dalian 116023, China*

Correspondence should be addressed to Zhongming Liu; 781637124@qq.com

Received 22 April 2021; Revised 2 September 2021; Accepted 11 September 2021; Published 12 October 2021

Academic Editor: Edén Bojórquez

On August 8, 2017, an earthquake of magnitude 7.0 on the Richter scale occurred in Jiuzhaigou, Sichuan, causing significant damage to both life and property. Traditional geological hazard investigation is difficult in Jiuzhaigou because of the high altitude, the high-altitude canyons, and the vegetation-covered seismic areas. This study explores the technical advantages of using airborne LiDAR technology to penetrate vegetation and gather information directly from the surface, rapidly acquiring airborne 3D point cloud data in difficult areas. Through the preprocessing of data, the high-precision digital terrain and landform results were obtained. Comparative research found that the DEM obtained by high-precision airborne LiDAR technology has significant advantages in terms of the accuracy, details, and microgeomorphology of the data collected. The results can be directly used in the early identification of disasters, such as during the initial collapse or for disaster management. Studies have shown that airborne LiDAR has the technical advantage of penetrating vegetation to the surface and can, therefore, be used to guide the early identification and management of geological disasters in similar areas in the future.

1. Introduction

Rockfall hazards are phenomena that commonly occur in mountainous regions [1–3]. During a rockfall, a solid body composed of rock and soil moves under the action of gravity, rolling, bouncing, and falling down a slope. Lithological conditions, geological formations, topography, earthquakes, precipitation, and improper engineering are all important factors that trigger rockfall [4, 5]. In many countries, rockfall hazards generate significant annual losses to property and human life compared to other types of natural hazards; more attention has therefore been paid to this type of hazard [6–10], especially in areas that lie along mountain roads and some railways, where rockfall hazards are a district danger.

In recent years, extreme weather has become more frequent, engineering activities have continued to intensify, and the impact of strong earthquakes has continued to affect mountainous regions, causing abrupt and unexpected geological disasters in these regions [11]. Jiuzhaigou in Northwest Sichuan is characterized by mountains of high altitude and has endured a series of strong earthquakes, such as the Wenchuan and Lushan earthquakes which shattered a considerable number of high-altitude rocks and cracked much of the slopes on the mountainside. Fractures that subsequently developed in these rocks led to a substantial increase in the amount of material present that was likely to lead to hazards. The Mw 7.0 Jiuzhaigou Earthquake that occurred on 8 August 2017 led to approximately 300 rockfall events, causing 25 deaths in 8 counties, with 525 injured and 6 missing. A total of 176492 people (including tourists) were affected to varying degrees, 73671 residential properties were damaged, and the destruction covered a total area of 18295 km^2 [12, 13].

Faced with the severe challenge from natural disasters, humanity needs to reflect on the impact that the current lifestyle has on the environment [14, 15]. Significant amounts of effort have been focused over the last twenty years on predicting the mechanisms that trigger rockfall hazards, including the spatial and temporal distributions and the consequences [16–21].

As a result, several techniques that can be used for mapping rockfall susceptibility, hazard, and risk have been developed and applied in different geographic areas [22–24].

Airborne laser radar technology and the first 3D rolling stone/rockfall process model that has been integrated with the GIS environment were mainly used in this study for identification and evaluation, to improve rockfall hazard studies for Jiuzhaigou environmental management and to improve rockfall susceptibility mapping and analyses. Remote sensing geological disaster interpretation technology, airborne laser radar digital terrain analysis technology, GIS data processing technology, and image morphology analysis were combined with field investigation to evaluate the most serious threats from rockfall and to identify the source area of rockfalls. Combining the quantitative evaluation model of rockfall frequency, speed, and height with a quantitative analysis of the physical rocks that have fallen, the realization of the rolling stones/rockfall three-dimensional physical deterministic process model and probability statistics model are combined to improve predictions of the risk of disaster in the Jiuzhaigou National Park.

2. Study Area

Jiuzhaigou is located between the Qinghai-Tibet plateau and the Sichuan basin in a mountain transition zone (100°, 30–104° 27 ′ north and latitude 30°, 34–35° 19 ′) and is a world natural heritage site, national key scenic area, national 5 A-class tourist scenic area, and a national geological park. The mouth of the Jiuzhaigou River is only 2000 m above sea level, while the central peaks in this region are at heights above 4000 m and the southern margin is over 4500 m. Original forest covers 80% of the valley [25–28].

The 2017 earthquake not only caused casualties and property loss, but it also led to geological disasters and problems in the ecological balance that still affect some areas such as the famous Panda Sea, the Five Flower Lake, some waterfalls, and other parts of the landscape that suffered serious damage. The vertical topography of Jiuzhaigou changed significantly, and natural disasters and geological hazards such as landslides, rockfalls, and wide-scale flows of debris threatened the entire 651 km^2 of the National Park of Jiuzhaigou, with the formation of more than 30 gullies containing flows of debris.

Geological disasters have tended to be dominated by debris flow since 1980, with 10 major mudslides occurring from 1980 to 1985, and another large mudslide in 2003 [29, 30]. The earthquake on 12 May 2008 in Wenchuan had a significant impact, causing many secondary geological disasters, and serious safety hazards have remained in several areas. A comprehensive geological survey of Jiuzhaigou National Park was carried out in early 2010, and more than 50 locations were identified at which geological hazards are likely to happen [31, 32]. Earthquakes that reach 8.8 on the Richter scale are therefore likely to aggravate the risk of geological disaster in Jiuzhaigou, constituting a threat to the ecological environment, landscape, roads, residential areas, river systems, and the safety of tourists that severely restricts both the tourism and the development of the economy in Jiuzhaigou (Figure 1).

3. Materials and Methods

Figure 2 is a schematic diagram of the proposed methods. It consists of three major components: (i) the acquisition of LiDAR data and preprocessing, (ii) the identification of the rockfall source area via digital terrain analysis using techniques such as morphometry, topography, remote sensing geology, 3D GIS technology, and human-computer interactive interpretation, and (iii) the analysis and assessment of rockfall hazards.

3.1. Spatial Modeling and Advantages of LiDAR Technology. RockFall Analyst is the first 3D rolling stone rockfall process model that is fully integrated with the GIS environment, combining the rolling stone/rockfall 3D physical deterministic process model with a statistical probability model to improve the accuracy of disaster risk analysis. Two major steps are utilized by Rockfall Analyst. First, a 3D dynamic model uses physics to calculate and predict the 3D trajectory of rolling stones and falling rocks, accompanied by information concerning the velocity, the dynamic processes that occur during flight through the air, collision, rebound, rolling, and sliding. Secondly, the rolling stone and rockfall disaster space grid analysis model is initiated, converting the information about the falling rocks and the velocity that was obtained in vector format during the first step into a grid format that can be used to better relay spatial information concerning the elements of the disaster. Statistical software, the adjacent domain analysis technique, and methods that estimate the surface smoothness are then utilized to predict the spatial distribution of the various elements of rockfall, including the frequency, potential energy, and the three main elements of kinetic energy.

Airborne LiDAR includes a position measurement system, an attitude measurement system, a 3D laser scanner (point cloud access), equipment for gathering images such as 3D laser scanner active laser beam, by which precise information about the target such as distance, slope, roughness, and reflectance can be obtained from the returning laser pulse, and a digital camera, which is used to acquire the digital image of the target. Subsequent processing of the information gathered with airborne radar can generate 3D laser point clouds with true color (or ground reflection intensity). Compared to traditional photogrammetric techniques, airborne LiDAR not only provides high-resolution, high-precision two-dimensional images of the topography and landform but also uses multiple echo techniques that can penetrate ground vegetation, effectively removing the influence of surface vegetation via a filtering algorithm to obtain accurate data concerning ground elevation. As a result, LiDAR technology is usually used in situations where high mountains are covered by substantial

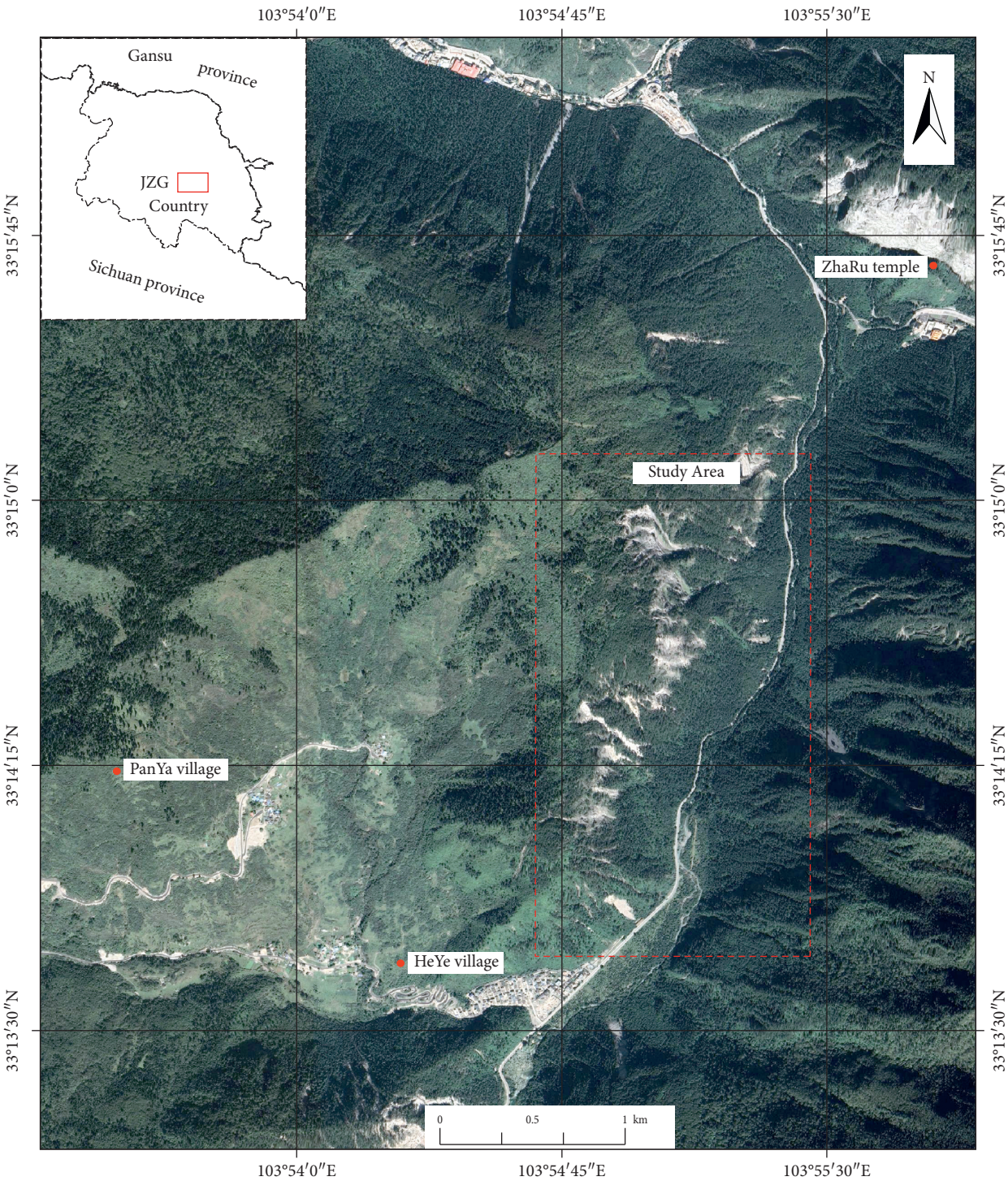

Figure 1: The map of study area. The red dotted box is the scope of the study area, where vegetation damage caused by the earthquake caused a collapse, threatening the road directly below.

amounts of vegetation, effectively eliminating the effects produced by the presence of vegetation and providing a true picture of the ground. LiDAR is therefore useful for identifying potential geological hazards in areas with substantial amounts of the mountain vegetation, especially for identifying ancient landslides (Figure 3), or areas where earthquakes have led to the shattering of rocks and caused minor rockfalls without accompanying landslides.

3.2. LiDAR Capturing and Processing. Measurement using remote sensing geological airborne LiDAR technology has been ongoing in Jiuzhaigou since September 2017. The first phase of the data was acquired during September 2017 with Mi-171 helicopters carrying the Leica ALS80 airborne LiDAR system flying at an altitude of 1400 m at 150 km/h, using a laser pulse frequency of 100 kHz, a point cloud density of 20 points/square meters, and an image resolution

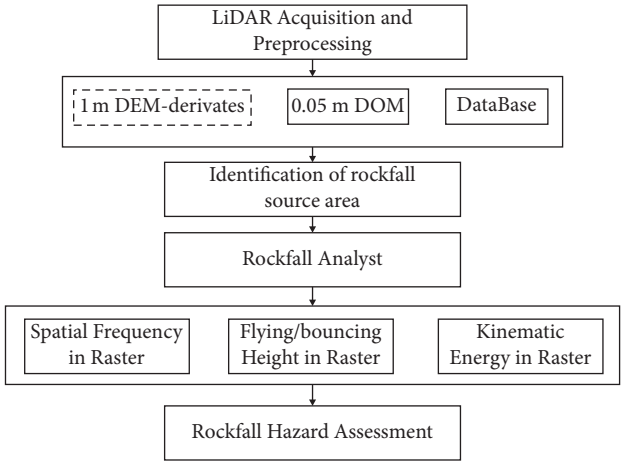

Figure 2: Rockfall hazard assessment workflow using airborne LiDAR and Rockfall Analyst.

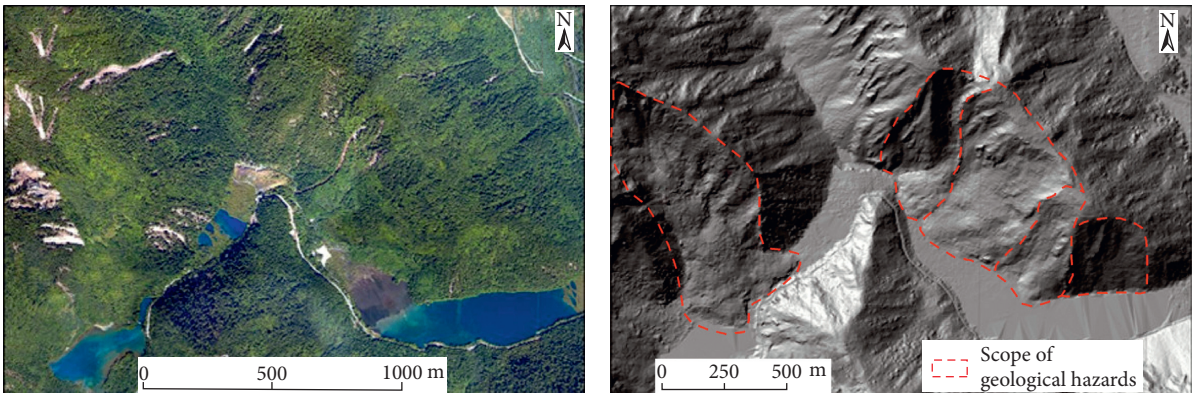

(a) (b)

Figure 3: Comparison of an optical image and airborne LiDAR data. (a) Orthophoto map for disaster interpretation. (b) Shadow map of the same mountains in which vegetation has been filtered out based on laser point cloud data.

of 0.05 m. Through LiDAR strip adjustment, point cloud denoising, filtering, classifying, and the construction of a triangulated irregular network (TIN), a digital elevation model (DEM) with a horizontal resolution of 1 m and a vertical accuracy of ±20 cm was generated from the high-resolution-based ground LiDAR point data. A coarser DEM with a resolution of 30 m (30 m DEM) was provided for comparison by the Geospatial Data Cloud site, Computer Network Information Center, Chinese Academy of Sciences (http://www-.gscloud.cn). Comparison found that the high-resolution DEM was capable of providing more detailed geological hazard prediction from information concerning the characteristics of precursors such as physiognomy, gullies, steep cliff scarps, the presence of clastic rocks, and other associated information (Figure 4).

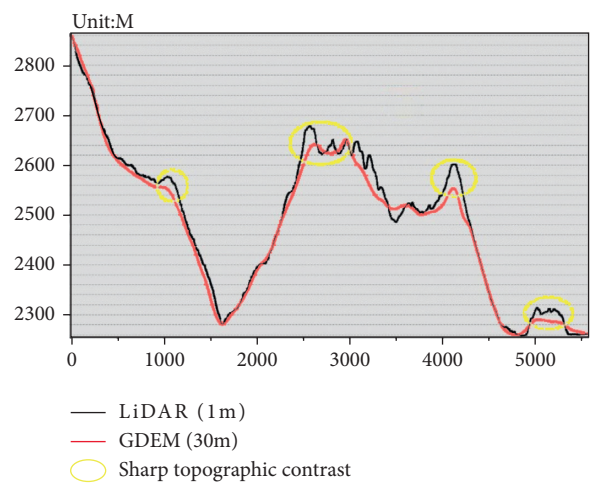

Figure 4: Comparison of the 1 m resolution DEM from LiDAR and the 30 m AsterGDEM DEM terrain profile data.

3.3. Fine Processing Based on the Geological Hazard Remote Sensing Survey. The accuracy of recognizing and evaluating rockfall hazards is directly proportional to the mathematical accuracy, point cloud density, and quality of the LiDAR data. In the process of denoising and filtering point clouds, classification, modeling, and the production of a DEM, only one original laser point per m^2 is provided with traditional mapping in accordance with conventional criteria such as a 1 : 2000 scale, and only four original laser points are produced on a scale of 1 : 1000. Although this can meet the requirements for surveying and producing topographic

maps, it is far from adequate for the interpretation of refined geological hazards. The original point cloud was filtered to remove the true surface point clouds retained by vegetation, which could not meet the requirements for the extraction of information pertaining to disaster precursors. On the other hand, if the laser point cloud density is higher, the penetration rate is stronger, and more ground points are obtained through automatic filtering and manual intervention, meaning that topographies can be attained in finer detail, which is more conducive to the extraction of information concerning disaster precursors and the demarcation of the source area of materials for potential rockfall disasters. The classification algorithm based on laser echo frequency, point cloud elevation, and the use of the nadir to extract ground points were, therefore, used in this study. By fully integrating the advantages of the above algorithms, more detailed textures can be obtained for the interpretation of geological hazards. Figures 5(a) and 5(b) show a comparison of the same image before and after improvement.

3.4. Identification of Rockfall Based on Digital Terrain Analysis Techniques. The identification of the source area for material that is involved in rockfall disasters is divided into two steps. The first step was to use information concerning 100 known rockfall points that were obtained by the geological survey department from 1998 to 2017 as the dependent variable. The location of the above historical disaster points was identified via superposition of spatial positions, and the potential for further rockfalls was analyzed using high-precision data from airborne LiDAR, identifying new source areas. It was found by statistical analysis that rockfalls that occur in Jiuzhaigou have the following characteristics. Rockfall hazards occur most often in approximately 3000 areas that are close to roads, indicating a close relationship between rockfall and construction. Secondly, there is a rapid upward trend in the probability of rockfall on slopes that are greater than 45°. Figure 6(a) presents a 3D interpretation scene of collapse geological hazard potential constructed using 0.5 m optical remote sensing image data and 1m DEM data. Figure 6(b) describes the use of image recognition algorithm to extract the collapse hazard potential range based on 0.5 m disaster remote sensing image data, based on which postearthquake disaster rapid statistics can be carried out. Figure 6(c) focuses on the collapse geohazard potential hazard detection using the mountain shading technique of digital terrain analysis. As (1) shows [33], disaster potential hazard detection analysis from different viewpoints is realized by changing the solar altitude angle and azimuth angle. Figure 6(d) illustrates the application of slope analysis based on digital terrain technology, which can circle the high side slopes greater than 50 degrees based on slope analysis. Figure 6(e) indicates the terrain compactness analysis, which is also one of the digital terrain analysis techniques, and can provide a reference basis for the identification of the development range of the collapse hazard potential. Figure 6(f) demonstrates the topographic relief analysis, which can analyze the structure of large rock masses and is valuable for defining the scope of landslide hazards.

$$\begin{aligned}\text{Hillshade} = 255.0 * [&\text{Cos}(\text{Zenith\_rad}) * \text{Cos}(\text{Slope\_rad}) \\ &* \text{Sin}(\text{Zenith\_rad}) \\ &* \text{Sin}(\text{Slope\_rad}) \\ &* \text{Cos}(\text{Azimuth\_rad} - \text{Aspect\_rad})].\end{aligned} \tag{1}$$

3.5. Modeling Procedure. The simulation and prediction of rockfall hazard can be carried out when the high-risk areas of rockfall hazard are analyzed comprehensively using digital terrain analysis and three-dimensional visualization technology combined with historical data concerning geological disasters. To further examine the effect of topography on rockfall behavior, simulations using DEMs with resolutions of 1 m, 12.5 m, and 30 m were carried out (Figure 7. These simulations included the initial detachment and fall of the rocks and the subsequent bouncing, rolling, sliding, and deposition. Raster images of rockfall spatial frequency, the height of airborne rocks (potential energy), and kinetic energy were provided based on the trajectories and velocities produced by the 3D rockfall simulations. The resolution of each raster image is the same as that of the input DEM. The simulation of the rockfall processes described above using the DEM from the LiDAR survey was repeated using the 30 m DEM. Using the raster modeling function in Rockfall Analyst, rockfall trajectories were calculated for each grid cell, each of which covered an area of $1\,\text{m}^2$. Spatial geostatistical techniques were employed to analyze the trajectories and determine the rockfall spatial frequency for the whole study area. Comparison of the 1 m, 12.5 m, and 30 m DEM data indicated that the simulation of the falling path gradually became more linear and the curvature gradually decreased at lower resolutions, whereas the falling rocks were affected by all variations in topography at a resolution of 1 m, reflecting the linearity of the simulation under the influence of the gravity drop shape process, and verifying the advantages of using high-resolution airborne LiDAR data.

Finally, the potential impact of rockfalls on the Jiuzhaigou area was evaluated using the final rockfall hazard map which takes all available raster layers into account.

4. Results and Discussion

4.1. DEMs with Different Resolutions Are Completely Different for Predicting Disasters. Historical rockfall data were combined with digital topography, high-resolution orthophoto images, and 3D visualization to obtain the source of the rockfall in the study area. As shown in Figure 7, DEM data with different resolutions corresponding to identified potential rockfall points were used to simulate the rockfall and the path taken by these rocks. It was found that the rolling stone path simulated by DEM at an accuracy of 30 m is almost straight down the slope of the mountain, and the falling speed is particularly fast, reaching 95 m/s. The influence of topography can be ignored. When DEM precision is increased to 12.5 m, the simulation is better, the rolling

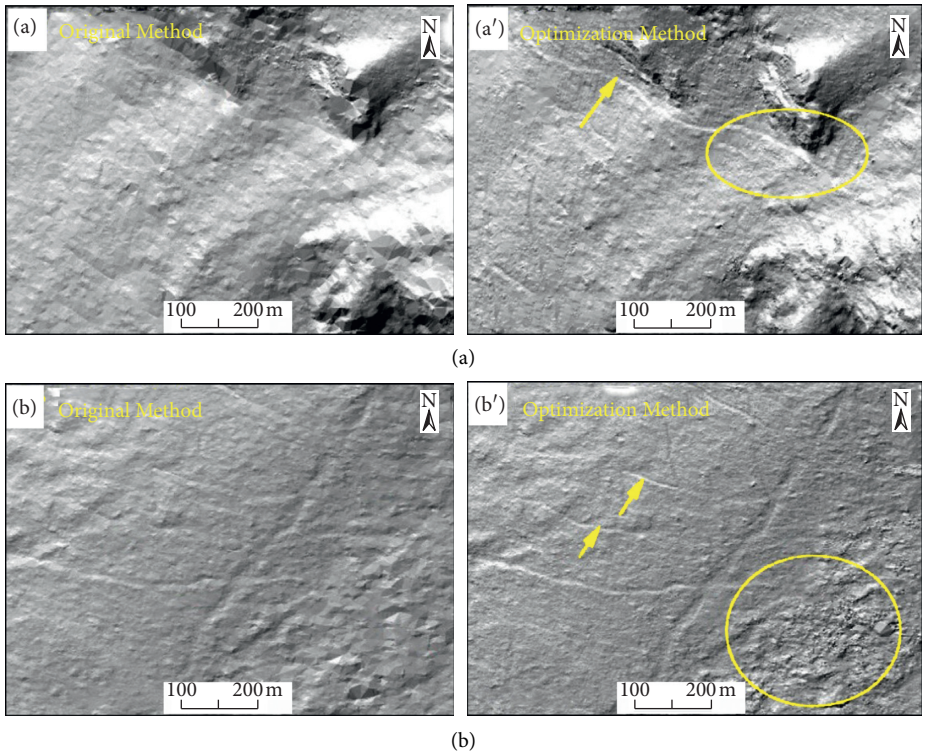

Figure 5: Comparison of the traditional filtering method and the geological filtering method for displaying microgeomorphology: (a, b) the results gained with the traditional filtering algorithm and (a′, b′) the results of using the optimization filtering algorithm, which produces smaller landforms (steep hills, clastic rocks).

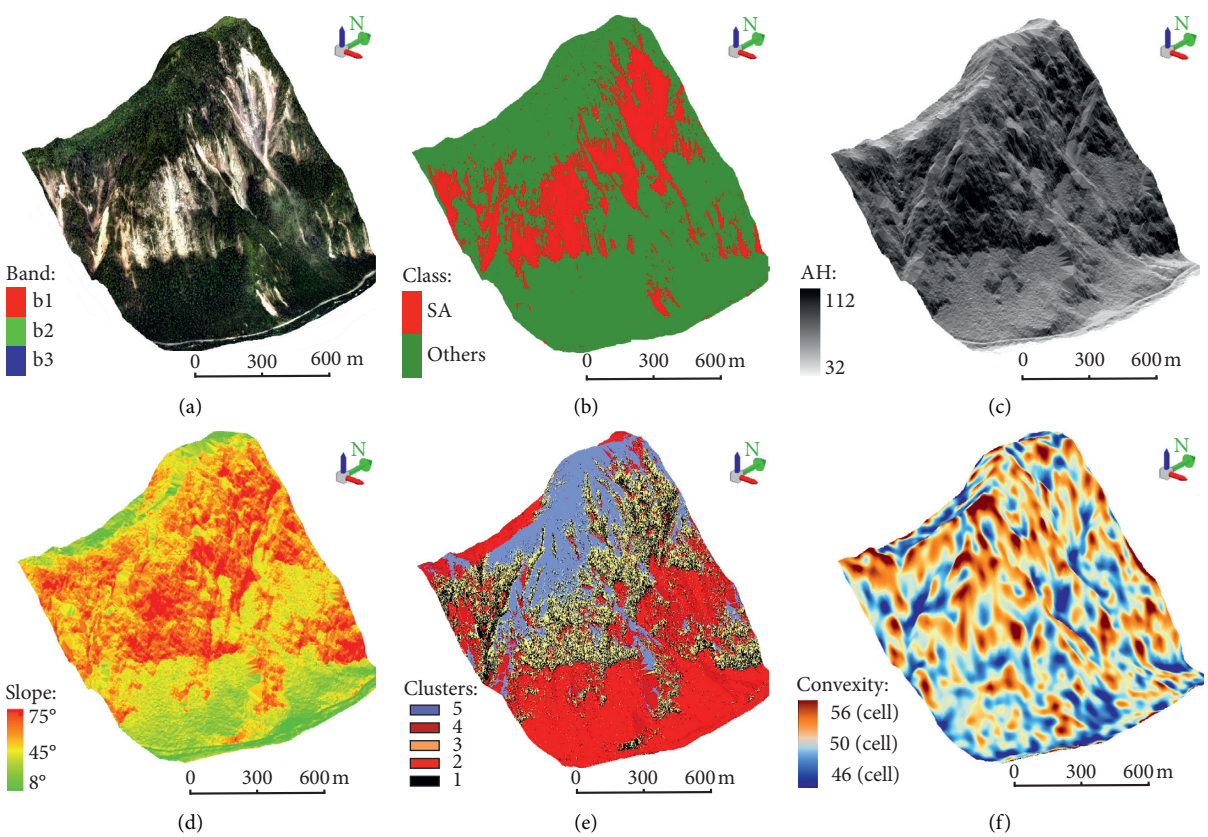

Figure 6: Identification of the source of the material causing rockfall hazards based on digital terrain analysis technology: (a) 3D visualization technology, (b) neural network classification was used to identify the source area of debris, (c) hill-shading map, (d) slope, (e) terrain clustering, and (f) terrain surface convexity.

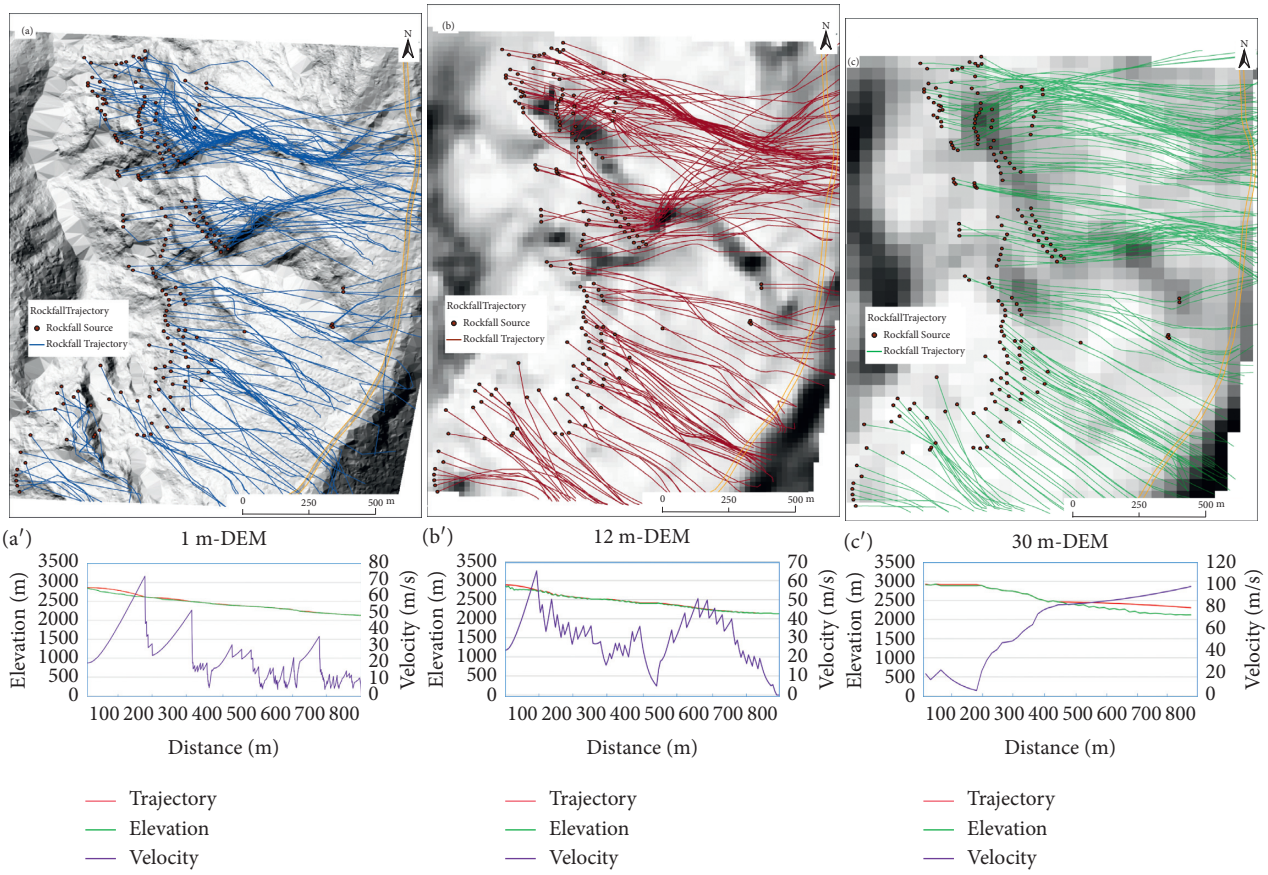

Figure 7: (a) DEM with a 1 m resolution was used to simulate the path of falling rocks, (b) using DEM with 12.5 m resolution, and (c) using DEM with 30 m resolution. (a′) The falling speed and distance of falling rocks at a 1 m resolution, (b′) the falling speed and distance of falling rocks with a 12.5 m resolution, and (c′) the falling speed and distance of falling rocks at a resolution of 30 m.

speed is significantly less than that observed in the 30 m DEM simulation, and the falling rocks are airborne for significantly longer periods than seen using 30 m DEM.

This result shows that the accuracy of the terrain used for predicting the effects of simulated rockfall disasters is of significant importance. When DEM accuracy is increased to 1 m, it can be seen from Figure 7(a) that the track of the falling rocks is significantly affected by changes in the topography. It can be seen from the figure that the falling rocks follow an obvious "S" shaped path, and the speed of the fall is also significantly reduced. It is also evident when observing Figure 7(a)′ that the rocks are airborne for even longer periods, which is due to the influence of micro-geomorphology. When the range of a dangerous rockfall is identified, it is, therefore, apparent that the path, speed, and height of the rockfall can be accurately simulated based on topographic and geomorphic data, which plays a very important role in the comprehensive assessment of geological safety along mountain roads.

4.2. High-Precision Airborne LiDAR Data Is More Practical. We used 5 ∗ 5 grids to calculate the slope and slope direction based on digital terrain analysis. Digital elevation models with resolutions of 30 m, 12.5 m, and 1 m were used to carry out the risk assessment of the rockfall disaster.

Frequency, height, and energy raster layers were used to set the hazard class numbers. The comprehensive weight factor method was used to evaluate the risk level of the rockfall disaster. The spatial frequency distribution of the falling stones was obtained from the dynamic simulation of the paths of falling rocks, which was the most critical factor in rockfall evaluation. The weight was set at 0.5.

At the same time, physical parameters such as rock mass can be estimated based on the scope of the material source area, and the gravitational potential energy contained in the material source area can be obtained indirectly. Greater amounts of potential energy are contained in larger rocks, with greater threats to nearby slopes, roads, and other forms of infrastructure. Therefore, the weight factor of rock energy was set at 0.3. Finally, the height of the rockfall source area is also an important factor. The higher the location of the rockfall source area, the greater the force generated by impact, and the more serious the threat to the slope and road, so the weight was set at 0.2. Using the above steps, different rockfall disasters were obtained and shown according to these categories. Images demonstrating the final evaluation are shown in Figure 8.

4.3. Disaster Simulation and Actual Analysis. As shown in Figure 8, the collapse disaster image is a 0.5-meter image taken after the earthquake disaster, which can clearly

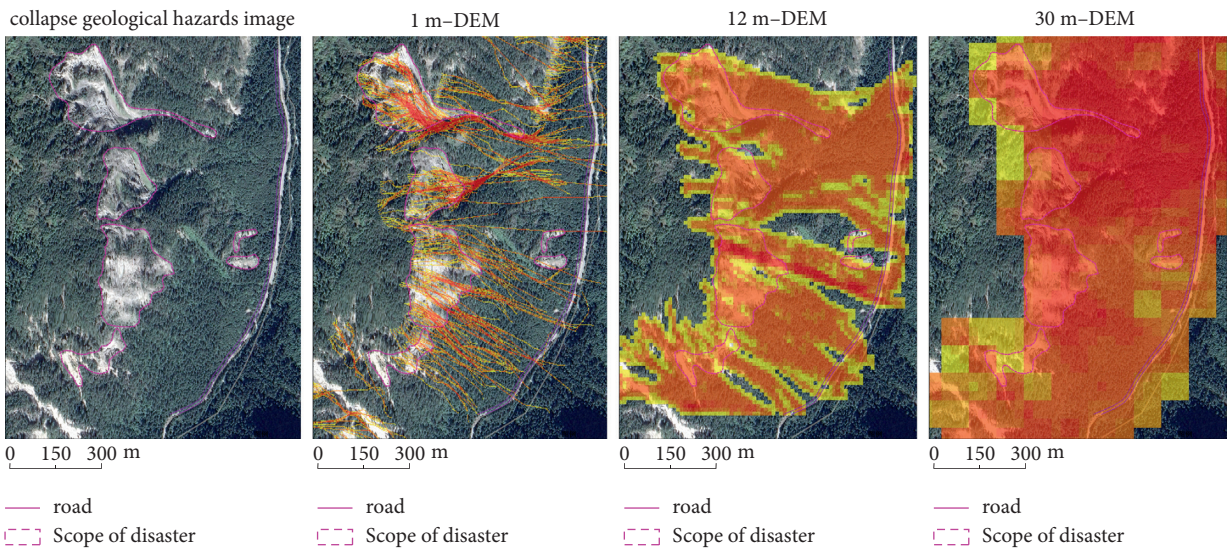

Figure 8: DEMs with different resolutions have different results in disaster evaluation along highways.

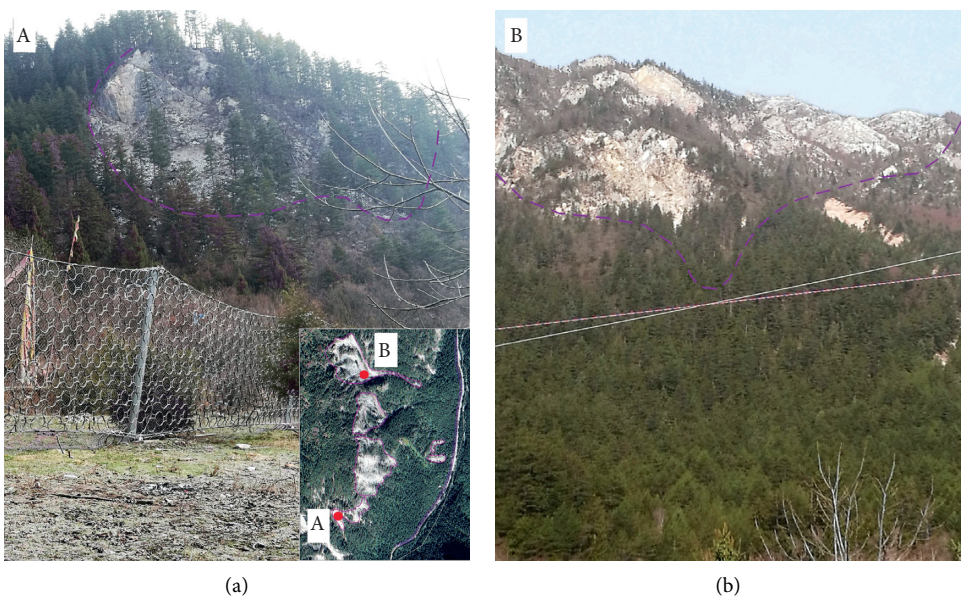

Figure 9: Field validation at points A and B shows that 1m DEM data constructed by high-precision airborne LiDAR is more valuable for collapse risk analysis than DEM data of 12 m and 30 m.

identify the threat range caused by the collapse disaster. We overlay the threat range and the DEM assessment results of 1 m, 12 m, and 30 m resolution. Study found that 1 m resolution DEM evaluation of disaster threat range profile is more close to the actual situation, the simulation of the rolling stone path and vegetation breakage also conforms to the disaster situation, the scope and the threat of collapse disasters threat range Rolling Stones fit degree can reach more than 90%, and the effect of 12-meter DEM analysis is clearly "enlarge effect." However, the simulation effect of 30 m DEM basically "has no reference value." Therefore, high-precision DEM has high value in actual disaster analysis.

4.4. Field Validation. Through laboratory experiments, we have preliminarily concluded that high-precision remote sensing image has decisive value for the risk assessment of collapse disaster. In order to further verify the experimental conclusions, we adopted field investigations to verify them. Figure 9(a) shows Heye Village in Jiuzhaigou scenic spot. We matched the hazard assessment vector range of 1 m, 12 m, and 30 m rolling stones with the longitude and latitude coordinates of the field. Through field inspection, most of the collapse disasters occurred within the range of 1 m DEM hazard assessment, as shown in the figure, and disaster prevention measures have been taken in area A. Similarly, at point B, the resolution assessment range of 1 m DEM is the

closest to the actual situation, and the verification shows that it is the collapse disaster zone now. However, the predicted disaster range of 12 meters and 30 meters is obviously larger than the actual disaster range. It is found that the predicted area of 12 meters and 30 meters is covered by high vegetation currently, and no collapse disaster has occurred. Therefore, the above verification further proves that the collapse disaster prediction method constructed by high-precision airborne LiDAR is reliable and practical.

5. Conclusions

Rockfall is a natural phenomenon, but when it poses a threat to human life, the environment, roads, railways, or important support slopes, it becomes a hidden danger that must be considered. Scientific and reasonable assessment methods are, therefore, needed for comprehensive risk analysis. Traditional scientific evaluation methods are mostly based on optical remote sensing images and field investigation. Airborne laser radar technology has significant advantages over ground-based three-dimensional laser scanning technology or other forms of remote sensing technology as the laser pulse can obtain highly accurate data concerning topography through any vegetation that is present and can, therefore, be used to construct high fidelity topography data based on the digital terrain analysis technology from which the slope, slope direction, degree of concave and convex terrain, terrain roughness, and the openness of the terrain can be obtained. Factors such as optical remote sensing image data can, therefore, be used to accurately identify the potential sources of rockfalls when combined with field investigation to obtain the physical parameters of the rock in the study area. Finally, it can be used to accurately mitigate areas that are potentially prone to rockfall disaster and guide construction, to provide slope support, develop protective networks, construct retaining walls, and establish other systems for the prevention and control of geological disaster.

The early recognition and prediction of geological disaster is challenging, and although high-precision airborne LiDAR data can be used for the identification of possible sources of material for rockfall, risk assessment, and potential hazards, the cost of acquiring airborne LiDAR data can become extreme, so geological hazard investigations are often combined with oblique photography modeling to obtain high-precision digital surface modes for a study area, in which the model includes features concerning the terrain and the texture for clearer analysis of the potential threat from rock fracture and other important processes [34].

Data Availability

The high-precision airborne LiDAR data and DEM data used to support the findings of this study are included within the article.

Conflicts of Interest

The authors declare that they have no conflicts of interest.

Acknowledgments

The authors gratefully acknowledge the financial support of The National Key Research and Development Program of China (2018YFC1505202) and the National Natural Science Foundation of China (42072306).

References

[1] R. A. Kromer, D. J. Hutchinson, M. J. Lato, D. Gauthier, and T. Edwards, "Identifying rock slope failure precursors using LiDAR for transportation corridor hazard management," *Engineering Geology*, vol. 195, pp. 93–103, 2015.

[2] R. Mahalingam and M. J. Olsen, "Evaluation of the influence of source and spatial resolution of DEMs on derivative products used in landslide mapping," *Geomatics, Natural Hazards and Risk*, vol. 7, no. 6, pp. 1835–1855, 2015.

[3] E. Arnone, A. Francipane, A. Scarbaci, C. Puglisi, and L. V. Noto, "Effect of raster resolution and polygon-conversion algorithm on landslide susceptibility mapping," *Environmental Modelling & Software*, vol. 84, pp. 467–481, 2016.

[4] W. Chen, X. Li, Y. Wang, G. Chen, and S. Liu, "Forested landslide detection using LiDAR data and the random forest algorithm: a case study of the Three Gorges, China," *Remote Sensing of Environment*, vol. 152, pp. 291–301, 2014.

[5] H. Kim, S. W. Lee, C.-Y. Yune, and G. Kim, "Volume estimation of small scale debris flows based on observations of topographic changes using airborne LiDAR DEMs," *Journal of Mountain Science*, vol. 11, no. 3, pp. 578–591, 2014.

[6] H. Lan, C. Derek Martin, and C. H. Lim, "RockFall analyst: a GIS extension for three-dimensional and spatially distributed rockfall hazard modeling," *Computers & Geosciences*, vol. 33, no. 2, pp. 262–279, 2007.

[7] R. Copons and J. M. Vilaplana, "Rockfall susceptibility zoning at a large scale: from geomorphological inventory to preliminary land use planning," *Engineering Geology*, vol. 102, no. 3-4, pp. 142–151, 2008.

[8] P. M. Santi, C. P. Russell, J. D. Higgins, and J. I. Spriet, "Modification and statistical analysis of the Colorado rockfall hazard rating system," *Engineering Geology*, vol. 104, no. 1-2, pp. 55–65, 2009.

[9] V. Chiessi, M. D'Orefice, G. S. Mugnozza, V. Vitale, and C. Cannese, "Geological, geomechanical and geostatistical assessment of rockfall hazard in San Quirico Village (Abruzzo, Italy)," *Geomorphology*, vol. 119, no. 3-4, pp. 147–161, 2010.

[10] H. Lan, C. D. Martin, C. Zhou, and C. H. Lim, "Rockfall hazard analysis using LiDAR and spatial modeling," *Geomorphology*, vol. 118, no. 1-2, pp. 213–223, 2010.

[11] B. T. Pham, I. Prakash, and D. Tien Bui, "Spatial prediction of landslides using a hybrid machine learning approach based on Random Subspace and Classification and Regression Trees," *Geomorphology*, vol. 303, pp. 256–270, 2018.

[12] A. Erener, A. A. Sivas, A. S. Selcuk-Kestel, and H. S. Düzgün, "Analysis of training sample selection strategies for regression-based quantitative landslide susceptibility mapping methods," *Computers & Geosciences*, vol. 104, pp. 62–74, 2017.

[13] G.-F. Lin, M.-J. Chang, Y.-C. Huang, and J.-Y. Ho, "Assessment of susceptibility to rainfall-induced landslides using improved self-organizing linear output map, support vector machine, and logistic regression," *Engineering Geology*, vol. 224, pp. 62–74, 2017.

[14] T. Bibi, K. Azahari Razak, A. Abdul Rahman, and A. Latif, "Spatio temporal detection and virtual mapping of landslide

using high-resolution airborne laser altimetry (lidar) in densely vegetated areas of tropics," *ISPRS - The International Archives of the Photogrammetry, Remote Sensing and Spatial Information Sciences*, vol. XLII-4/W5, pp. 21–30, 2017.

[15] B. Kalantar, B. Pradhan, S. A. Naghibi, A. Motevalli, and S. Mansor, "Assessment of the effects of training data selection on the landslide susceptibility mapping: a comparison between support vector machine (SVM), logistic regression (LR) and artificial neural networks (ANN)," *Geomatics, Natural Hazards and Risk*, vol. 9, no. 1, pp. 49–69, 2017.

[16] G. C. Ohlmacher and J. C. Davis, "Using multiple logistic regression and GIS technology to predict landslide hazard in northeast Kansas, USA," *Engineering Geology*, vol. 69, no. 3-4, pp. 331–343, 2003.

[17] K.-T. Chang, S.-H. Chiang, and M.-L. Hsu, "Modeling typhoon- and earthquake-induced landslides in a mountainous watershed using logistic regression," *Geomorphology*, vol. 89, no. 3-4, pp. 335–347, 2007.

[18] A. Yalcin, S. Reis, A. C. Aydinoglu, and T. Yomralioglu, "A GIS-based comparative study of frequency ratio, analytical hierarchy process, bivariate statistics and logistics regression methods for landslide susceptibility mapping in Trabzon, NE Turkey," *Catena*, vol. 85, no. 3, pp. 274–287, 2011.

[19] I. Colkesen, E. K. Sahin, and T. Kavzoglu, "Susceptibility mapping of shallow landslides using kernel-based Gaussian process, support vector machines and logistic regression," *Journal of African Earth Sciences*, vol. 118, pp. 53–64, 2016.

[20] L. C. Razanamahandry, H. A. Andrianisa, H. Karoui, J. Podgorski, and H. Yacouba, "Prediction model for cyanide soil pollution in artisanal gold mining area by using logistic regression," *Catena*, vol. 162, pp. 40–50, 2018.

[21] Y. Xiong and R. Zuo, "GIS-based rare events logistic regression for mineral prospectivity mapping," *Computers & Geosciences*, vol. 111, pp. 18–25, 2018.

[22] F. Guzzetti, A. Carrara, M. Cardinali, and P. Reichenbach, "Landslide hazard evaluation: a review of current techniques and their application in a multi-scale study, Central Italy," *Geomorphology*, vol. 31, no. 1, pp. 181–216, 1999.

[23] L. Otávio Aleotti Maia and R. Yahya Qassim, "Minimum cost safety stocks for frequent delivery manufacturing," *International Journal of Production Economics*, vol. 62, no. 3, pp. 233–236, 1999.

[24] K. Martinović et al., "Development of a landslide susceptibility assessment for a rail network," *Engineering Geology*, vol. 215, pp. 1–9, 2016.

[25] J. L. Florsheim, S. L. Ustin, Y. Tang et al., "Basin-scale and travertine dam-scale controls on fluvial travertine, Jiuzhaigou, southwestern China," *Geomorphology*, vol. 180-181, pp. 267–280, 2013.

[26] S. Li, X. Hu, Y. Tang, C. Huang, and W. Xiao, "Changes in lacustrine environment due to anthropogenic activities over 240 years in Jiuzhaigou National Nature Reserve, southwest China," *Quaternary International*, vol. 349, pp. 367–375, 2014.

[27] Y. Kong, Z. Kong, Z. Liu, C. Wei, and G. An, "Substituting small hydropower for fuel: the practice of China and the sustainable development," *Renewable and Sustainable Energy Reviews*, vol. 65, pp. 978–991, 2016.

[28] X. Qiao, J. Du, S. Lugli et al., "Are climate warming and enhanced atmospheric deposition of sulfur and nitrogen threatening tufa landscapes in Jiuzhaigou National Nature Reserve, Sichuan, China?," *The Science of the Total Environment*, vol. 562, pp. 724–731, 2016.

[29] X. Qiao, J. Du, S. H. Kota, Q. Ying, W. Xiao, and Y. Tang, "Wet deposition of sulfur and nitrogen in Jiuzhaigou national nature reserve, sichuan, China during 2015–2016: challenges," *Engineering Geology*, vol. 241, pp. 25–32, 2018.

[30] D. Zhao, C. Qu, X. Shan, W. Gong, Y. Zhang, and G. Zhang, "InSAR and GPS derived coseismic deformation and fault model of the 2017 Ms7.0 Jiuzhaigou earthquake in the Northeast Bayanhar block," *Tectonophysics*, vol. 726, pp. 86–99, 2018.

[31] Y. Chen, J. Hu, and F. Peng, "Seismological challenges in earthquake hazard reductions: reflections on the 2008 Wenchuan earthquake," *Science Bulletin*, vol. 63, no. 17, pp. 1159–1166, 2018.

[32] F. Huang, Z. Cao, S.-H. Jiang, C. Zhou, J. Huang, and Z. Guo, "Landslide susceptibility prediction based on a semi-supervised multiple-layer perceptron model," *Landslides*, vol. 17, no. 12, pp. 2919–2930, 2020.

[33] P. A. Burrough and R. A. McDonell, "Principles of Geographical Information Systems (Oxford University Press, New York), 190 ppPossible effects from regional emission reduction and local tourist activities," *Environmental Pollution*, vol. 233, pp. 267–277, 1998.

[34] L. Zhu, G. Wang, F. Huang, Y. Li, W. Chen, and H. Hong, "Landslide susceptibility prediction using sparse feature extraction and machine learning models based on GIS and remote sensing," *IEEE Geoscience and Remote Sensing Letters*, 2021.

Hindawi
Advances in Civil Engineering
Volume 2021, Article ID 9915947, 14 pages
https://doi.org/10.1155/2021/9915947

Research Article

Construction Stage Seismic Vulnerability Evaluation of a Continuous Girder Bridge with the Cast-in-Place Cantilever Construction Method

Hongxu Li,[1,2] **Yong Huang**,[1,2] **and Endong Guo**[1,2]

[1]*Institute of Engineering Mechanics, China Earthquake Administration, Harbin 150080, China*
[2]*Key Laboratory of Earthquake Engineering and Engineering Vibration of China Earthquake Administration, Harbin 150080, China*

Correspondence should be addressed to Yong Huang; huangyong@iem.ac.cn

Received 1 April 2021; Revised 13 August 2021; Accepted 25 August 2021; Published 3 September 2021

Academic Editor: Sonia E. Ruiz

To evaluate the vulnerability of bridges at various construction stages under the action of strong earthquakes, the incremental dynamic analysis (IDA) method is applied, and the vulnerabilities of a continuous girder case study bridge with the cast-in-place cantilever construction method, which owns five main construction stages, are evaluated and compared. The results show the following: With the increase in the peak ground acceleration (PGA), the vulnerabilities of bridges at different construction stages all increase. The fragility and vulnerability are mainly determined by the structural mechanical system condition and the mode shapes but not the modal frequency. For the working condition of seismic PGA of 0.4 g, (1) the bridge at the substructure construction stage may only experience slight or moderate damage with the exceedance probability of 8% to 5% and the mean loss ratio being only about 5%; (2) the vulnerabilities of bridges at the middle cantilever construction stage and the long cantilever construction stage are similar, the collapse damage exceedance probability is about 80%, and the mean loss ratio is about 65%; and (3) the vulnerabilities of bridges at the middle span closure construction stage and the bridge completion construction stage are nearly the same, the collapse damage exceedance probability is about 98%, and the mean loss ratio can reach 80%. The research results explore a new method for evaluating the vulnerability of bridges at different construction stages, which can provide suggestions for seismic damage defense and seismic insurance risk evaluation.

1. Introduction

In the statistics [1] of 279 bridge collapse cases after the year of 2000, the bridges with construction collapse cases comprised 46.59%, whereas natural disasters accounted for 28.32%. It is obvious that construction and natural disasters are important risk factors leading to bridge collapse accidents. Therefore, if a bridge under construction experiences an earthquake, the safety of the bridge will be seriously threatened. It is of great theoretical and practical significance to evaluate the antiseismic capacity of buildings [2]. Great attention should be paid to the seismic vulnerability evaluation, especially for bridges under construction.

For the study of the seismic vulnerability of bridges, most of the research studies have been conducted on completed bridges [3, 4]. To study the seismic fragility of long-span suspension bridges, Lu et al. [5] applied the probabilistic seismic demand models (PSDMs) method and improved a design based on fragility. Wu et al. [6] applied the incremental dynamic analysis (IDA) method and obtained the seismic capacity residual ratio of a structure. Zhang and Huo [7] used the frequency analysis method of exceeding the limit state along with the IDA method to analyze the seismic isolated bridge. Pan et al. [8] proposed a curve fitting method based on the damage index demand to capability ratio model to analyze the seismic vulnerability of New York continuous steel bridges. Cao et al. [9] studied the seismic fragility of multispan continuous girder bridges with consideration of the bond-slip behavior using the IDA method. Relatively little research has been done on the seismic vulnerability of

bridges during construction. In 2016, Yang et al. [10] analyzed the vulnerability of the whole process of the cantilever method for the concrete-filled steel tube superposed pier of a high-pier bridge in a mountainous area to analyze the risk of aftershock damage during the reconstruction of the bridge in an earthquake zone. Ohashi and Kiyomiya [11] performed a seismic safety analysis of a cable-stayed bridge with the suspension method, which included five construction stages. Hsu et al. [12] proposed a construction classification and vulnerability evaluation framework for different construction stages for Taiwan's buildings in 2013.

From the point of view of earthquake insurance, the existing commercial catastrophe risk models assume that a completed bridge has invariable vulnerability. However, this is not suitable for construction process risk because the vulnerabilities of bridges at every construction stage are different and these vulnerabilities may be more or less than those of a completed bridge. To evaluate the seismic risk of bridges under construction, it is important to research the differences of the seismic vulnerabilities of bridges at different construction stages.

In this research, a prestressed concrete continuous girder bridge with the cantilever method will be taken as the example to research the construction stage seismic vulnerability evaluation method. With consideration of the mechanical characteristics at different construction stages, five construction stages, which include the substructure, middle cantilever, long cantilever, middle span closure, and bridge completion stages, are comparatively researched on their seismic vulnerabilities. The seismic vulnerabilities of the bridges at different construction stages are evaluated by utilizing the IDA method.

2. Seismic Vulnerability Evaluation Method for Construction Stages

In this study, the fragility means the probability of structural response to exceed critical states under some seismic intensity measure. The vulnerability means the structural mean loss ratio under some seismic intensity measure. The fragility measures probability and vulnerability measure loss [13]. Therefore, the vulnerability evaluation is the computation process of the structural mean loss ratio.

In this study, the vulnerability evaluation method is as follows:

(1) Based on the practical construction method of the researched bridge, the whole construction process should be divided into different construction stages by considering different mechanical characteristics.

(2) The finite element modeling (FEM) of the bridge model should be developed by considering different construction stages. The incremental dynamic analysis method is applied to calculate the seismic demand values at different construction stages and for a range of earthquake intensities.

(3) For the bridge vulnerability evaluation under the action of strong earthquakes, the pier bottom sections are always regarded as fragile units. The moment-curvature values of the pier bottom sections are always regarded as the antiseismic capacity. The antiseismic capacity values can be obtained according to section characteristics, such as section size, material performance, and rebar layout.

(4) The ratios of the seismic demand value to the antiseismic capacity value at different construction stages and for different earthquake intensities can be calculated. In the log-log coordinate system, the function is fitted with the logarithm of the seismic intensity measure as the independent variable and the logarithm of the seismic demand value for the antiseismic capacity value ratio as the dependent variable.

(5) The longitudinal and transversal fragilities should be separately calculated. The seismic fragility curves of the bridge with comprehensive consideration of the longitudinal and transversal fragilities can be achieved.

(6) The loss ratios at different damage states are found based on reference [14]. The mean loss ratios at different construction stages are calculated for different peak ground accelerations (PGAs). The seismic mean loss ratios of the bridges at different construction stages can then be determined.

The flow chart of the vulnerability evaluation method is shown in Figure 1. In Figure 1, the information in the double boxes is the basic data that should be collected before the vulnerability evaluation, while the information in the single boxes is the intermediate variable in the evaluation process.

Figure 1 shows that the antiseismic capacity, seismic demand, fragility, and mean loss ratio are the core elements in the seismic vulnerability evaluation process, and they are the key factors for determining the structural seismic vulnerability.

3. Case Study Bridge Finite Element Modeling

3.1. Case Study Bridge Introduction. In this study, a prestressed concrete continuous girder bridge with the cast-in-place cantilever construction method is selected as a case study bridge to research the bridge vulnerability characteristics in the construction process.

The case study bridge has three spans. The first, second, and third spans are 51 m, 85 m, and 51 m, respectively. The girder cross section is a single box variable section. The elevation view of the middle span girder is shown in Figure 2.

The height of the pier is 9 m. All of the pier cross sections are rectangle sections with a size of 3.5 m × 7 m. The reinforcement layout of the pier bottom section is shown in Figure 3.

The bridge girder applies the cast-in-place cantilever construction method. The main construction stages are as follows: (1) substructure construction stage, (2) girder cantilever with blocks construction stages, (3) the 1st and 3rd span cast-in-place construction stages, (4) the 1st and 3rd span closure construction stages, (5) the middle span closure construction stage, and (6) the bridge completion stage. The

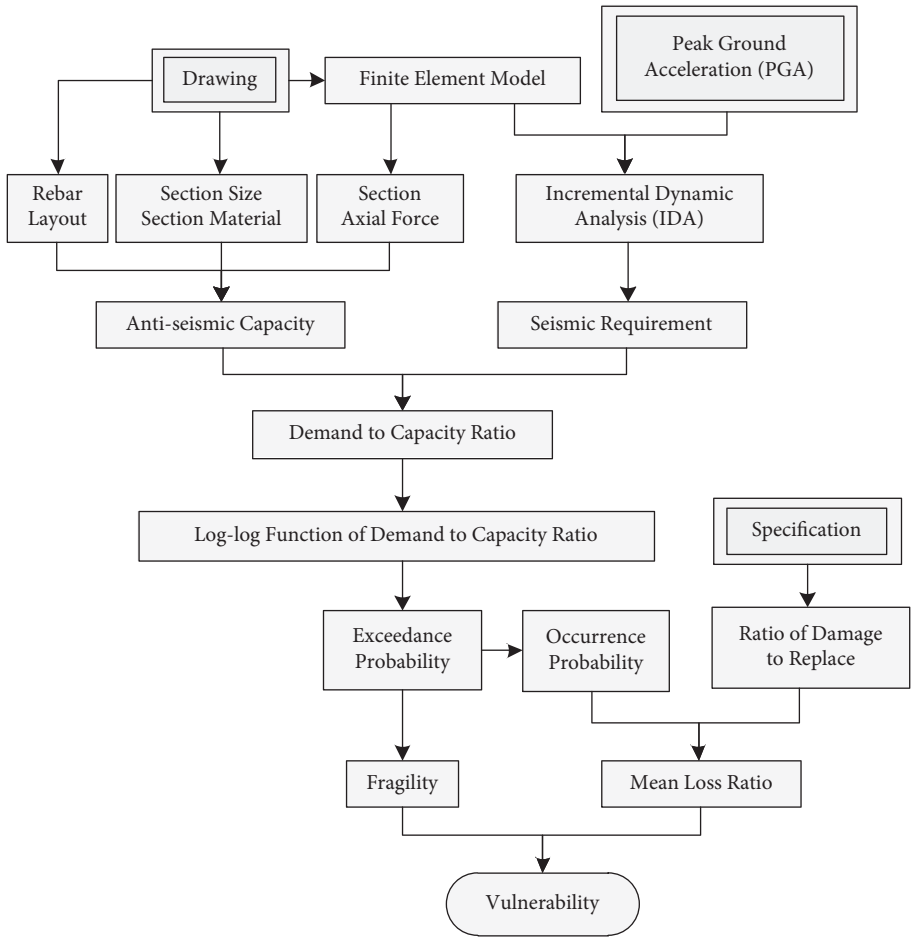

Figure 1: Flow chart of the vulnerability evaluation method.

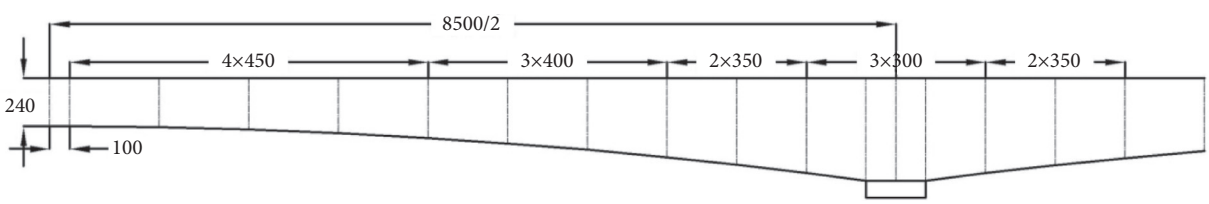

Figure 2: Elevation view of the middle span girder (dimension units: cm).

girder cantilever with blocks construction stages include the hanging basket, cast, prestress tension, and the other construction substages.

In reference to the practical seismic damage characteristics of the cast-in-place cantilever construction method, based on the case study bridge practical construction organization scheme, the seismic vulnerability of five typical construction stages are selected as the research object in this paper. The comparatively researched construction stages are listed in Table 1.

3.2. Finite Element Modeling. For this study, the finite element model of the bridge is developed using the software Midas Civil. The cushion caps, piers, and girders are modeled by beam elements, and their materials are C35 concrete, C40 concrete, and C60 concrete, respectively. The prestress steels in the girders are high strength low relaxation strands with a standard strength of 1860 MPa, and the posttensioned construction method is applied. The supports are simulated by elastic coupling. The soil-structure interaction is ignored. The Construction Stages function in the Midas Civil is applied to simulate the bridges at different construction stages by activating or killing the relevant element, boundary, and loads. The researched construction stages in this study are shown in Figure 4. The boundary condition is that the bridge is fixed at the bottoms of the cushion caps, which is shown as green points in Figure 4.

The modal information of the FEM for all the considered stages is listed in Table 2.

Twenty seismic records from five practical earthquakes that occurred in eastern China are selected as the seismic

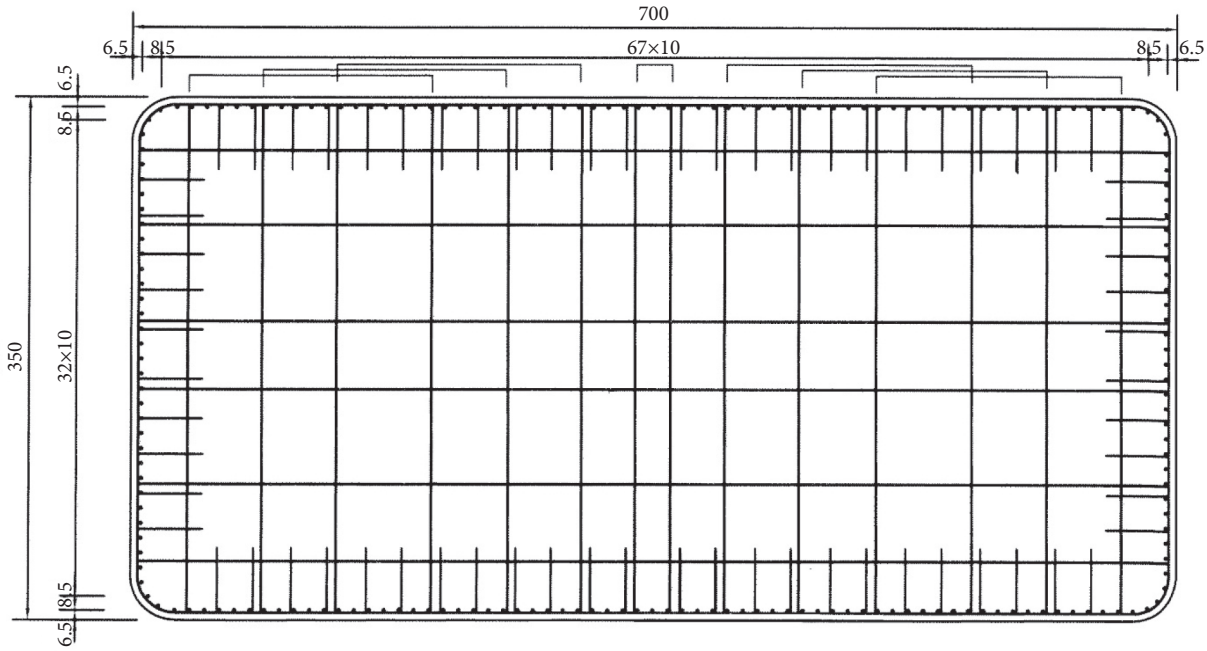

Figure 3: Reinforcement layout of the pier bottom section (dimension units: cm).

Table 1: Comparatively researched construction stages.

No.	Researched construction stage
1	Substructure
2	Middle cantilever
3	Long cantilever
4	Middle span closure
5	Bridge completion

excitation in the FEM software. Each of the records contains three record components, which are assumed to be oriented along the transversal, longitudinal, and vertical directions of the bridge. The identification of the considered seismic records is listed in Table 3. The seismic records data for this study are provided by Institute of Engineering Mechanics, China Earthquake Administration.

With regard to the relationship between the ground motion acceleration and the seismic fortification intensity [15–17], as well as for the structural probable damage situation, the PGAs are modified to 0.1 g, 0.2 g, 0.4 g, 0.8 g, and 1.0 g. The seismic response spectra of the seismic records are shown in Figure 5. The damping ratio used to develop the response spectra is 5%, and the response spectra are drawn from the twenty seismic records.

4. Case Study Bridge Seismic Vulnerability Evaluation

4.1. Antiseismic Capacity Analysis. To analyze the middle pier bottom section mechanical performance, some key parameters, such as the section shape, section size, concrete, rebar, rebar layout (as shown in Figure 3), and loading, are considered. The nominal moment-curvature [18] (which is called the computational curve in this paper) and the fitted double-linear moment-curvature (which is called idealized curve in this paper) relationships of the middle pier bottom section can be determined. Based on references [16, 19, 20], the first yield point, effective yield point, and ultimate point can be got. Then the first yield point and effective yield point can be connected into a line, and the line can be extended to the initial point; similarly, the effective yield point and ultimate point can be connected into a line. The above-mentioned two lines constitute the idealized curve. The middle pier bottom section moment-curvature relationships of the bridge completion stage are taken as the example, as shown in Figure 6.

The moment-curvature idealized relationship of the pier bottom sections is used to control the nonlinear behavior by the form of plastic hinges in the Midas Civil. The moment and curvature of the pier bottom sections will change along the idealized curve in Figure 6.

Based on reference [8], the first yield point, the effective yield point, the maximum moment point, and the ultimate point are selected as the damage boundary values in the seismic fragility evaluation process. The middle pier bottom section damage boundary values of the bridge completion stage are taken as the example and shown in Figure 6; the detail values are listed in Table 4.

4.2. Seismic Demand Analysis. In the seismic demand analysis process, the IDA method is applied. For the twenty seismic records, the PGAs are modified to 0.1 g, 0.2 g, 0.4 g, 0.8 g, and 1.0 g as the seismic excitation. So, there are 100 seismic load working conditions in total for every construction stage. After the finite element nonlinear time-history analysis in the Midas Civil, the transversal and longitudinal maximum moments of the middle pier bottom can be achieved. The IDA results of the middle pier bottom

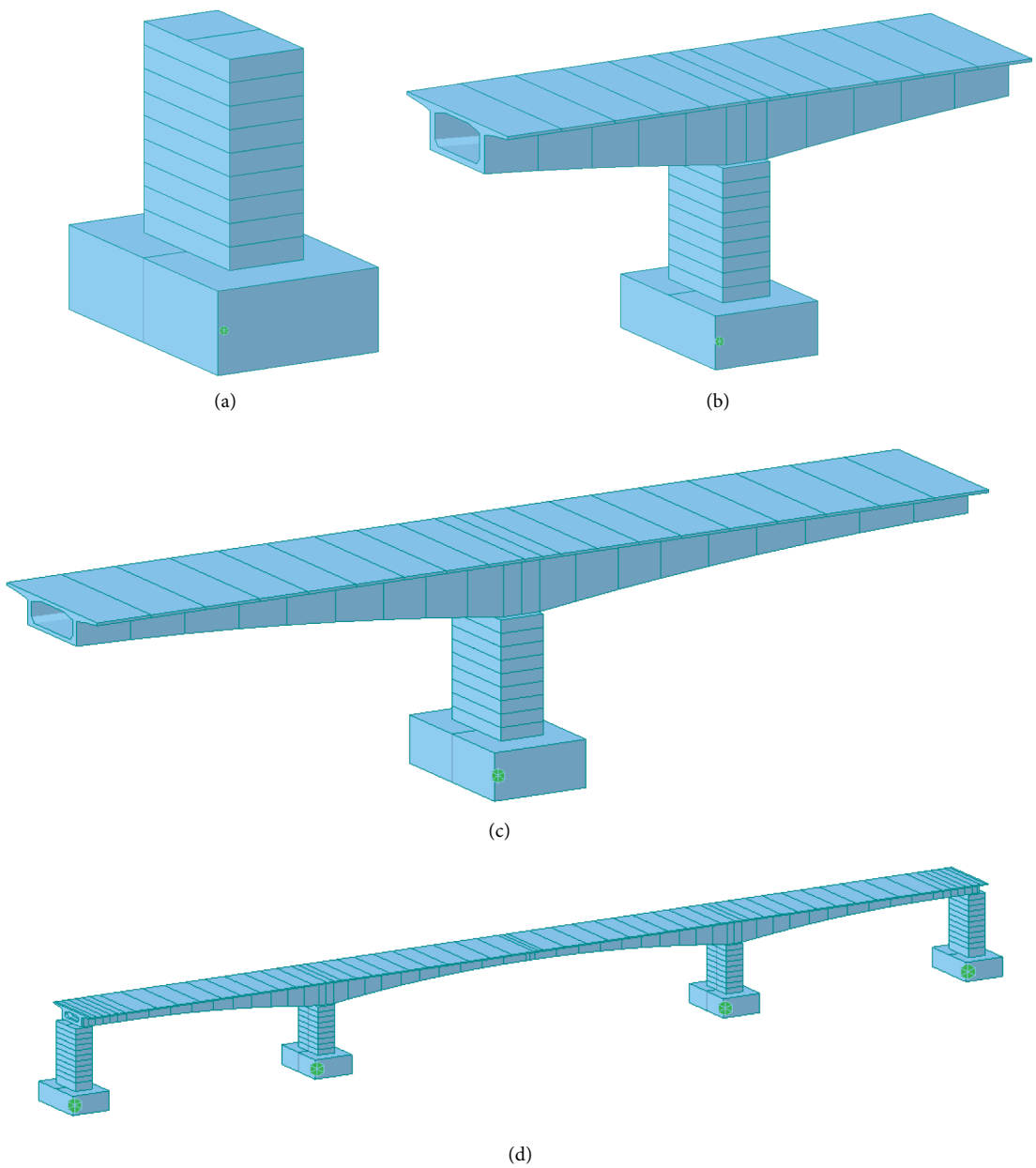

Figure 4: Researched construction stages for the case study bridge. (a) Substructure construction stage. (b) Middle cantilever construction stage. (c) Long cantilever construction stage. (d) Middle span closure construction stage and bridge completion construction stage.

at the bridge completion stage for twenty seismic excitations are taken as the example, as listed in Table 5.

Table 5 shows that for the case study bridge middle pier bottom, the transversal maximum moments are always larger than the longitudinal maximum moments. This may result in the transversal direction being more vulnerable than the longitudinal direction for the case study bridge.

4.3. Seismic Fragility Analysis. Based on the damage index demand for the capacity ratio method, the bridge seismic fragility situations at different construction stages are analyzed in this study. For each damage state, the natural logarithm of the input PGA to the 1 g ratio ($\ln(\mathrm{PGA})$) is regarded as the abscissa, and the natural logarithm of the demand to capacity ratio ($\ln(S_d/S_c)$) is regarded as the ordinate. Then, the log-log plot can be achieved. With the least square method, the linear functions can be fitted as shown in

$$\ln\left(\frac{S_d}{S_c}\right) = A * \ \ln(\mathrm{PGA}) + B, \tag{1}$$

where PGA is the ratio of the input PGA to 1 g; S_d is the seismic demand, which is the seismic response curvature of the middle pier bottom in this article (1/m); S_c is the

Table 2: The modal information of the FEM.

Construction stage	Modal no.	Frequency (Hz)	Mode shape	Mode shape description
Substructure	1	21.236		Middle pier longitudinal bends
	2	34.176		Middle pier transversal bends
	3	81.022		Middle pier longitudinal bends
Middle cantilever	1	2.378	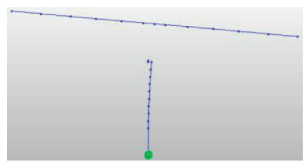	Middle pier longitudinal bends; main girder rotates around the supporter transversal direction
	2	3.539	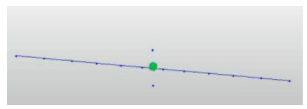	Main girder rotates around the supporter vertical direction
	3	5.932	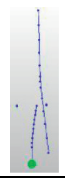	Middle pier transversal bends; main girder transversal bends
Long cantilever	1	1.161	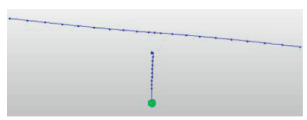	Pier longitudinal bends; main girder rotates around the supporter transversal direction
	2	1.458	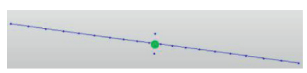	Main girder rotates around the supporter vertical direction
	3	2.570	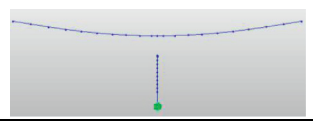	Main girder vertical bends
Middle span closure/ bridge completion	1	1.359		Main girder vertical bends
	2	2.421		One middle pier transversal bends; main girder vertical bends
	3	3.128		Middle piers transversal bends; main girder transversal bends

antiseismic capacity, which is the damage boundary curvature of the middle pier bottom in this article (1/m); S_d/S_c is the ratio of demand to capacity; and A and B are the coefficients in the linear function. The coefficients and standard deviations (SD) in the linear function fitting process are listed in Table 6.

Table 3: Identification of the considered seismic records.

Time (UTC + 8)	Epicenter position	Magnitude (Ms)	Depth (km)	Station position	Site condition
2011-01-19 12 : 07 : 43	N30.659, E117.099	4.4	6	N32.000, E119.199	Soil
				N31.700, E119.000	Soil
				N31.500, E119.300	Soil
				N31.600, E118.300	Soil
				N31.500, E118.300	Soil
2012-07-20 20 : 11 : 51	N33.04, E119.569	4.9	15	N34.400, E118.400	Soil
				N33.299, E119.300	Soil
				N32.799, E120.300	Soil
				N32.099, E119.699	Soil
				N33.799, E119.800	Soil
2013-11-23 13 : 44 : 11	N37.099, E120.019	4.5	10	N36.799, E118.900	Soil
				N36.400, E119.800	Soil
				N36.500, E119.400	Soil
				N36.799, E119.800	Rock
				N37.599, E121.000	Rock
2014-03-19 20 : 19 : 22	N24.049, E122.419	5.9	10	N26.600, E118.199	Rock
				N25.500, E119.800	Rock
				N25.700, E117.099	Rock
2014-05-21 08 : 21 : 13	N23.76, E121.489	5.9	20	N25.799, E116.400	Rock
				N25.500, E119.800	Rock

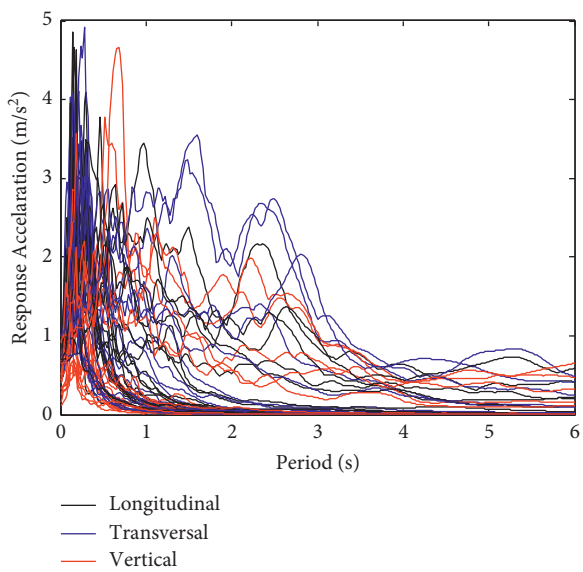

Figure 5: Seismic response spectra of the twenty seismic records.

The most common form of a seismic fragility function is the lognormal cumulative distribution function (CDF) [13]. The exceedance probability of $S_d/S_c > 1$ is

$$P_f = P\left(\frac{S_d}{S_c} > 1\right) = P\left[\ln\left(\frac{S_d}{S_c}\right) > \ln 1\right] = 1 - \Phi\left(\frac{\ln 1 - \mu}{\sigma}\right) = \Phi\left(\frac{\mu}{\sigma}\right), \quad (2)$$

where the mean value of the natural logarithm of the demand to capacity ratio is

$$\mu = \ln\left(\frac{S_d}{S_c}\right). \quad (3)$$

Additionally, the standard deviation of the natural logarithm of the demand to the capacity ratio is

$$\sigma = \sqrt{\frac{S_r}{n-2}}, \quad (4)$$

where S_r is the variance of natural logarithm of the demand to capacity ratio; n is the sample size of the natural logarithm of the demand to capacity ratio.

Based on equations (2)–(4), all the longitudinal and transversal exceedance probabilities of different damage states at different construction stages for different PGAs can be computed. Then, the seismic fragility of the bridge after comprehensive consideration of the longitudinal and transversal fragility curves can be determined. These curves are shown in Figure 7.

Figure 7 shows that for the substructure construction stage with a PGA of 0.4 g, the exceedance probabilities of the slight, moderate, extensive, and collapse damage states are about 8%, 5%, 0%, and 0%, respectively. This means, under the action of strong earthquakes, a bridge at the substructure construction stage hardly suffers from any seismic damage. Therefore, the antiseismic performance of this construction stage is excellent. For the middle cantilever construction stage and the long cantilever construction stage, the exceedance probabilities are similar, and the exceedance probabilities of the slight, moderate, extensive, and collapse damage states are about 80%, 79%, 60%, and 55%, respectively. This means that under the action of strong earthquakes, a bridge at the middle cantilever construction stage and the long cantilever construction stage usually suffers from seismic damage. For the middle span closure

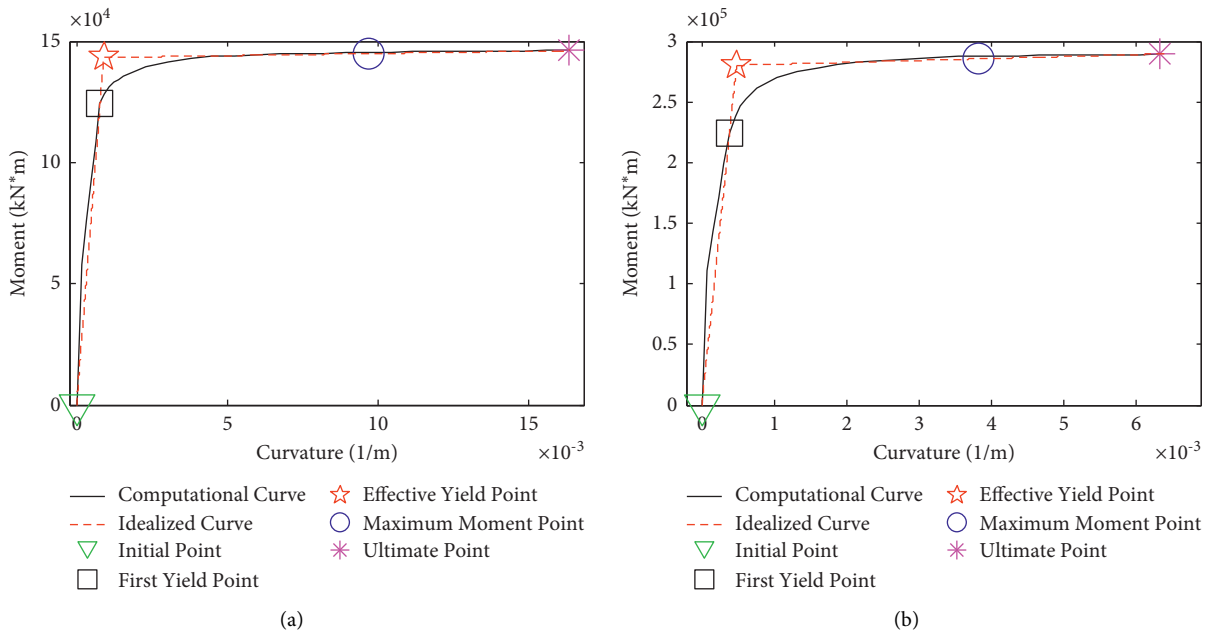

Figure 6: Moment-curvature relationships of middle pier bottom section (bridge completion stage). (a) Longitudinal moment-curvature relationships. (b) Transversal moment-curvature relationships.

Table 4: Damage evaluation indexes boundary values of the middle pier bottom (bridge completion stage).

Direction	Index	Unit	Slight damage	Moderate damage	Extensive damage	Collapse damage
Longitudinal	Curvature	1/m	7.82×10^{-4}	9.01×10^{-4}	9.70×10^{-3}	1.64×10^{-2}
	Moment	kN × m	1.24×10^{5}	1.43×10^{5}	1.45×10^{5}	1.46×10^{5}
Transversal	Curvature	1/m	3.84×10^{-4}	4.79×10^{-4}	3.59×10^{-3}	6.42×10^{-3}
	Moment	kN × m	2.25×10^{5}	2.80×10^{5}	2.85×10^{5}	2.90×10^{5}

Table 5: IDA results of the middle pier bottom (bridge completion stage).

Earthquake no.	PGA (g)	Transversal maximum moment (kN × m)	Longitudinal maximum moment (kN × m)
1	0.1	124715.30	41350.43
	0.2	249430.61	82700.87
	0.4	284632.28	143498.30
	0.8	295975.51	144432.25
	1.0	297487.94	144594.96
2	0.1	11055.41	9510.73
	0.2	22110.81	19021.46
	0.4	44221.62	38042.91
	0.8	88443.24	76085.82
	1.0	110554.06	95107.28
3	0.1	95882.67	116589.76
	0.2	191765.56	143736.31
	0.4	295770.93	144428.37
	0.8	303330.19	146002.37
	1.0	305830.99	147366.54
4	0.1	66169.98	43928.98
	0.2	132339.97	87857.97
	0.4	264679.60	143438.19
	0.8	293742.85	143818.36
	1.0	298630.06	144124.19

Table 5: Continued.

Earthquake no.	PGA (g)	Transversal maximum moment (kN × m)	Longitudinal maximum moment (kN × m)
5	0.1	111156.75	29670.38
	0.2	222313.50	59340.75
	0.4	286419.06	118682.54
	0.8	292862.12	144810.86
	1.0	297130.57	146277.70
6	0.1	93010.80	51934.77
	0.2	186021.60	103869.54
	0.4	284940.70	144977.70
	0.8	300716.87	149089.16
	1.0	303597.27	149702.63
7	0.1	93769.84	38333.40
	0.2	187539.68	76666.81
	0.4	284832.89	143386.89
	0.8	298734.72	145034.92
	1.0	302025.42	145959.40
8	0.1	104805.70	63977.45
	0.2	209611.40	127954.78
	0.4	286336.05	144716.45
	0.8	299258.12	146852.25
	1.0	301826.16	148718.42
9	0.1	76552.32	43323.90
	0.2	153104.64	86647.80
	0.4	281042.53	143559.38
	0.8	290690.42	144939.87
	1.0	294659.85	145455.57
10	0.1	138362.57	51103.98
	0.2	276725.15	102207.95
	0.4	292900.51	143900.92
	0.8	304259.53	147797.69
	1.0	307890.01	148617.52
11	0.1	85445.93	12397.04
	0.2	170891.86	24794.08
	0.4	283817.09	49588.17
	0.8	297073.82	99176.34
	1.0	297865.37	123970.42
12	0.1	83037.47	21897.19
	0.2	166074.93	43794.39
	0.4	283211.00	87588.77
	0.8	299157.07	143589.67
	1.0	300885.15	143720.47
13	0.1	66182.85	12746.55
	0.2	132365.70	25493.10
	0.4	264731.41	50986.20
	0.8	290176.33	101972.40
	1.0	297831.41	127465.51
14	0.1	29031.62	13745.21
	0.2	58063.24	27490.41
	0.4	116126.48	54980.83
	0.8	232252.97	109961.65
	1.0	280726.63	137451.98
15	0.1	24994.13	11864.14
	0.2	49988.26	23728.28
	0.4	99976.51	47456.56
	0.8	199953.03	94913.13
	1.0	249941.28	118641.41

Table 5: Continued.

Earthquake no.	PGA (g)	Transversal maximum moment (kN × m)	Longitudinal maximum moment (kN × m)
16	0.1	95988.89	93153.59
	0.2	191977.95	143593.86
	0.4	291159.88	152178.75
	0.8	341519.75	163385.42
	1.0	377424.26	168383.61
17	0.1	86019.30	54731.88
	0.2	172038.59	109463.75
	0.4	284273.13	146056.75
	0.8	303447.56	152343.62
	1.0	311396.04	155236.52
18	0.1	81512.48	80920.30
	0.2	163024.96	143487.87
	0.4	282744.71	152948.93
	0.8	318259.65	162343.61
	1.0	340261.62	165587.19
19	0.1	55297.90	71379.22
	0.2	110595.79	143302.00
	0.4	221193.84	148759.48
	0.8	306720.64	161842.72
	1.0	320054.15	169186.21
20	0.1	98706.94	70372.86
	0.2	197413.89	140745.71
	0.4	284130.64	145358.69
	0.8	305035.48	150225.29
	1.0	314483.53	151202.57

Table 6: Coefficients and standard deviations in the linear function fitting process.

Damage state	Parameter	Substructure	Middle cantilever	Long cantilever	Middle span closure	Bridge completion
Slight damage	A	1.000	3.313	3.438	2.827	2.959
	B	−0.329	6.523	6.383	8.066	8.158
	SD	0.900	3.595	3.589	3.321	3.393
Moderate damage	A	1.000	3.313	3.438	2.827	2.959
	B	−0.619	6.278	6.152	7.838	7.937
	SD	0.900	3.595	3.589	3.321	3.393
Extensive damage	A	1.000	3.313	3.438	2.827	2.959
	B	−3.146	3.973	3.955	5.673	5.922
	SD	0.900	3.595	3.589	3.321	3.393
Collapse damage	A	1.000	3.313	3.438	2.827	2.959
	B	−3.777	3.448	3.439	5.161	5.342
	SD	0.900	3.595	3.589	3.321	3.393

construction stage and the bridge completion construction stage, the exceedance probabilities are nearly the same, and the exceedance probabilities of slight, moderate, extensive, and collapse damage states are about 98%, 97%, 82%, and 78%, respectively. This means that under the action of strong earthquakes, a bridge at the middle span closure construction stage or the bridge completion construction stage always suffers from seismic damage, and it can easily suffer from extensive damage or collapse damage.

4.4. Seismic Damage Occurrence Probability. In Figure 7, the fragility represents the exceedance probability of a damage state, and it is the accumulated result of the occurrence probability of the damage state. Hence, the probabilities of occurrence of different damage states are

$$\begin{cases} p_1 = 1 - p_{f1} \\ p_2 = p_{f1} - p_{f2} \\ p_3 = p_{f2} - p_{f3}, \\ p_4 = p_{f4} - p_{f3} \\ p_5 = p_{f4} \end{cases} \tag{5}$$

where p_1, p_2, p_3, p_4, and p_5 are the occurrence probabilities of the no damage state, slight damage state, moderate damage state, extensive damage state, and collapse damage state and p_{f1}, p_{f2}, p_{f3}, and p_{f4} are the exceedance probabilities of the slight damage state, moderate damage state, extensive damage state, and collapse damage state, respectively. The occurrence probability curves of different states are shown in Figure 8.

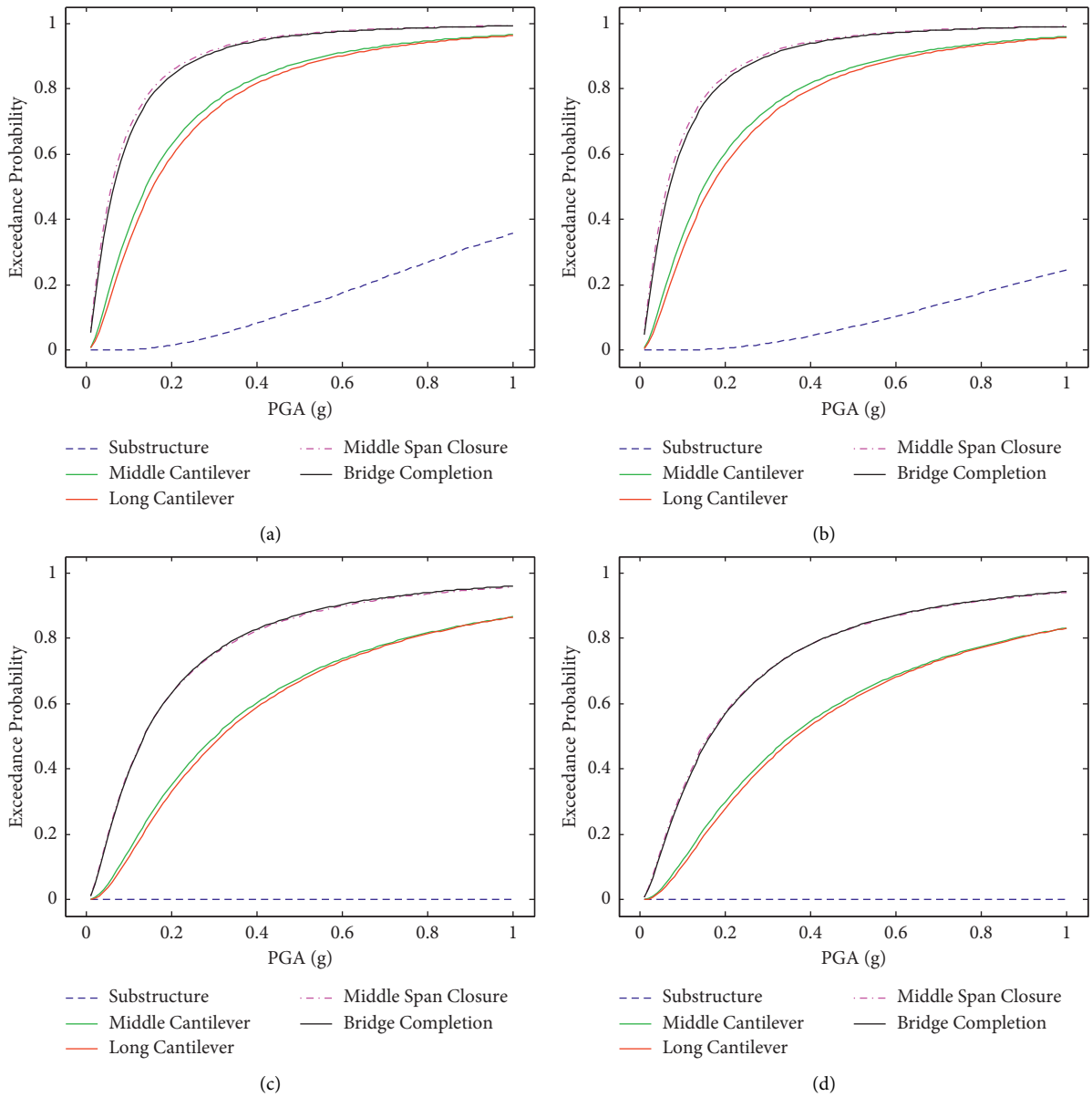

Figure 7: Fragility curves of different damage states. Exceedance probability of (a) slight damage state, (b) moderate damage state, (c) extensive damage state, and (d) collapse damage state.

Figure 8 shows that for different construction stages with different seismic intensities, the occurrence probabilities of the slight damage state and the extensive damage state are less than 12%, and the occurrence probabilities are low. This means that for the action of strong earthquakes, a bridge seldom suffers from extensive seismic damage or slight seismic damage. For different construction stages with different seismic intensities, the occurrence probabilities of the no damage state, moderate damage state, and collapse damage state are different, and the vulnerability evaluation and seismic defensive measurements should be conducted separately.

4.5. Seismic Mean Loss Ratio. The seismic loss ratio is the ratio of the lost value in an earthquake to the original value before an earthquake, the scope of which is 0 to 1. The mean loss ratio (MLR) is the mean value of the loss ratios. Based on the Pacific Earthquake Engineering Research Center (PEER) damage evaluation equation [17, 21], the bridge seismic mean loss ratio [22] is

$$\mathrm{MLR} = \sum_{j=1}^{k} \left(\frac{C_{s,j}}{I_s} * p_j \right), \tag{6}$$

where j is the damage state; k is the damage states total amount; $C_{s,j}$ is the recovery cost for damage state j; I_s is the replacement cost; $C_{s,j}/I_s$ is the loss ratio, which is the ratio of the recovery cost to the replacement cost; and p_j is the occurrence probability of damage state j.

In reference [22], the loss ratios of slight damage, moderate damage, and extensive damage for bridges are determined by their respective midvalues as 16%, 31%, and

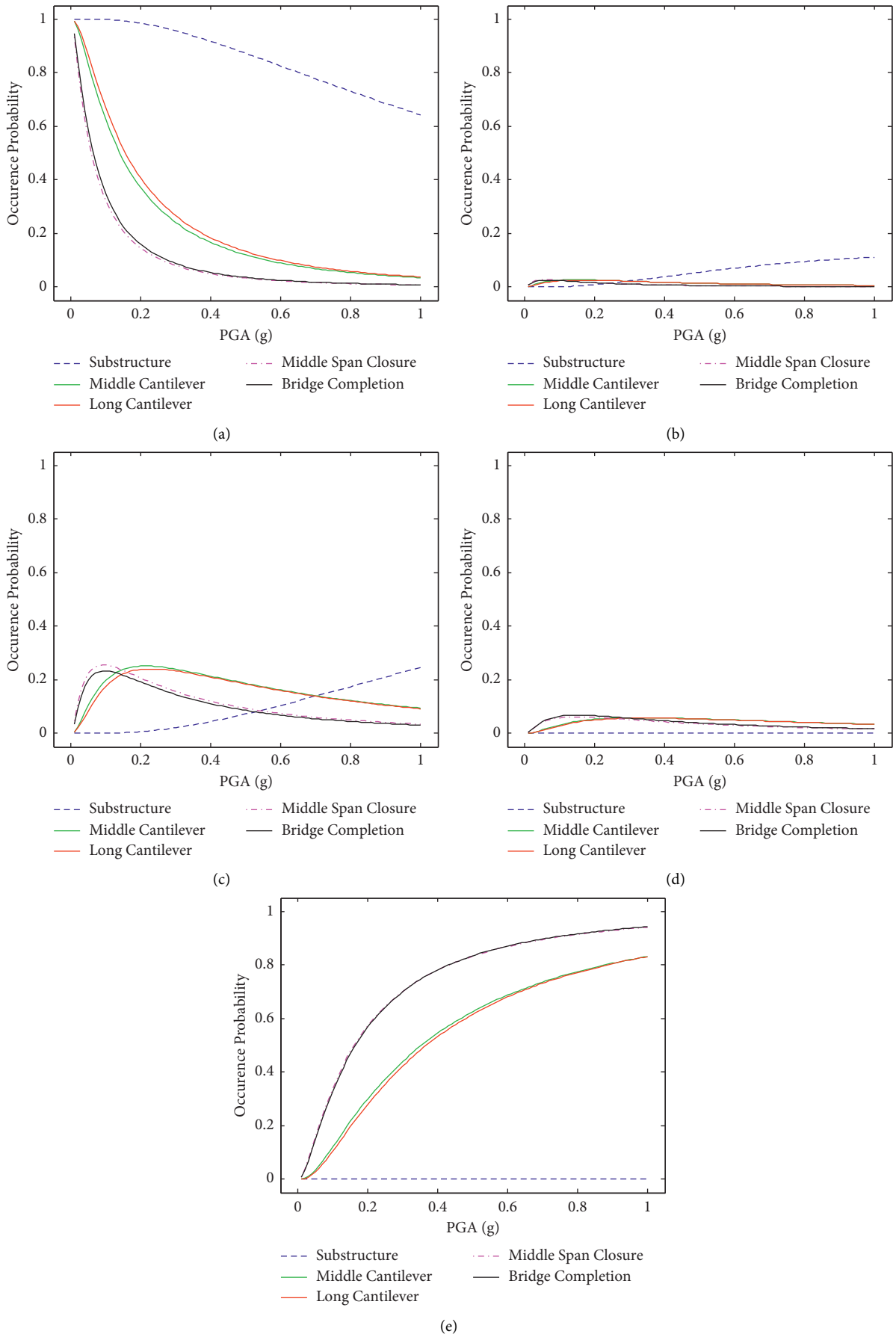

Figure 8: Occurrence probability curves of different damage states. Occurrence probability of (a) no damage state, (b) slight damage state, (c) moderate damage state, (d) extensive damage state, and (e) collapse damage state.

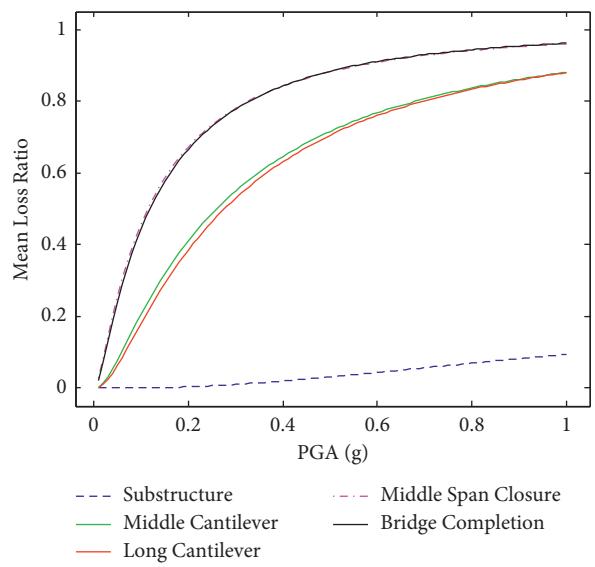

Figure 9: Seismic mean loss ratio curves of different construction stages.

56%. The loss ratios of no damage and collapse damage are 0% and 100%. Based on equation (6), the seismic mean loss ratios at different construction stages and for different PGAs can be determined. The seismic mean loss ratio curves of different construction stages are shown in Figure 9.

Figure 9 shows that the mean loss ratio curves of different construction stages are different. For the working condition of seismic PGA of 0.4 g, the conclusions can be acquired as follows. For the substructure construction stage, the mean loss ratio is about 5%. This means that under the action of strong earthquakes, a bridge at the substructure construction stage may only lose a small value. For the middle cantilever construction stage and the long cantilever construction stage, the mean loss ratios are similar, at about 65%. This means that under the action of strong earthquakes, a bridge at the middle cantilever construction stage and the long cantilever construction stage can lose more than half of the value. For the middle span closure construction stage and the bridge completion construction stage, the mean loss ratios are nearly the same, at about 85%. This means that under the action of strong earthquakes, a bridge at the middle span closure construction stage and the bridge completion construction stage may suffer from serious losses.

In addition, the plots shown in Figures 7 and 9 indicate that the seismic behavior of the bridge for middle cantilever and long cantilever construction stages are always similar, and for middle span closure and bridge competition, construction stages are practically the same. The reason is that the structural mechanical system for the middle cantilever and long cantilever construction stages are the same and so is the middle span closure and bridge competition construction stages. The structural mechanical system condition could also determine the structural mode shapes. As shown in Figure 2, the first and second mode shapes of the middle cantilever and long cantilever construction stages are the same, but the first and second modal frequencies are different. The first and second mode shapes of the middle span closure and bridge competition construction stages are the same. It can be summarized that the exceedance probability and mean loss rate are mainly determined by the structural mechanical system condition and the mode shapes but not the modal frequency.

5. Conclusions

In this study, the seismic vulnerability evaluation method of bridges under construction is proposed. Based on the case of a continuous girder bridge with the cast-in-place cantilever construction method, the seismic vulnerability evaluations of bridges at different construction stages are comparatively researched, and the conclusions are as follows:

(1) With the increase of the PGA, the system fragility and the mean loss ratio will increase.

(2) The fragility and vulnerability are mainly determined by the structural mechanical system condition and the mode shapes but not the modal frequency.

(3) For the bridge at the substructure construction stage, the seismic safety redundancy is large, and the seismic mean loss ratio is low. The bridge at the middle span closure construction stage or the bridge completion construction stage during strong earthquakes may suffer a serious loss, so many more seismic defensive measurements should be taken, and it is important to buy seismic insurance to transfer the possible seismic loss risk at these risky construction stages. For the bridge at the long cantilever construction stage or the middle cantilever construction stage, the seismic loss is moderate between the substructure construction stage and the cantilever construction stage.

(4) For the continuous girder bridges with the cast-in-place cantilever construction method, the mechanical system and characteristics, fragilities, and vulnerability of bridges at different construction stages are vastly different. Under the action of strong earthquakes, the vulnerability evaluation of bridges under construction should be conducted separately for different construction stages. Additionally, the seismic loss defensive measures for different construction stages should also be prepared differently.

Therefore, the research on the vulnerability evaluations for bridges at different construction stages under the action of strong earthquakes is useful. The research results can be applied to the evaluation of seismic risk occurrence probability and seismic loss ratio for the seismic insurance companies.

In addition, in future research, the aftershocks can also be considered by means of lengthening the ground motion records. The bridges under construction with the other construction methods can be researched with the construction stages vulnerability evaluation process proposed in this study. The influence of the bridge importance on the risk during the

construction stages can be further considered and discussed to make the research deeper and more comprehensive.

Data Availability

The data supporting the conclusion of the article are shown in the relevant figures and tables in the article.

Conflicts of Interest

The authors declare that there are no conflicts of interest regarding the publication of this article.

Acknowledgments

This work was financially supported by the National Key R&D Program of China (Grant no. 2018YFC1504602) and Scientific Research Fund of Institute of Engineering Mechanics, China Earthquake Administration (Grant no. 2018A02), and the support is greatly appreciated.

References

[1] W. B. Peng, J. D. Shen, X. Tang et al., "Review, analysis, and insights on recent typical bridge accidents," *China Journal of Highway and Transport*, vol. 32, no. 12, pp. 132–144, 2019.

[2] H. X. He, Y. F. Hu, and S. Wu, "Evaluation of structural vulnerability and resilience based on energy dissipation difference index and SIR model," *China Civil Engineering Journal*, vol. 53, no. 4, pp. 11–22, 2020.

[3] H. N. Li, H. Chen, and D. S. Wang, "A review of advances in seismic fragility research on bridge structures," *Engineering Mechanics*, vol. 35, no. 9, pp. 1–16, 2018.

[4] W. P. Wu, L. F. Li, S. C. Hu et al., "Research review and future prospect of the seismic fragility analysis for the highway bridges," *Earthquake Engineering and Engineering Dynamics*, vol. 37, no. 4, pp. 85–96, 2017.

[5] G. Lu, K. Wang, and W. Qiu, "Fragility-based improvement of system seismic performance for long-span suspension bridges," *Advances in Civil Engineering*, vol. 2020, pp. 1–21, Article ID 8693729, 2020.

[6] F. Wu, J. Luo, W. Zheng et al., "Performance-based seismic fragility and residual seismic resistance study of a long-span suspension bridge," *Advances in Civil Engineering*, vol. 2020, pp. 1–16, Article ID 8822955, 2020.

[7] J. Zhang and Y. Huo, "Evaluating effectiveness and optimum design of isolation devices for highway bridges using the fragility function method," *Engineering Structures*, vol. 31, no. 8, pp. 1648–1660, 2009.

[8] Y. Pan, A. K. Agrawal, and M. Ghosn, "Seismic fragility of continuous steel highway bridges in New York state," *Journal of Bridge Engineering*, vol. 12, no. 6, pp. 689–699, 2007.

[9] Y. Cao, Y. Liang, C. Huai, J. Yang, and R. Mao, "Seismic fragility analysis of multispan continuous girder bridges with varying pier heights considering their bond-slip behavior," *Advances in Civil Engineering*, vol. 2020, pp. 1–12, Article ID 8869921, 2020.

[10] C. Yang, W. L. Chen, and F. Teng, "The vulnerability analysis of bridge construction in aftershock area," *Engineering Mechanics*, vol. 33, pp. 251–256, 2016.

[11] R. Ohashi and O. Kiyomiya, "Examination of safety against earthquake at each stage of construction of long cable-stayed bridge," *Abstracts of Annual Meeting of JSCE*, vol. I, no. 531, 2016.

[12] W.-K. Hsu, W.-L. Chiang, Q. Xue et al., "A probabilistic approach for earthquake risk assessment based on an engineering insurance portfolio," *Natural Hazards*, vol. 65, no. 3, pp. 1559–1571, 2013.

[13] K. Porter, *Beginner's Guide to Fragility, Vulnerability, and Risk*, Springer Berlin Heidelberg, Berlin/Heidelberg, Germany, 2015.

[14] GB/T18208.4-2011, *Post-earthquake Field Works-Ppart 4: Assessment of Direct Loss*China Standard Press, Beijing, China, 2011.

[15] GB18306-2015, *Seismic Ground Motion Parameters Zonation Map of China*China Standard Press, Beijing, China, 2015.

[16] JTG/T2231-01-2020, *Specifications for Seismic Design of Highway Bridges*China Communications Press, Beijing, China, 2020.

[17] J. Liu, L. Zhang, H. Zhang, and T. Liu, "Seismic vulnerability analysis of single-story reinforced concrete industrial buildings with seismic fortification," *Structural Durability & Health Monitoring*, vol. 13, no. 2, pp. 123–142, 2019.

[18] A. Karamlou and P. Bocchini, "Functionality-fragility surfaces," *Earthquake Engineering & Structural Dynamics*, vol. 46, no. 10, pp. 1687–1709, 2017.

[19] M. J. N. Priestley and R. Park, "Strength and ductility of concrete bridge columns under seismic loading," *ACI Structural Journal*, vol. 84, no. S8, pp. 61–76, 1987.

[20] R. D. Zhao, Z. Q. Xu, J. B. Zou et al., "Seismic response analysis and performance evaluation of long-span cable-stayed bridge based on ANSYS," *Journal of Architecture and Civil Engineering*, vol. 35, no. 4, pp. 19–26, 2018.

[21] A. Karamlou, *Multi-scale Methodologies for Probabilistic Resilience Assessment and Enhancement of Bridges and Transportation Systems*, Ph. D. thesis, Lehigh University, Bethlehem, the USA, 2017.

[22] G. P. Cimellaro, A. M. Reinhorn, and M. Bruneau, "Framework for analytical quantification of disaster resilience," *Engineering Structures*, vol. 32, no. 11, pp. 3639–3649, 2010.

Hindawi
Advances in Civil Engineering
Volume 2021, Article ID 6638867, 24 pages
https://doi.org/10.1155/2021/6638867

Research Article

Explosive Performance Assessment of Buried Steel Pipeline

Seyed-Mohammad Seyed-Kolbadi,[1] Mohammad Safi,[2] Ayoub Keshmiri,[3] S. Mahdi S. Kolbadi ,[4] and Masoud Mirtaheri[4]

[1]*Department of Civil Engineering, Branch of Shahid Chamran, Technical and Vocational University of Golestan, Gorgan, Iran*
[2]*Shahid Beheshti University, Department of Civil and Environmental Engineering, Tehran, Iran*
[3]*Department of Civil Engineering, Branch of Aliabad, University of Golestan, Aliabad, Iran*
[4]*Department of Civil Engineering, KN Toosi University of Technology, Tehran, Iran*

Correspondence should be addressed to S. Mahdi S. Kolbadi; mahdi_kolbadi@sina.kntu.ac.ir

Received 13 December 2020; Revised 23 March 2021; Accepted 16 April 2021; Published 5 May 2021

Academic Editor: Edén Bojórquez

It is so important to consider the passive defense problem in any places there have been attacks by varies kinds of military threats and terrorists. It is certain that social security is related to overcoming on these perils and protection from country. Vital facilities are one of examples that should be protected. Vital facilities include roads, bridges, transmission lines, and telecom and media network. With attention to the intense dependent to export and transmit of oil and gas and with consideration of this point that many places are full of gas and oil resource, the protection of these lines is very important. In recent years, occurrence of varies kinds of terrorist accidents in relation to important structures in all the world causes that the explosion loads have special attention. Explosion can generate much damage with vibration in vast soil media. Thus, it is important to predict the dynamic impact load and its treatment response. With attention to regardable development of numerical methods in recent decades, it is possible to investigate the explosion effects on surface and underground structures. In this research, the newest applied method modeling of the explosion phenomenon has been investigated and comprehensive information has been earned. In this investigation, problem of explosion wave's propagation effects on buried pipes simulated by ABAQUS/CAE 6.10-1 was studied based on the finite element method. Surface explosion effects on gas buried pipe lines and their dynamic response have been investigated depending on properties and their characteristics. The variation of buried pipe depth effects and variation effects in soil properties around pipe in different cases has been considered, and the results are here. The results showed that in buried pipes under surface explosions, displacements, major stresses, and strains decrease in clay, dense, and loose sands with increase of buried depth. These results obtain that because of increase of closuring of pipes in soil when internal friction angle increases for a kind of soil, the stress on pipe rim will decrease also. It was also observed that the pipe performance in clay and loose sands is better than that in compacted sand, respectively.

1. Introduction

Vital arteries include roads, stairs, tunnels, transmission lines (water, oil, and gas), and communication and media networks. If one of the vital arteries is damaged, malfunctioning, urban activities, or relief work will be paralyzed during the crisis, thus increasing the loss of life and property. If the threatening factors of vital arteries are divided into two categories, natural and human factors, earthquakes, and explosions can be mentioned as examples of them, respectively. Over recent years, various terrorist incidents on important structures worldwide have caused special attention to be paid to explosive devices, in large cities that use underground spaces for highways, tunnels, and underground pipes. Therefore, it is essential to predict the dynamic impact loads and investigate the behavioral response of the structures. The reliable and economical design of structures requires a better understanding of the sophisticated and practical parameters of these structures. Due to the necessity and importance of these vital arteries, and if there is proper

information, we will be able to predict the possible effects of the explosion on them according to the specifications of the existing pipelines; in addition, if necessary, we should take steps to cure them. Also, with such information, the design of pipelines in the future can be more precise and safer, and the considerations related to the passive defense of vital arteries can be considered more effective. In recent years, there have been significant advances in developing numerical and laboratory methods for studying such systems. In the present study, comprehensive information will be obtained by examining the latest methods used to model the explosion phenomenon and the responses obtained from underground structures.

1.1. Modeling the Behavior of Materials. The simulation of the nonlinear part of the soil behavior has been performed using the modified Drucker–Prager plastic processor (cap) model. We also need to specify the level of yield, flow ωlaw, and hardening law. The rupture level of the Drucker–Prager is obtained from the following equation [1]:

$$F_s = t - p \tan\beta - d = 0. \tag{1}$$

$\beta(\theta, f_i)$ and $d(\theta, f_i)$ represent the angle of friction of the material and its bond, respectively, and can be defined as a function of temperature, θ, and others. T and P are equivalent to the amount of deviation stress and compressive stress, respectively [2] Table 1.

According to Iran's 2800 regulations, the selected base soil is type IV, which is considered soft soil. Then, by changing the effective parameters in the interaction and response of the structure, about 50 analyses with different parameters have been performed, which have been then displayed under different diagrams.

In addition, the used mechanical properties for simulation of steel pipeline can be found in Figure 1.

2. Numerical Solution Methods

2.1. Motion Equations. The most common solution to the problem of soil-structure interaction is the analysis based on the substructure method. In this method, the linear problem of soil-structure interaction is separated into a series of simpler subproblems, and then the results are combined using the principle of superposition. In the substructure isolation method [3], the whole soil-structure system, shown in Figure 2, is divided into three substructures. Substructure I includes the free area of the structure, substructure II includes the volume of soil removed, and substructure III includes the surface structure and its foundation. In the substructure isolation method, it is assumed that soil and structure interaction occurs only at the common boundary of the substructures (soil contact surface). The equation of motion of the substructures shown in Figure 2 can be written in matrix form (1). For harmonic excitation, mixed force vectors, and frequency displacement, the equation of motion for the soil-structure interaction system will be (8), when indices I, II, and III are related to the three substructures and indices i, w, and s, respectively, are related to the degrees of freedom corresponding to the nodes at the boundary of soil and structure, removed soil volume, and the upper part of the structure (Figure 3):

$$[M]\left\{\widehat{\ddot{u}}\right\} + [K]\left\{\widehat{u}\right\} = \left\{\widehat{Q}\right\},$$

$$\begin{bmatrix} C_{ii}^{III} - C_{ii}^{II} + X_{ii} & -C_{iw}^{II} & C_{is}^{III} \\ -C_{wi}^{II} & -C_{ww}^{II} & 0 \\ -C_{si}^{III} & 0 & C_{ss}^{III} \end{bmatrix} \begin{Bmatrix} u_i \\ u_w \\ u_s \end{Bmatrix} = \begin{Bmatrix} X_{ii}u_i \\ 0 \\ 0 \end{Bmatrix}. \tag{2}$$

2.2. The Site Response. For solving the problem of the construction response, it is necessary to make and solve the problem of eigenvalue for the model. In calculations related to volumetric waves from the submatrices calculated from the characteristics of each layer, they are used to form eigenvalue equations. In Kiran and Manoj's study [4], based on the construction model with horizontal layers and the assumption of linear deformation changes within each layer, the eigenvalue problem can be divided into two separate algebraic eigenvalue problems. These include the Riley wave, and the other one is for the movement of the Love wave. The equation of the eigenvalue for the motion of the Riley wave can be written in the following matrix form using the isolated soil model. There are two degrees of freedom in this model at each boundary between the two layers; thus, each n-layer system will have $2n$ degrees of freedom. In the previous equation, ω is the mode vibration angular frequency, K is the eigenvalue, and $\{V\}$ is the corresponding $2n$ component eigenvector. The dimensions of the matrices $[A]$, $[B]$, $[G]$, and $[M]$ are $2n \times 2n$, and these matrices are obtained by the summation of the matrices related to sublayers. If the depth of the j layer from the top is h_j and also the volumetric mass, shear modulus, and its constant are ρ_j, G_j, and λ_j, respectively, these matrices will be as follows:

Eigenvalue equations:

$$\left([A]K^2 + i[B]K + [G] - \omega^2[M]\right)\{V\} = 0,$$

$$\left[A_j\right] = \frac{h_j}{6}\begin{bmatrix} 2\left(\lambda_j + 2G_j\right) & 0 & \left(\lambda_j + 2G_j\right) & 0 \\ 0 & 2G_j & 0 & G_j \\ \left(\lambda_j + 2G_j\right) & 0 & 2\left(\lambda_j + 2G_j\right) & 0 \\ 0 & G_j & 0 & 2G_j \end{bmatrix},$$

$$\left[M_j\right]^{[l]} = \frac{\rho_j h_j}{6}\begin{bmatrix} 1 & 0 & 0 & 0 \\ 0 & 1 & 0 & 0 \\ 0 & 0 & 1 & 0 \\ 0 & 0 & 0 & 1 \end{bmatrix}. \tag{3}$$

Eigenvalue equation using numerical techniques:

$$\left([A]K^2 + i[B]K + [G] - \omega^2[M]\right)\{V\} = 0,$$

$$\left[G_j\right] = \frac{1}{h_j}\begin{bmatrix} G_j & 0 & G_j & 0 \\ 0 & \left(\lambda_j + 2G_j\right) & 0 & -\left(\lambda_j + 2G_j\right) \\ -G_j & 0 & G_j & 0 \\ 0 & -\left(\lambda_j + 2G_j\right) & 0 & \left(\lambda_j + 2G_j\right) \end{bmatrix},$$

$$\left[A_j\right] = h_j G_j \begin{bmatrix} \frac{1}{3} & \frac{1}{6} \\ \frac{1}{6} & \frac{1}{3} \end{bmatrix},$$

$$\left[G_j\right] = \frac{G_j}{h_j}\begin{bmatrix} 1 & -1 \\ -1 & 1 \end{bmatrix}, \tag{4}$$

$$\left[M_j\right]^{[c]} = \frac{\rho_j h_j}{6}\begin{bmatrix} 2 & 0 & 1 & 0 \\ 0 & 2 & 0 & 1 \\ 1 & 0 & 2 & 0 \\ 0 & 1 & 0 & 2 \end{bmatrix},$$

$$\left[M_j\right]^{(c)} = \frac{\rho_j h_j}{6}\begin{bmatrix} 2 & 1 \\ 1 & 2 \end{bmatrix},$$

$$\left[M_j\right]^{(l)} = \frac{\rho_j h_j}{2}\begin{bmatrix} 1 & 0 \\ 0 & 1 \end{bmatrix}.$$

Table 1: Mechanical properties of soil.

Mass density (kg/m^3)	Angle of friction	Flow stress ratio (MPa)	Dilation angle	Damping		Young's modulus (MPa)	Poisson ratio
				α	β		
1700	35	0.8	4.81	10	0	107.1e6	0.4

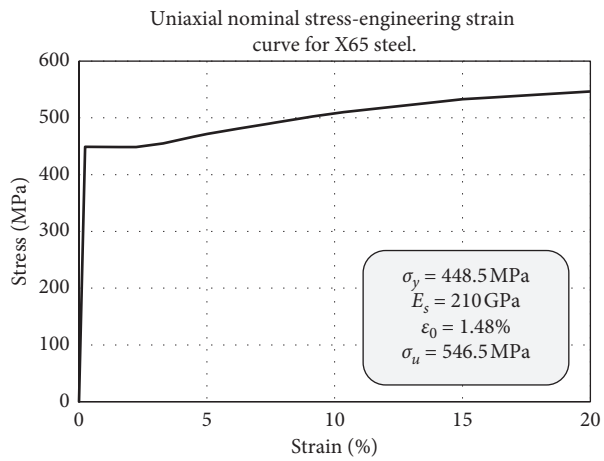

Figure 1: Mechanical properties of used wave-shaped connection in the FE numerical model.

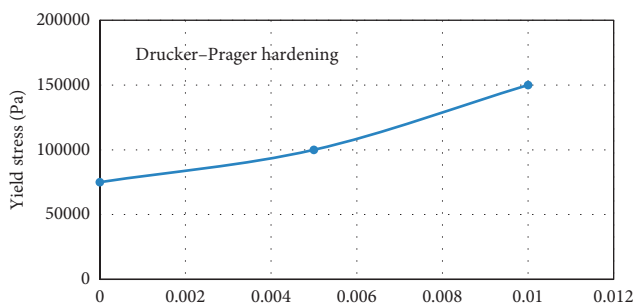

Figure 2: Drucker–Prager hardening model.

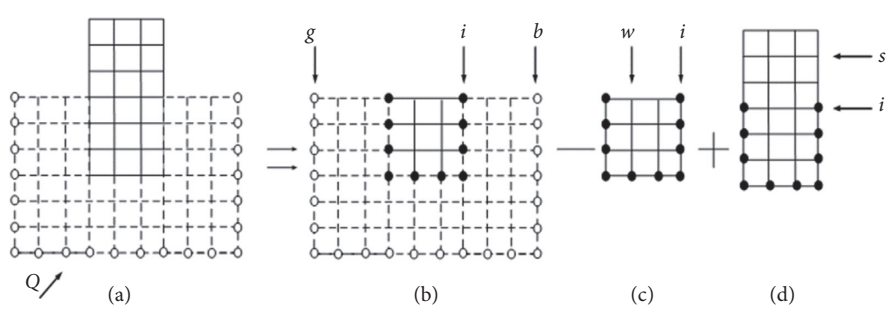

Figure 3: Separation of infrastructures to make calculations more simple: (a) total, (b) substructure I, (c) substructure II, and (d) substructure III.

Matrices $[M_j]^{[c]}$ and $[M_j]^{[l]}$ are the continuous and concentrated mass matrices, respectively. Using the numerical techniques suggested by Was, equation (5) of the eigenvalue can be obtained. By solving the equation, $2n$ Riley mode, as well as $2n$ wavenumber, is obtained. These values will be used to calculate the conditions of energy-absorbing boundaries in wave deformation motions on the system model screen. Based on the layered soil model, the eigenvalue problem for the motion of the Love wave can be written in the following form. In this waveform, at the boundary of each layer, there is only one degree of freedom. The following matrices $[A]$, $[G]$, and $[M]$ are derived from the following matrices.

Shi [5] wrote the equation of motion for SV inclined waves using the n-layer soil system. The equation of motion of the soil system, which is affected by SV waves, can be written as (18). Matrices $[A]$ $[G]$, and $[M]$ are obtained from the summation of the submatrices defined in equations (6) and (7). The matrix $[B]$ is obtained from the summation of the following submatrices, $[\overline{B}_j]$, defined as equation (19). If M_j and G_j are the binding and shear modulus of the J layer, respectively, the vector $\{P_b\}$ is a two-component vector, which defines the load vector at the bottom of the layer (rock bed). From the solution of equation (7), the displacement vector $\{u\}$ is obtained. At any distance x, the free-field motion can be achieved using equation (7) and δ is the

coefficient of modal participation that is calculated by applying the control motion at a point:

$$\left([A]K^2 + [\overline{B}]K + [G] - \omega^2[M]\right)\{u\} = \begin{Bmatrix} 0 \\ P_b \end{Bmatrix}, \tag{5}$$

$$\left[\overline{B}_j\right] = \frac{1}{2}\begin{bmatrix} 0 & \left(3G_j - M_j\right) & 0 & -\left(G_J - M_j\right) \\ \left(3G_j - M_j\right) & 0 & \left(G_j - M_j\right) & 0 \\ 0 & \left(G_j - M_j\right) & 0 & \left(3G_j - M_j\right) \\ -\left(G_j - M_j\right) & 0 & \left(3G_j - M_j\right) & 0 \end{bmatrix}, \tag{6}$$

$$\{u(x)\} = \delta.\ \exp(-ikx). \tag{7}$$

The semi-infinite semispace can be modeled by two methods, variable depth and viscous boundary at the base. Substructure methods are valid only for linear analyses. However, soils exhibit nonlinear behavior depends on strain in response to dynamic loading. Nonlinear soil behavior can be considered using the equivalent linear method proposed by Syed and Idris [6] and others. In this way, soil nonlinear characteristics are estimated by equivalent linear characteristics, including shear modulus and damping coefficient.

2.3. The Impedance. In the substructure isolation method, the equations of motion of the SSI system, including the impedance matrix $[X_{ff}]$, are shown in equation (8). In this method, the impedance matrix is calculated only for the boundary nodes (i nodes in Figure 3). At each analysis frequency, the impedance matrix is calculated by the dynamic compliance matrix. In three-dimensional problems, estimating the dynamic compliance matrix is reduced to the problem of finding the horizontal layer system response to loading at the boundary of the layers. After calculating the elements of mass and stiffness matrices, the equation of motion becomes (9). When C is the dynamic stiffness matrix ($C = K - \omega^2 M$), R is the impedance matrix of the energy-absorbing boundaries. Indices c and p are related to the degrees of freedom on the boundary line and the model environment, and $u_c$and u_p are the corresponding displacement sizes. The displacement of the outer nodes of model C is obtained from equation (10), where the index m is related to the Fourier harmonic degree. The vector under the coefficients of the modal participation depends on the $3n$ mode of displacement of the n-layer soil system:

$$\begin{bmatrix} C_{CC} & C_{CP} \\ C_{PC} & C_{PP} + R \end{bmatrix}\begin{Bmatrix} u_c \\ u_p \end{Bmatrix} = \begin{Bmatrix} Q_c \\ 0 \end{Bmatrix}, \tag{8}$$

$$\{u(r)\}_m = [w(r)]_m\{\Delta\}_m, \tag{9}$$

$$\{\Delta\}_m^T = \langle \alpha_1, \alpha_2, \ldots, \alpha_{3n} \rangle. \tag{10}$$

Furthermore, matrix $[W(r)]_m$ is a $3n \times 3n$ matrix that is a function of the radial distance from the axis of the model, the eigenvalue, the eigenvector, and the m degree function from the second type of Stanković functions [7]. Equation (11) is used with the modal participation vector to calculate the displacement at any point at an r radius distance from the model axis. At any frequency of analysis, a dynamic compliance matrix is a $3i \times 3i$ matrix for a system with i interactional nodes within the free field environment. The direct impedance calculation method demands to calculate the compliance matrix $[F_{ff}]$ for all the nodes involved. The impedance matrix $[X_{ff}]$ is then calculated by inverting the dynamic compliance matrix:

$$\left[X_{ff}\right] = \left[F_{ff}\right]^{-1}. \tag{11}$$

2.4. Structural Analysis. In this section, the structural and removed soil characteristics, used in the motion equation coefficient matrix equations (12), are calculated including the components A, B, and T. The removed soil and structure are modeled by standard finite element models, and then their dynamic characteristics are calculated. Within the soil-structure system, in the event of stable dynamic excitation, equation (12) is formed and dissolved at separate selected harmonic frequencies. In the case of harmonic excitation of results, the harmonic mixed conversion acceleration functions indicate the response of the whole system to the harmonic input motion at the control point. Transient motions, such as earthquakes, are analyzed using separated Fourier conversion technique. Utilizing these techniques, the base input motion that specified at N separate points is evenly distributed over the T period. The final result is obtained after summation in the following way:

$$\begin{Bmatrix} u_x(t) \\ u_f(t) \end{Bmatrix} = \mathrm{Re}\sum_{j=0}^{(N/2)}\begin{Bmatrix} u_{xj} \\ u_{fj} \end{Bmatrix}\exp\left(i\omega_j t\right). \tag{12}$$

For a single harmonic input, f separate values at L intervals can be calculated by Fourier inverse converting over D. Complete solution demands to form a linear equation system, and then it is solved for all FFT frequencies. This procedure requires considerable time and computational work. A high-level frequency and also an efficient method can be utilized so that the mixed response range, M, and Z are selected and calculated at several critical frequencies besides response values at other FFT frequencies. It can also be identified by interpolation [8].

2.5. Soil and Structure Interaction. Within studying the interaction problem, the dynamic response of the structure is affected by the interactions of the structure, the foundation, and the surrounding soil. There are two general substructural and direct methods available for analyzing interaction issues [9]. In the substructure method, the entire infinite environment is modeled; after calculating the soil impedance matrix, it will be appended to the dynamic stiffness of the structure. This process will make the problem more straightforward to figure out and more comfortable with calculating. Under the direct method, only a part of the soil environment, which is close to the structure, is modeled [9]. In this method, complex geometric shapes, changes in soil properties, and nonlinear behavior of the environment can be considered. Inside the analysis of the time domain, nonlinear behavior of the soil and structure materials can also be considered.

This study operates the conventional model in defining the interaction of contact surfaces, the Columbus friction model. The model has been applied using the contact element, which will be explained below. The Columbus friction model determines the frictional behavior between contact surfaces utilizing a friction coefficient μ. The default coefficient of friction is zero, so the tangential displacement will be zero until the surface tension exceeds a critical value for shear stress, and this depends on the vertical contact compression and is defined according to the following equation:

$$\tau_{\text{crit}} = \mu\rho, \tag{13}$$

where μ implies the coefficient of friction and $\rho$is the contact compression between the two surfaces. This equation determines the extreme value of shear stress for the contact surfaces involved in the collision. As long as the shear stress between them is equal to the frictional shear stress, the contact levels will not slide upon each other, as displayed in the following behavioral diagram (Figure 4).

Soil and structure interaction is significant, particularly for large and massive structures that have been built in soft soil. When affected by a dynamic load, a dynamic reaction of the soil and structure complex signifies a function of the dynamic characteristics, induced forces, and stimuli, and the dynamic model of the system which involved the dynamic model of the structure linking with the dynamic model of the environment. Interaction is a boundary value problem.

Therefore, it requires an infinite environment model; however, infinite modeling of the environment is not

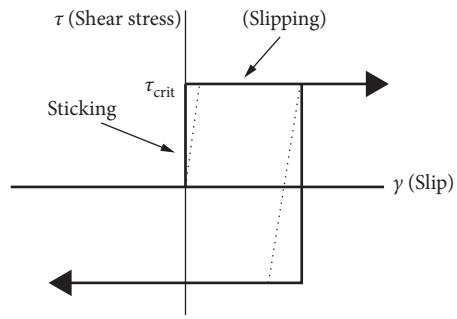

Figure 4: The frictional behavior of contact surfaces.

achievable. Hence, some terms must be considered that by a partial model of the infinite environment, the state of radiation (i.e., the waves are not reflected from the infinite environment) is satisfied. If the force, displacement, and dynamic stiffness upon the infinite boundary are displayed with $P(x, t)$ and $U(x, t)$ $K(x, t)$, respectively, the following equation is settled:

$$K(x,t) = \frac{P(x,t)}{U(x,t)}. \tag{14}$$

The purpose of the study soil and structural interaction is to obtain the dynamic stiffness and shape of the wave motion in the meeting points of soil and structure. The direct solution method for studying soil and structure interaction is based on the formulation of finite elements for soil and structure. This feature emphasizes the importance of the method in the topic of the interaction of soil and structure. Another significant point is the ability of the finite element method to consider nonlinear effects, both material and geometric. This makes the method one of the most potent numerical methods in structural analysis.

2.6. Loading Surface Blast. When an explosion occurs under ideal conditions of the theory, in the vicinity of the solid surface, waved shape will be hemispherical (Figure 5). (It should be noted that during an explosion within the air, the wave front is spherical.) Therefore, the energy of the blast wave is concentrated into a smaller area. For this purpose, all the relations obtained for blasting in the air can be utilized by doubling the weight of the explosives. However, in cases where the ground surface is firm and impermeable, laboratory tests are recommended.

The parameters of the blast wavefront are significant. The analytical solution of these parameters was first expressed by Huganiot and Rankine to describe shocks in the ideal gas. These equations are expressed for the velocity of the wavefront U_s and maximum dynamic compressionq_s as follows [10]: p_s p_0, and a_0 are the static overcompression, atmospheric compression, and velocity of sound, respectively, within the air under atmospheric compression. The scaling distance, Z, is defined as follows: [$R3$] is the actual distance from the center of the explosive to the target point, and W is the charge mass in kilograms of TNT. Utilizing Z allows us to have a concise and practical expression of the blast wave for various situations [10]:

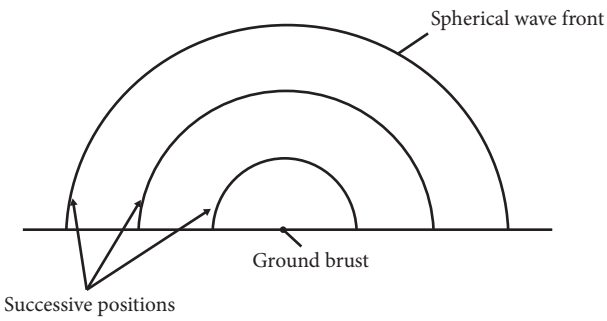

Figure 5: The hemispherical wave in superficial explosion.

$$U_s = \sqrt{\frac{6p_s + 7p_0}{7p_0}} \cdot a_0,$$
$$q_s = \frac{5p_s^2}{2(p_s + 7p_0)}, \tag{15}$$
$$Z = \left(\frac{R}{W^{(1/3)}}\right).$$

An equivalent TNT mass is required before the parameters can be extracted for an explosion. There are several ways to express equivalent TNT, but the simplest is the ratio of the specific mass energy of actual explosives to the specific mass energy of TNT. The specific gravity energy of TNT is equal to 6700 kJ/kg [11]. Other parameters of the blast wave include the positive phase duration T_s and the positive impulsei_s, which is the area under the compression-time diagram from time $t_a$to the end of the positive phase [11]. A standard method for extracting blast wave parameters is to practice graphs provided in some sources, such as TM5-1300 [10]:

$$i_s = \int_{t_a}^{t_a+T_s} p_s(t)\mathrm{d}t,$$
$$i_s^+ = \int_{t_a}^{t_a+t_0^+} [P(t) - P_a]\mathrm{d}t, \tag{16}$$
$$i_s^- = \int_{t_a+t_0^+}^{t_a+t_0^+ + t_0^-} [P_a(t) - P(t)]\mathrm{d}t.$$

There are many relations to maximum overcompression due to conventional (chemical) explosions based on researchers' explosive applied. Kiran's relation to the traditional chemical explosion is given [4]: maximum overcompression curves (as well as the curves of other parameters of the blast wave) exist as a function of the distance measured in 1300-500 related to the defense organization. And the maximum overcompression can be obtained by utilizing them (Figure 6):

$$\frac{P_S^+}{P_0} = \frac{808\left[1 + (Z/4.5)^2\right]}{\left\{\left[1 + (Z/0.048)^2\right]\left[1 + (Z/0.32)^2\right]\left[1 + (Z/1.35)^2\right]\right\}^{0.5}}. \tag{17}$$

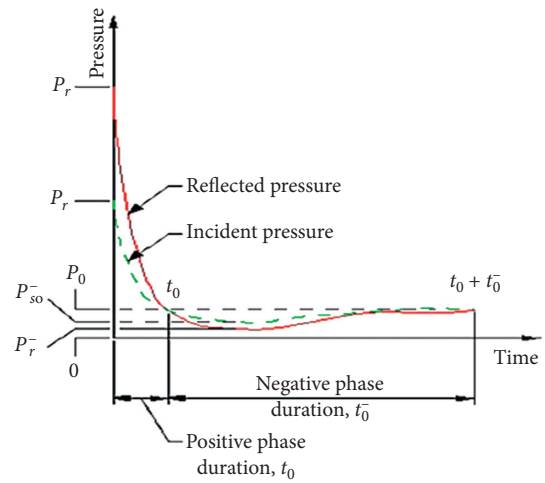

Figure 6: The ideal blast wave.

When an explosive device explodes on the surface of the earth or at a very short distance from it, the blast wave will ideally have a hemispherical wavefront, which is different from the spherical wavefront obtained in an aerial explosion [10]. Therefore, the released energy is applied to a smaller surface, and corrective coefficients must be applied to the air blast equations to obtain the overcompression in the surface explosion. Within 1963, Newmark proposed the following relation for calculating the maximum overcompression in chemical surface explosions:

$$P_s = 6784\frac{W}{R^3} + 93\left(\frac{W}{R}\right)^{0.5} \text{(bars)}, \tag{18}$$

where P_s is the overcompression, W is the equivalent weight of TNT (tons), and R is the distance from the center of the explosion on the ground to the desired point in terms of meters (Figure 7).

In studies conducted by various researchers such as Bulson, Bashara, and Henrich on the case of blasts, experiments were reported based on the amount of explosive equivalent TNT; therefore, it seems essential to provide a correlation to equate other explosives with TNT. The mass of explosives can be converted to TNT using the combustion temperature [12]:

$$w_{\mathrm{TNT}} = \frac{H_{\mathrm{EXP}}}{H_{\mathrm{TNT}}} w_{\mathrm{EXP}}, \text{(chemical explosion)}. \tag{19}$$

$$w_{\mathrm{TNT}} = k_j W_j,$$
$$k_j = \frac{0.5}{0.7}, \text{(nuclear explosion)}. \tag{20}$$

In these relations, w_{TNT}, H_{TNT}, H_{EXP}, w_{EXP}, and W_j are equivalent to TNT weight, TNT combustion temperature, the explosive combustion temperature, the weight of the explosive, and the energy equivalent of a nuclear explosion (e.g., the amount of TNT T, which produces energy equivalent to the energy of a nuclear blast), respectively. Also, K_j is a factor related to the amount of actual energy released as a blast wave (a blast wave of nuclear explosives

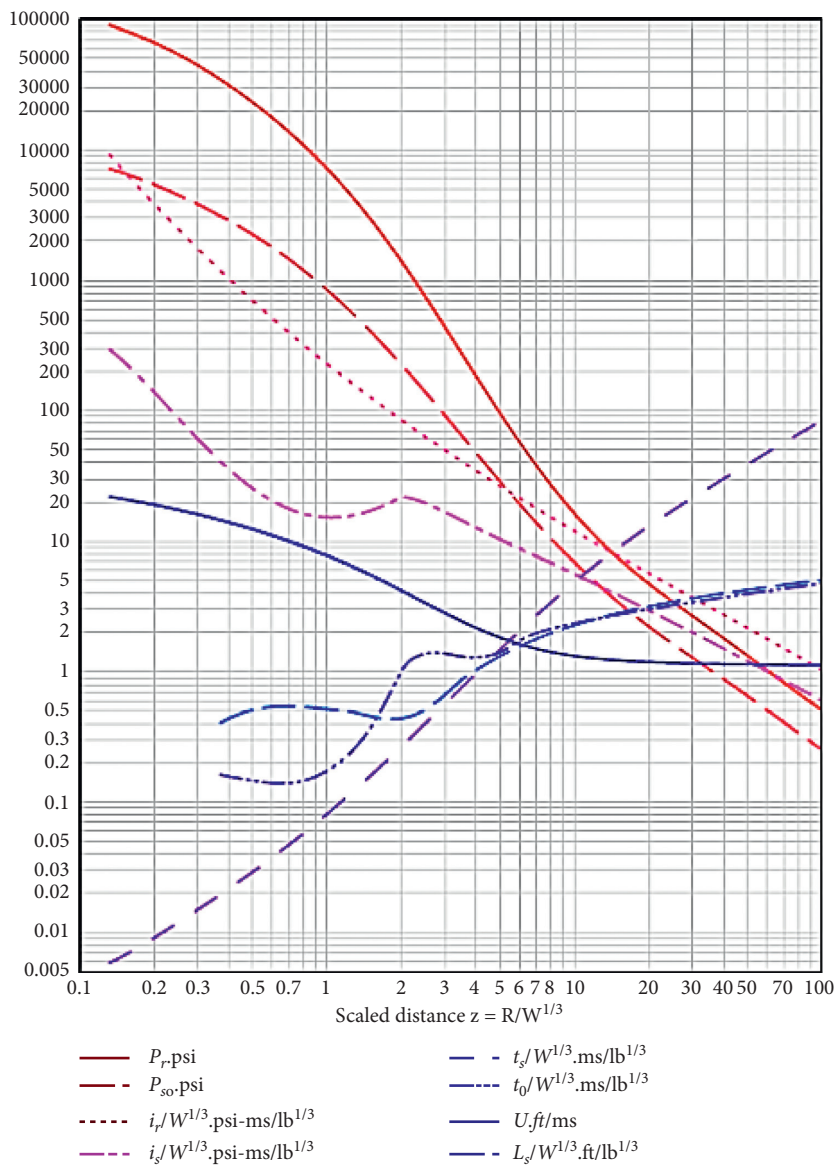

Figure 7: Spherical blast wave parameters, at sea level TM5-1300 (1969).

accounts for 70% of total energy, and the rest of it is wasted in the form of light and radiation) Table 2 [13].

2.7. Study of the Propagation of Blast Waves in the Soil Environment. The compressive waves created due to the explosion propagate in the soil environment, and colliding with the soil causes the soil to crumble and flow [14]. After the explosion, the resulting compressive wave propagates rapidly at a velocity close to sound velocity (about 300 m/s). This wave puts a compression of about 1000 pounds per square inch. Other letters are waves of tension or shock. The boundary impact between two different materials on how the wave propagates can be significant. Estimating the relative amplitude and directions in which the waves are reflected or refracted at the boundaries is available, utilizing the relations obtained from the theory of elasticity. Using the following equation also holding wave velocity and mass density, we can obtain the relation between A_i and A_r where c, ρ, and A_i are the velocity of the wave, density, and the amplitude of the initial stress wave, respectively. Moreover, A_r is the amplitudes of the reflected stress wave:

$$\frac{A_r}{A_i} = \frac{\rho_1 c_1 - \rho_2 c_2}{\rho_1 c_1 + \rho_2 c_2}. \tag{21}$$

The behavior of soil under dynamic loading is one of the most exciting topics for engineers in mines, buildings, and defense structures. Generally, the soil is a three-phase mixture of solid mineral particles, water, and the air. Connected or separated solid particles form the soil skeleton. Water and air are located among the cavities between solid particles of soil. Soil is the three-phase mixture; that is why it is challenging to predict the deformation of soils; not only is

Table 2: Conversion coefficient for different explosives.

HBX2	Minol 2	Composition B	Amatol	TNT	Explosive material
1.30	1.34	1.04	1.04	1	Conversion coefficient

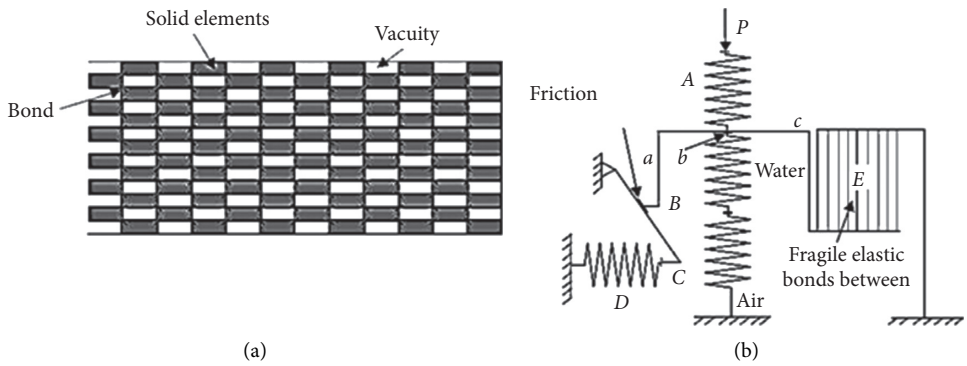

Figure 8: Wang three-phase behavior model for blast load: (a) conceptual model; (b) mathematical model.

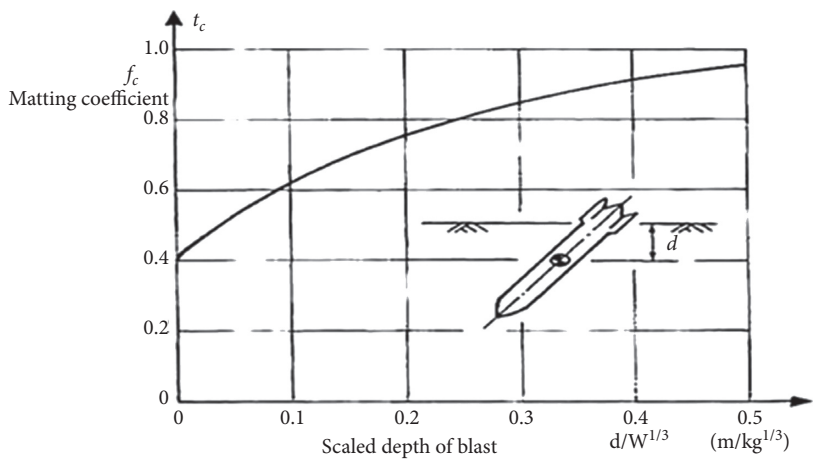

Figure 9: Mating coefficient.

the skeletal structure complex, but the properties of each component are fundamentally different. The different deformation characteristics of each phase and soil-structure make the soil deformation mechanism strongly dependent on the ratio of components in the soil and loading conditions. As a result, the mechanism of deformation of saturated and unsaturated soils is different, and such a difference in dynamic loading will be much more noticeable than static loading.

Both the mechanisms of skeletal deformation and the deformation of all soil phases affect simultaneously. However, in different loading stages and depending on the different ratios of components in the soil, one of the mechanisms is dominant so that the other mechanisms can be ignored [15]. For dry soils, which include a large amount of air and have a low percentage of water, the first mechanism prevails when subjected to static loading or slow dynamic loading. The initial compaction of the air is extreme. However, by increasing compression, the bonds between the soil particles are deformed; furthermore, the soil skeleton is damaged. Such soil is considered dense soil. Then, the second mechanism becomes more critical while the first mechanism gradually disappears [16].

The extraordinary dependence of soil properties on loading conditions makes it tough to develop a unique model for the deformation of soils under dynamic loading, particularly for high explosion rate loading, which varies significantly in different mass charge situations under loading conditions. Within an explosion, the soil close to the mass charge is deeply compacted. Hence, a high-stress wave is generated and propagates outward into the soil. As the distance from the charge increases, the stress wave decreases rapidly, and as a result, the soil compaction decreases. Therefore, in areas close to the charge, the second mechanism is predominant. In contrast, with increasing distance from the mass charge, the first mechanism becomes more and more significant and finally dominates the deformation of the soil. The extent of the nearby area depends on the

Table 3: The value of the reduction coefficient.

Reduction coefficient (n)	Soil type
1.5	Saturated clay
2.5	Semisaturated clay and silt
2.5	Very dense sand (dry or wet)
2.75	Dense sand (dry or wet)
3	Loose sand (dry or wet)
3.25	Very loose sand (dry or wet)

fundamental characteristics of the soil. Soil deformation mechanisms under static and transient loading have been studied over the years, and many models have been proposed to describe soil behavior under such loads.

However, insufficient research studies have been conducted on soil behavior under transient loads, such as explosion loads, due to these complexities. Modeling the soil response to an extremely variable pressure requires a robust soil model because new behavioral models typically cover a small range of deformations. Besides, in such high-stress conditions, in the vicinity of the charge, it is illogical to consider the rigid materials for the soil particles considered in ordinary soil dynamics. Instead, the solid phase change should be regarded in the soil behavior model. Based on Kandaur's conceptual analysis of soil deformation, a three-phase behavioral model for shock loading was developed by Wang (2003) to provide all of these requirements. In this model, the soil is considered a three-phase system consisting of solid particles, water, and air, in which the climate fills the solid particles form the soil skeleton, and the space between the particles is filled by water and air. The solid phase is considered plastic. Since the blast load duration is concise and there is not enough time for the water and air to escape from the soil particles, the relative displacement of the air-water and soil skeleton is neglected. Therefore, the model is suitable for describing soil behavior under normal blast loading [17].

In Figure 8, elements A, B, and C represent the deformation of the solid particles, water, and air, respectively, and elements D and E expose the friction and adhesive strength between the solid particles. The bonds between solid particles have been represented by a series of strings. Elements A, B, and C reflect the second deformation mechanism, and elements D and E are related to the first deformation mechanism. Based on the preceding modeling, a soil model for shock loading is obtained, which includes the following: equation of state (EOS), stress-strain relation, resistance model, and failure model for soil skeleton [18]. Different techniques are available in the technical literature to model a blast wave on buried structures. These impacts are in the form of displacement waves, acceleration, or compression. Naturally, the source of all methods is the same and is accomplished by solving the shock wave propagation equations in the soil environment. Of course, these relations are also interchangeable. The maximum amount of particle displacement (x) in terms of meters, at a distance of R (meters) from the source of the explosion, entirely or relatively buried, can be estimated from relation (22), where w is the mass of the explosive material in kilograms, c is the

Table 4: Models built to analyze the sensitivity of soil model dimensions.

Height (m)	Width (m)	Length (m)	Model no.
100	100	100	1
50	100	100	2
25	50	100	3
15	25	50	4

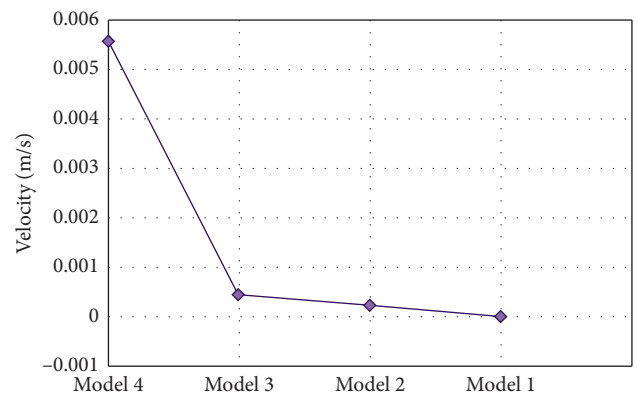

Figure 10: Graph of wave velocity values at the farthest nodes of different models.

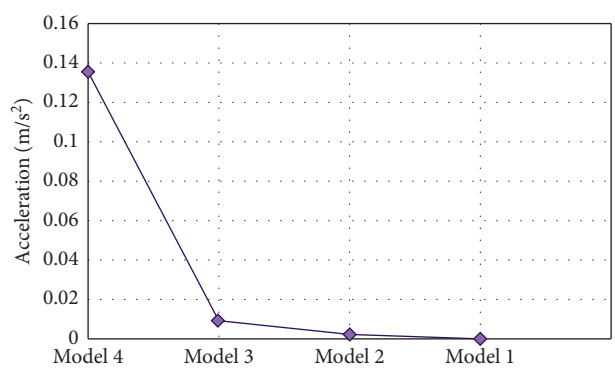

Figure 11: Graph of wave acceleration values at the farthest nodes of different models.

seismic wave velocity in meters per second, f_c is the coupling coefficient, calculated from Figure 9, and n is the dimensionless reduction coefficient; from Table 3, it is obtained that [19]

$$\frac{x}{w^{(1/3)}} = 60 \times \frac{f_c}{c}\left(\frac{2.52R}{w^{(1/3)}}\right)^{1-n}. \tag{22}$$

Also, the maximum velocity of particles in meters per second at a distance of R (meters) from the explosion source was calculated from equation (23). Moreover, the maximum pressure of the free field was determined based on equation (24). P is the density of the soil (kg/m^3), C is the load wave velocity (m/s), and P_0 is in pascals. The loading wave velocity C depends on the velocity of the seismic wave and the maximum particle velocity. C is high at short distances

Table 5: Characteristics of soil types used in the analyzes.

Soil type	γ (kg/m^3)	C (kPa)	ϕ	E (MPa)	υ	α	k	β	K	Ψ
Soft sand	1600	0	35	7	0.4	0.27	0	54.81	0.8	54.81
Hard sand	2000	0	25	14	0.3	0.19	0	44.53	0.85	44.53
Clay	1800	20	0	4	0.3	0	23.09	0	1	0

Table 6: Steel mechanical properties.

Tank material	γ (kg/m^3)	E (GPa)	υ	F_y (MPa)	F_u (MPa)
Steel X65	7850	203	0.3	448	530

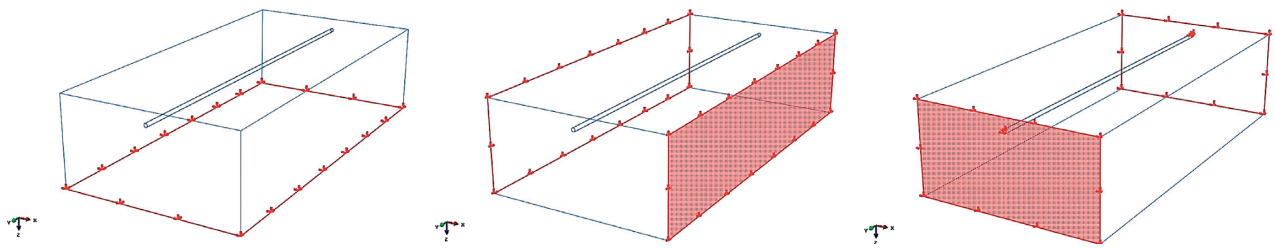

(a) (b) (c)

Figure 12: Conditions of symmetry at the lateral boundaries of the soil.

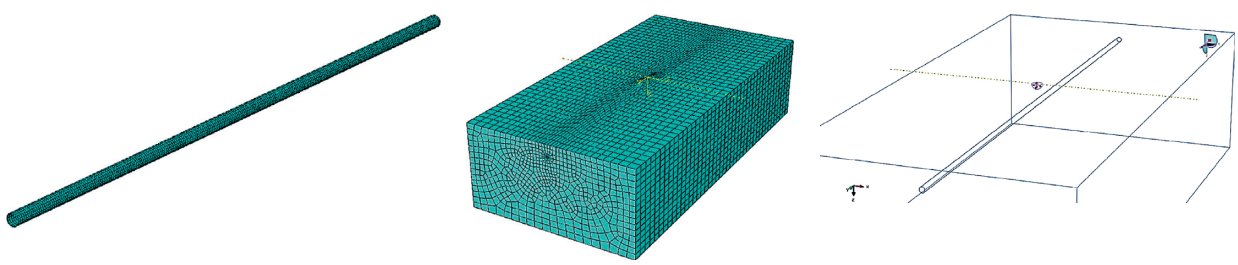

(a) (b) (c)

Figure 13: Place of blasting and meshing of soil and pipes.

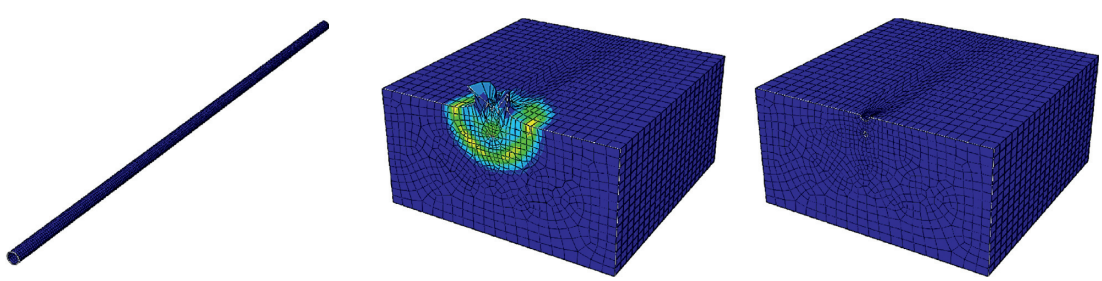

(a) (b) (c)

Figure 14: Continued.

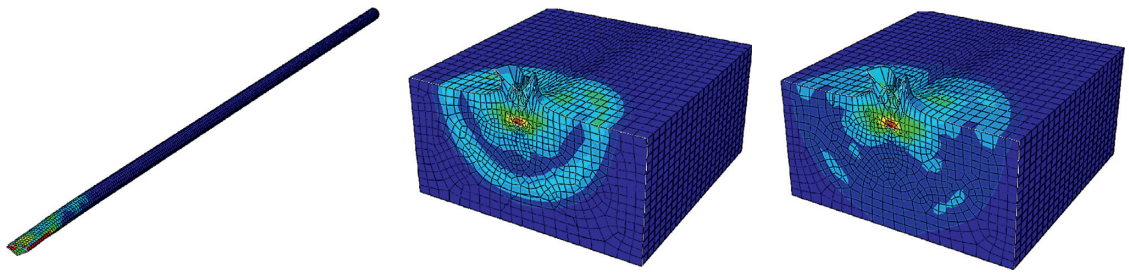

(d) (e) (f)

Figure 14: Propagation of the stress wave caused by the explosion in the soil and pipe environment.

Table 7: Specifications of models to investigate the effect of pipe burial depth.

Case	Soil type	Diameter (cm)	Thickness (mm)	Pipe pressure (Psi)	Depth (m)	W_{TNT} (kg)	Blast distance (m)
1	Clay				2		
2	Hard sand				2		
3	Soft sand				2		
4	Clay				3		
5	Hard sand				3	10	
6	Soft sand				3		
7	Clay				4		
8	Hard sand				4		
9	Soft sand				4		
10	Clay				2		
11	Hard sand				2		
12	Soft sand				2		
13	Clay				3		
14	Hard sand	100	14.3	250 (=1.732 MPa)	3	20	0
15	Soft sand				3		
16	Clay				4		
17	Hard sand				4		
18	Soft sand				4		
19	Clay				2		
20	Hard sand				2		
21	Soft sand				2		
22	Clay				3		
23	Hard sand				3	30	
24	Soft sand				3		
25	Clay				4		
26	Hard sand				4		
27	Soft sand				4		

due to the extraordinary velocity of the particles, but its value decreases as the seismic wave rises with increasing distance. Also, its quantity is never less than the seismic wave velocity [20]:

$$u = 48.8 \times f_c \left(\frac{2.52R}{w^{(1/3)}}\right)^{-n}, \tag{23}$$

$$\begin{aligned} P_0 &= \rho C u, \\ C &= c, \text{ (fully saturated clay soils)}, \end{aligned} \tag{24}$$

$$\begin{aligned} C &= 0.6c + \left(\frac{n+1}{n-2}\right)u, \text{ (saturated clay soils)}, \\ C &= c + \left(\frac{n+1}{n-2}\right)u, \text{ (sandy soils)}. \end{aligned} \tag{25}$$

Also, the time of continuous explosion compression on underground structures is obtained from equation (26) in which $i_0$is the specific momentum of the free zone, and placing the quantities of displacement and velocity of the particles in the above relation reaches the following relation for the time of total continuity equation (27). Inside the above relation, t_d transpires in seconds, R stands in meters, and C is in meters per second. However, to make modeling the analysis more comfortable, the reflection pressure drop has been omitted. The relationship of the blast pressure on the pipe in time has become

$$t_d = 2\frac{i_0}{P_0}, \tag{26}$$

$$i_0 = \rho C x, \tag{27}$$

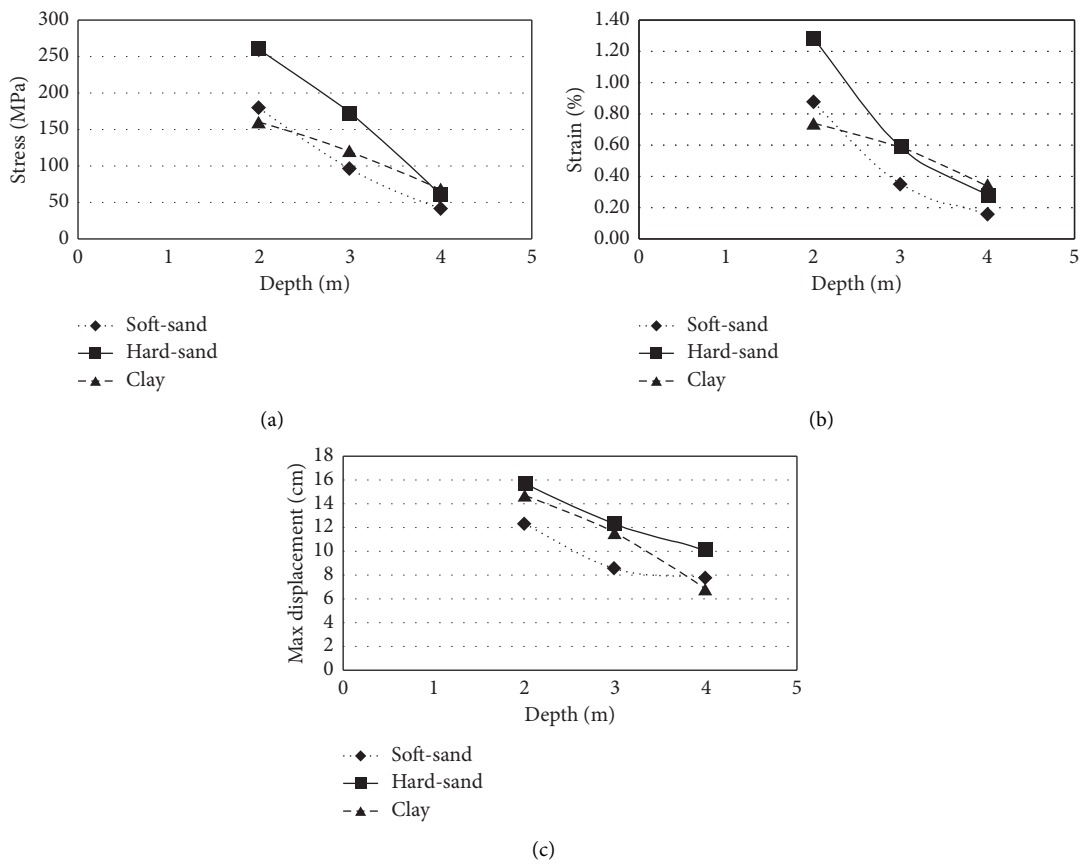

Figure 15: Analysis results to investigate the effect of pipe burial depth (explosion caused by 10 kg of TNT).

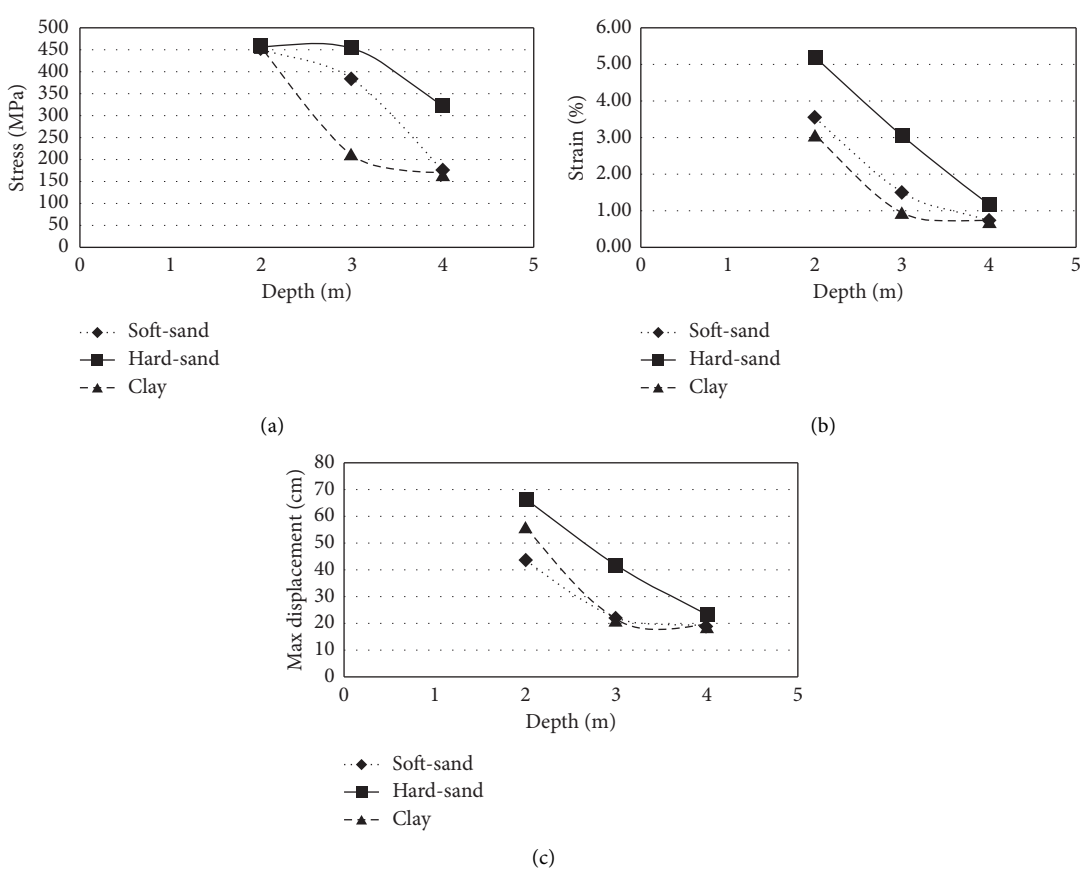

Figure 16: Analysis results to investigate the effect of pipe burial depth (explosion caused by 20 kg of TNT).

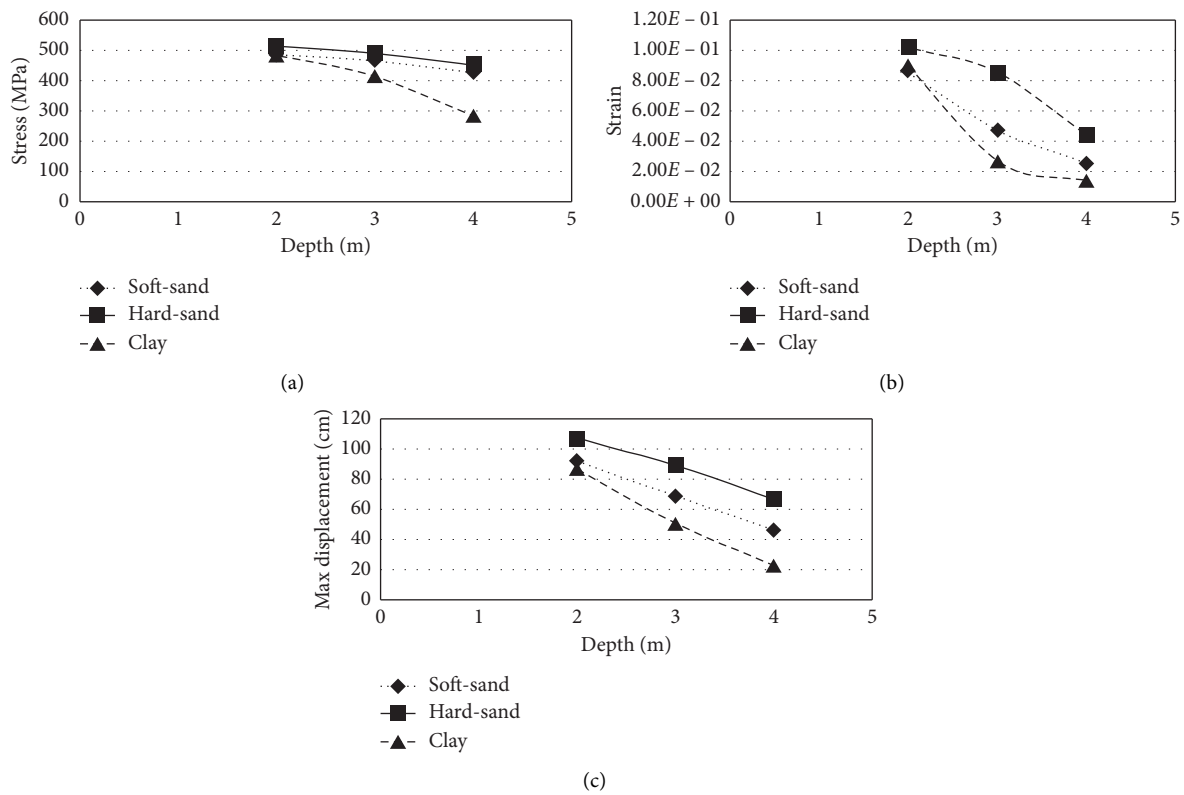

Figure 17: Analysis results to investigate the effect of pipe burial depth (explosion caused by 30 kg of TNT).

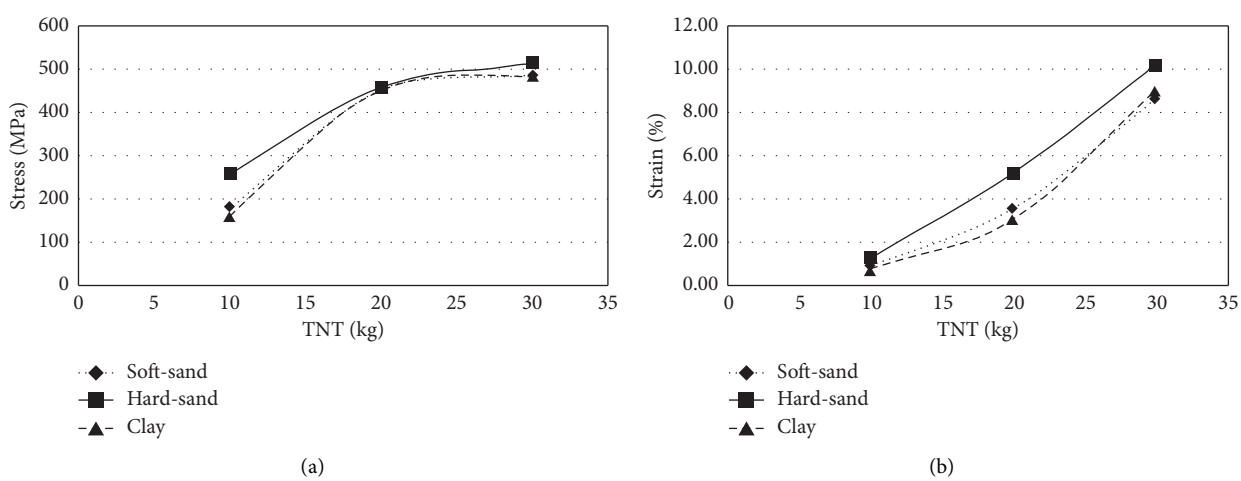

Figure 18: Continued.

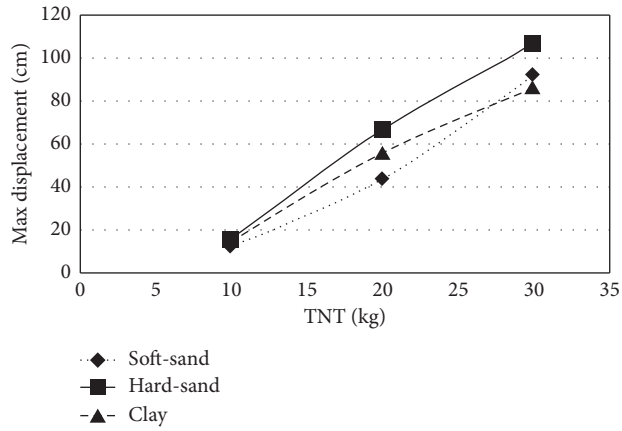

(c)

Figure 18: Analysis results to investigate the effect of explosive weight (pipe burial depth 2 meters).

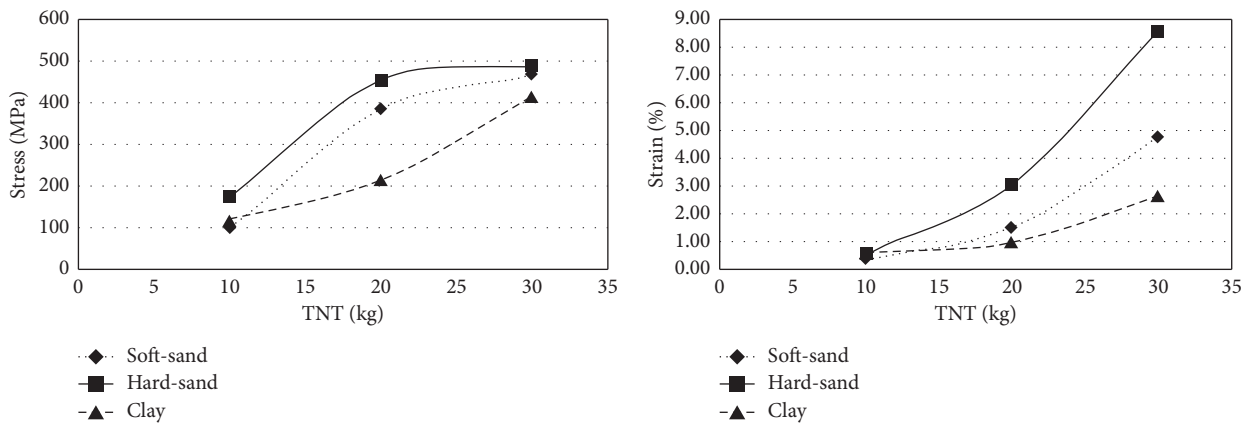

(a) (b)

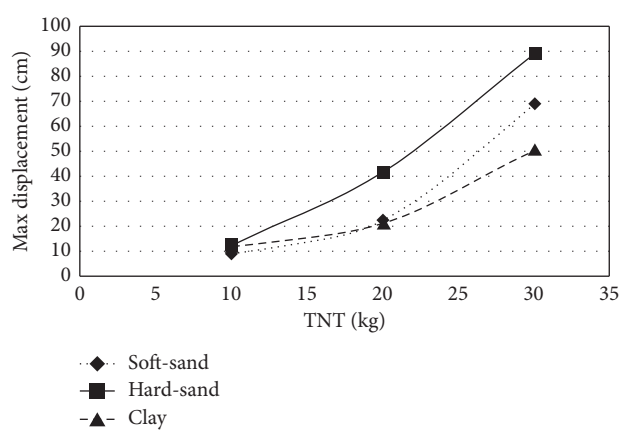

(c)

Figure 19: Analysis results to investigate the effect of explosive weight (pipe burial depth 3 m).

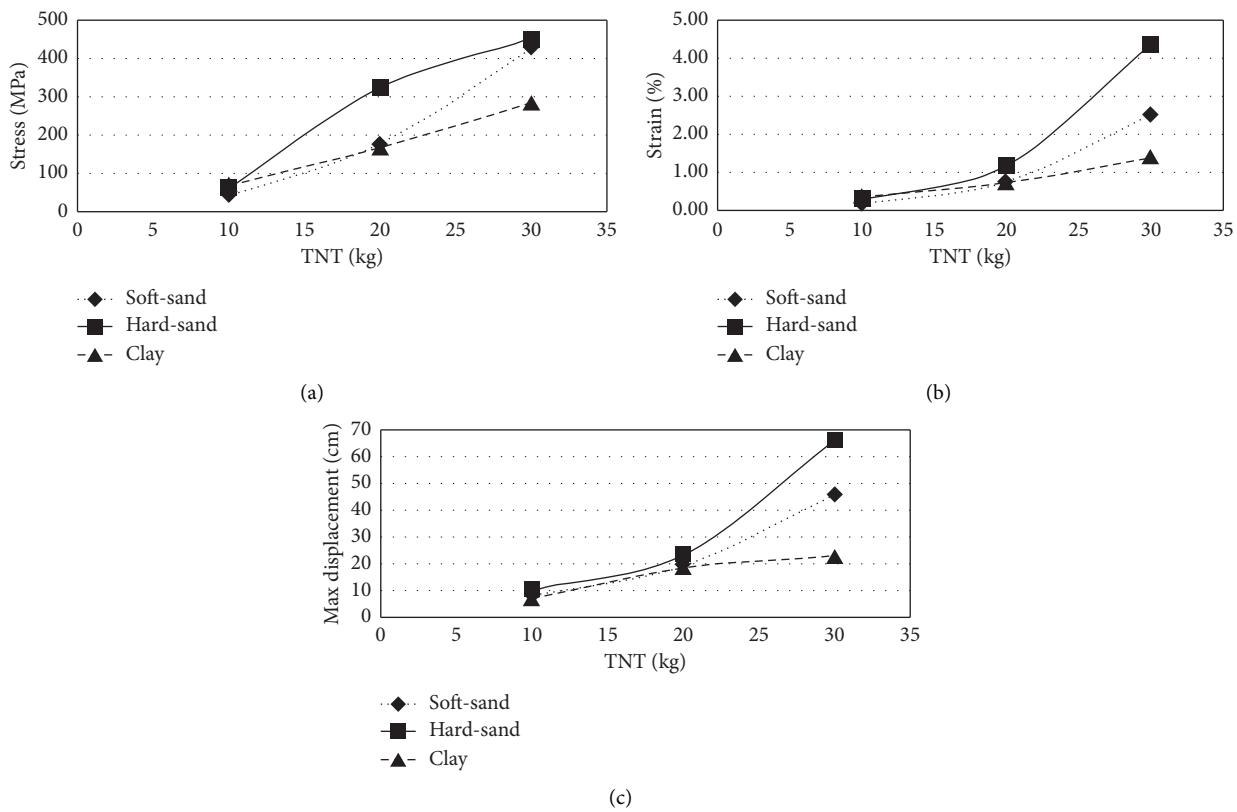

Figure 20: Analysis results to investigate the effect of explosive weight (pipe burial depth 4 m).

Table 8: Specifications of models to investigate the effect of explosive weight.

Case	Soil type	Diameter (cm)	Thickness (mm)	Pipe pressure (Psi)	Depth (m)	W_{TNT} (kg)	Blast distance (m)
1	Clay					10	
2	Hard sand					10	
3	Soft sand					10	
4	Clay					20	
5	Hard sand				2	20	
6	Soft sand					20	
7	Clay					30	
8	Hard sand					30	
9	Soft sand					30	
10	Clay					10	
11	Hard sand					10	
12	Soft sand					10	
13	Clay					20	
14	Hard sand	100	14.3	250 (=1.732 MPa)	3	20	0
15	Soft sand					20	
16	Clay					30	
17	Hard sand					30	
18	Soft sand					30	
19	Clay					10	
20	Hard sand					10	
21	Soft sand					10	
22	Clay					20	
23	Hard sand				4	20	
24	Soft sand					20	
25	Clay					30	
26	Hard sand					30	
27	Soft sand					30	

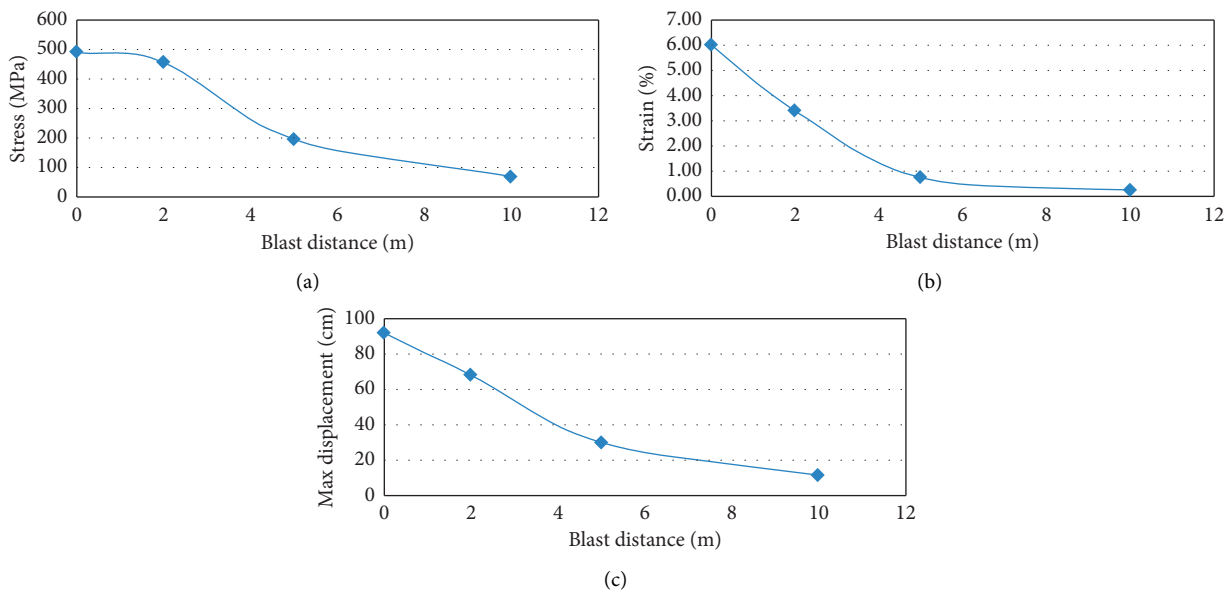

Figure 21: Analysis results to investigate the effect of blast distance from the pipe axis.

Table 9: Specifications of models to investigate the effect of explosion distance from the pipe axis.

Case	Soil type	Diameter (cm)	Thickness (mm)	Pipe pressure (Psi)	Depth (m)	W_{TNT} (kg)	Blast distance (m)
1							0
2	Soft sand	100	14.3	250 (=1.732 MPa)	3	20	2
3							5
4							10

Table 10: Specifications of models to investigate the effect of internal pipe pressure.

Case	Soil type	Diameter (cm)	Thickness (mm)	Pipe pressure (MPa)	Depth (m)	W_{TNT} (kg)	Blast distance (m)
1				0			
2	Soft sand	100	14.3	1.732 (=250Psi)	3	20	0
3				5			
4				10			

Table 11: Analysis results to investigate the effect of internal pipe pressure.

Pipe pressure	Max displacement (cm)	Stress (MPa)
No pressure	43.7	452
250 psi (=1.732 MPa)	43.7	452
5 MPa	43.6	452
10 MPa	43.6	452

Table 12: Specifications of models to investigate the effect of coefficient of friction between soil and pipe.

Case	Soil type	Diameter (cm)	Thickness (mm)	Pipe pressure (Psi)	Depth (m)	W_{TNT} (kg)	Friction coefficient
1							0.4
2							0.45
3	Soft sand	100	14.3	250 (=1.732 MPa)	3	20	0.5
4							0.55
5							0.6

Table 13: Analysis results to investigate the effect of coefficient of friction between soil and pipe.

Friction coefficient	Max displacement (cm)	Logarithmic strain	Stress (MPa)
0.4	22.19	%1.50	386
0.45	22.20	%1.50	391
0.5	22.22	%1.51	385
0.55	22.26	%1.51	386
0.6	22.30	%1.50	388

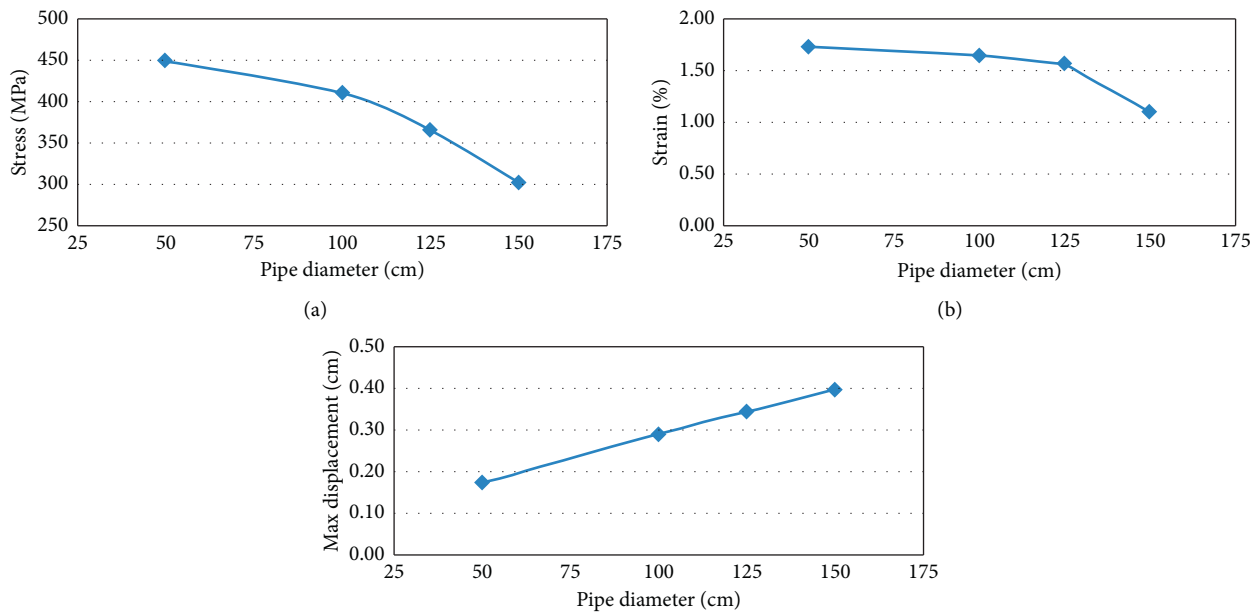

Figure 22: Analysis results to investigate the effect of pipe diameter.

Table 14: Specifications of models to investigate the effect of pipe diameter.

Case	Soil type	Diameter (cm)	Thickness (mm)	Pipe pressure (MPa)	Depth (m)	W_{TNT} (kg)	Blast distance (m)
1	Soft sand	50	14.3	1.732 (=250 Psi)	3	20	0
2		100					
3		125					
4		150					

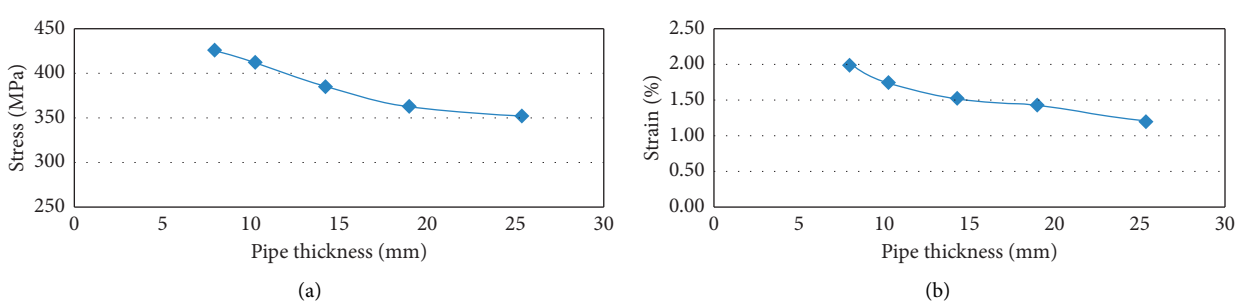

Figure 23: Continued.

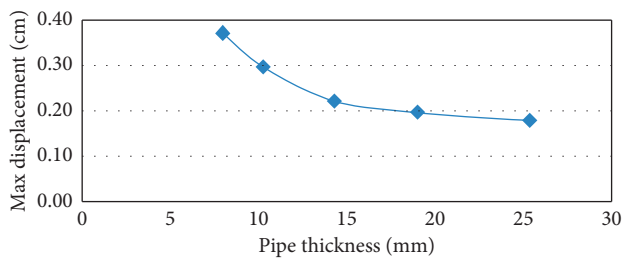

(c)

Figure 23: Analysis results to investigate the effect of pipe thickness.

Table 15: Specifications of models to investigate the effect of pipe thickness.

Case	Soil type	Diameter (cm)	Thickness (mm)	Pipe pressure (Psi)	Depth (m)	W_{TNT} (kg)	Blast distance (m)
1			8				
2			10.3				
3	Soft sand	100	14.3	250 (=1.732 MPa)	3	20	0
4			19				
5			25.4				

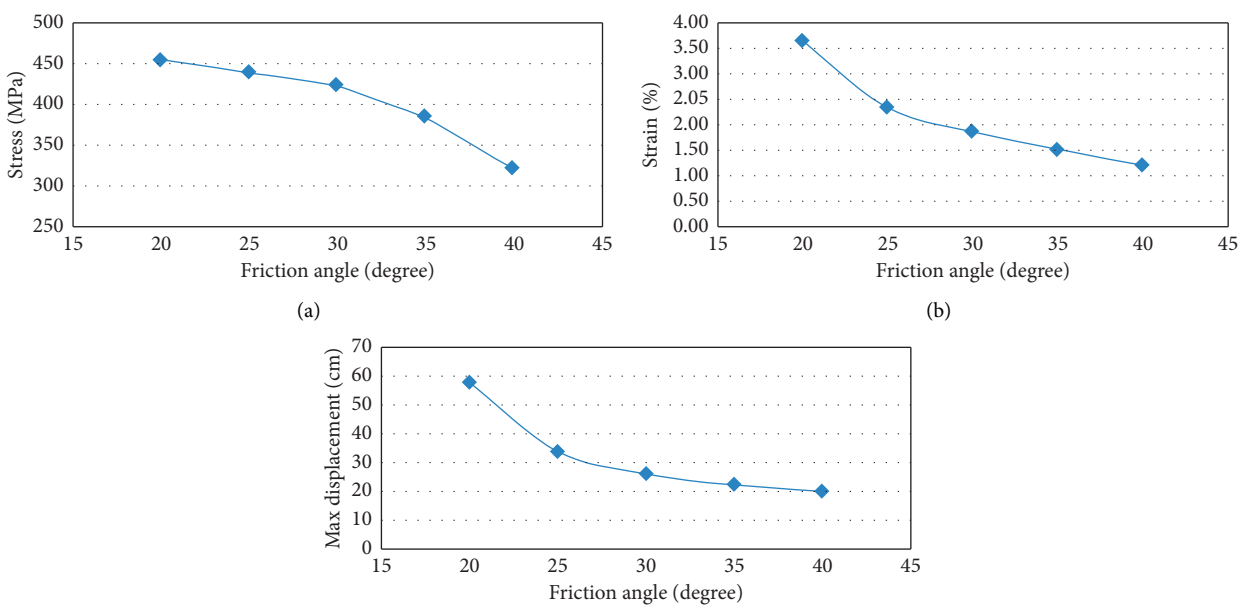

Figure 24: Analysis results to investigate the effect of internal soil friction coefficient.

Table 16: Specifications of models to investigate the effect of internal soil friction coefficient.

Case	Soil type	Diameter (cm)	Thickness (mm)	Pipe pressure (Psi)	Depth (m)	W_{TNT} (kg)	Friction angle
1							20
2							25
3	Soft sand	100	14.3	250 (=1.732 MPa)	3	20	30
4							35
5							40

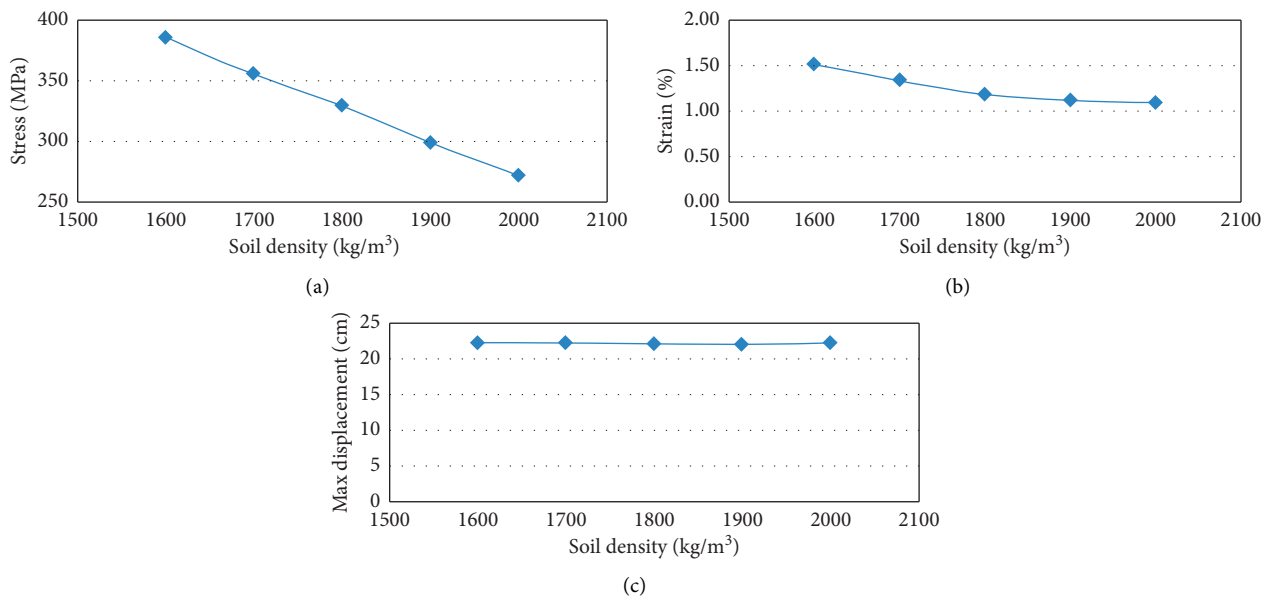

Figure 25: Analysis results to investigate the effect of soil specific gravity.

Table 17: Specifications of models to investigate the effect of soil specific gravity.

Case	Soil type	Diameter (cm)	Thickness (mm)	Pipe pressure (Psi)	Depth (m)	W_{TNT} (kg)	Soil density (kg/m³)
1							1600
2							1700
3	Soft sand	100	14.3	250 (=1.732 MPa)	3	20	1800
4							1900
5							2000

$$t_d = 6.1967\frac{R}{C}, \tag{28}$$

$$P(t) = P_r\left(1 - \frac{t}{t_d}\right). \tag{29}$$

3. Modeling and Conclusion

3.1. Sensitivity Analysis to Control Model Dimensions. Since the infinite soil environment is modeled in a finite form, the question arises about the dimensions of the soil model. Soil model dimensions should be chosen so that, while small, it has the least impact on the results; to minimize the time of analysis to get accurate results. Because the larger the model, the more accurate the results, but due to the larger dimensions of the model, the time of analysis is extended once the analysis of the model may take days. For this purpose, three models were made according to Table 4.

The above diagrams show the acceleration and wave velocity at the farthest node of the defined models (corner points) for the same loading and boundary conditions. According to this, it can be concluded based on obtained results (i.e., soil with dimensions of 50 100 100 × 25 m). The velocity and acceleration of the blast wave resulting from the explosion reaching the farthest node tend to zero. As the dimensions grow, only the analysis time increases, but there is no change in the results and outputs. Thus, the model that was considered for this project, according to the sensitivity analysis, is model 3, i.e., soil with dimensions of 100 × 50 × 25 meters, Figures 10 and 11.

3.2. Finite Element Model. The geometry of the model consists of two parts, soil and pipe. The dimensions of each are as follows: soil in the form of a cube with dimensions of 100 × 50 × 25 meters, and a steel pipe with a diameter of 1 meter, a length of 100 meters, and a thickness of 3/14 mm. After determining the geometry of the model, the specifications of the materials used should be defined. Soil and steel specifications are shown in Tables 5 and 6, respectively. For steel materials, the yield stress is equal to 0.5% strain, and ultimate tensile strength is equal to a 19% strain. The Drucker–Prager plastic model was also used to define soil behavior. All members are homogeneous. For pipe modeling, shell elements have been used, and for soil modeling, solid elements have been used.

Two methods can be applied in modeling soil-structure interaction. One is soil replacement modeling with springs in three directions (two directions perpendicular to the pipe and one direction tangent to the pipe). Another way is to build a full model, including soil, pipes, and their interaction in three dimensions. In this study, due to the closest

approximation to reality, the second method was utilized. In this modeling, the interaction between soil and pipe elements within the software is modeled on surface-to-surface mode, between the outer surface of the pipe and the inner surface of the soil and by the penalty method. In this method, the normal contact of two levels with the hard contact method is considered to prevent the surfaces from sinking into each other. Also, the tangential interaction of the two surfaces with a friction coefficient of 0.5 that was suggested by Vasouras and Kolbadi [21, 22] is regarded in the analyzes. This number is a suitable value for the interaction of soil with metal structures. However, in a part of the study, the effect of the quantity of this coefficient of friction on the behavior of the pipe was investigated, and the results are presented below. Also, at this level, damping contact was considered with a coefficient of 0.05.

Since the peripheral soil is semi-infinite, it must be modeled so that all its properties, including its being semi-infinity, are considered. Based on the previously performed sensitivity analysis (Figure 12), we saw that the velocity and acceleration of the blast wave that reaches the farthest node tend to zero [23, 24]. When the wave reaches the farthest nodes from all sides, it is damped. Therefore, there is no need to use energy absorbing and damping boundaries on the edges of the soil environment. Thus, symmetry conditions can be utilized on the lateral surfaces of the soil model without any challenges [25]. Of course, it should be noted that these conditions, i.e., not using adsorbent and damping boundaries on the lateral surfaces of the soil environment, are appointed just because of the type of loading, i.e., explosion, as well as the dimensions considered for this model, and cannot be generalized to other situations [26]. For example, the conditions for earthquake loading are different. If the adsorbent and damping boundaries are not used on the lateral surfaces of the soil environment, the wave reflected from the structure by these boundaries is reflected in the environment and causes errors in the results [27]. Therefore, absorbing boundaries must be applied to prevent the reflection of the waves. The soil floor also has encastre boundary conditions.

3.3. Loading. The loads applied to the pipe include the load due to the blast wave, the internal pressure of the pipe, and the overburden soil weight of the pipe. The blast load is applied as a compression-time series for an equivalent TNT mass of 10, 20, and 30 kg at a point on the soil based on the equations presented equation (22). The place of the surface load application was a hole dug in the shape of a hemisphere with a radius of 1 meter on the soil surface. The internal pressure of the pipe was also applied as a uniform pressure on the inner surface of the pipe. Nine-node cubic elements were used in meshing the soil volume, which is smaller in sensitive areas in Figure 13.

3.4. Type of Analysis. Knowing the nature of each of these methods and gaining experience will be simple to choose the solution. In the explicit method, the results at each moment $(x_n + 1)$ are obtained directly from the results before (x_n). In this way, new situations are calculated by considering the velocity and acceleration of the elements at the moment n and placing them in the following equation:

$$x_{n+1} = x_n + \Delta t_{n+(1/2)} \dot{x}_{n+(1/2)}. \tag{30}$$

On the other hand, in the implicit method, the size of Δt does not matter much. In this method, the equations of position (x_n), velocity (x_n), and acceleration (x_n) are solved simultaneously by iterative methods. In this way, there is no trace of speed and acceleration in the nodes. In high-speed physical phenomena, such as blast forces or collision forces that inflict a significant load on a structure in a short period, solver convergence is implicitly impossible. Besides, observation of the reaction of the structure in small time intervals is considered. The following is the process of spreading the stress wave propagation caused by the explosion in the soil and pipe under the blast load in Figure 14.

4. Review of Analysis Results

To analyze the sensitivity of the parameters affecting the performance of the pipe, the models and the results of their analysis are examined separately. The parameters that underlie the judgment are stress, strain, and displacement. The stress understudy is phonemic stress obtained from the square root of the sum of the principal stresses. Displacement also means the maximum absolute displacement of one of the pipe nodes.

4.1. The Impact of Pipe Burial Depth. Blast loading was performed on three types of soil (loose sand, hard sand, and clay) and its impact at three different depths. Depth of burial pipe tension, strain, and maximum displacement of the pipe is significantly reduced. The effect of increasing the burial depth of pipes on their behavior against explosion can be mentioned for various reasons, such as increasing the pipe blockage in the soil, increasing the distance of the pipe to the explosion place, and increasing the stiffness of the soil (Table 7). Therefore, it seems that the performance of buried pipes is better in clay soils and loose sands, respectively, especially with increasing pipe burial depth; this is evident. The phenomenon due to the higher seismic wave velocity in hard sandy soils is directly related to the modulus of elasticity of the soil and increases the blast wave maximum pressure (Figures 15–17).

4.2. The Impact of Explosive Weight. Based on the relations presented to calculate the mass charge, the weight of the mass charge directly affects the loads caused by the explosion. Therefore, according to the results obtained from the analysis of the models given in Figures 18–20, it can be stated that increasing the weight of charge mass, strain and maximum displacement of the pipe will increase. Here, too, the performance of pipes buried in loose soils and sands, particularly clay soils, seems to be better (Table 8).

4.3. The Impact of Blast Distance from the Pipe Axis. Based on the results obtained from the analysis of the models given in Figure 21, it can be said that by increasing the blast

distance, strain and maximum displacement of the pipe will be significantly reduced. This decreasing trend tends to zero after specific distances (depending on the conditions), where it occurs after a distance of 5 meters (Table 9).

4.4. The Impact of Internal Pipe Pressure. According to the results of the analysis of the models, which are given in Table 10 and 11, it can be said that the internal pressure has little impact on the pipe response practically.

4.5. The Impact of Friction Coefficient between Soil and Pipe. According to the analysis results, which are given within Tables 12 and 13, it can be recognized that practically, the friction coefficient between the soil and the pipe has a negligible impact on the pipe response, due to the propagation of the wave, which is perpendicular to the axis of the pipe. Hence, the impact it has on the pipe is more inclined to normal type than the contact. So, the normal interaction of soil and pipes is much more critical than their contact interaction.

4.6. Pipe Diameter Impact. As expected, the larger the diameter of the pipe, the better the pipe performance as the cross-sectional moment of inertia increases based on Figure 22 and Table 14.

4.7. Pipe Thickness Impact. As expected, the thicker the pipe, the better the performance of the pipe as the moment of inertia increases as can be found in Figure 23 and Table 15.

4.8. The Impact of Soil Internal Friction Coefficient. Based on the results obtained from the analysis of the models given in Figure 24, it can be stated that by increasing the internal friction coefficient of the soil, the maximum strain and displacement of the pipe decrease (Table 16).

4.9. Soil Specific Gravity Impact. Based on the results of the analyzes given in Figure 25, it can be understood that by increasing the specific gravity of the soil, the maximum stress and strain of the pipe are significantly reduced (Table 17). However, there is no noticeable change in maximum pipe displacement.

5. Conclusions

Summary of the achievements of studying the performance of buried pipelines under the effect of explosive loading is presented in this section. Then, based on the author's experience, to reduce ambiguities, conduct experiments, furthermore analyze some of the obtained results, and also present a series of suggestions and approaches for using the results of this research, some ideas are mentioned in the suggestions section.

As can be seen, from the problem under study, first, a suitable model was constructed in three-dimensional form using the finite element method. Then, in the analysis, by changing the parameters that seemed to be important in the behavior of the pipe under the effect of the surface explosion, we examined the sensitivity of the pipe response to the change of the desired parameter. After analyzing and extracting the results, these results were presented in charts, which were based on judgments and conclusions about pipe behavior. At the end of the analysis used in this study, results were obtained to understand better the behavior and optimal design of buried pipelines under the impact of surface explosions, which are mentioned as follows:

(1) Blast wave arrival velocity depends on the velocity of the soil environment compressive seismic wave. The arrival time of the wave in clay soils is longer than other soils. The blast wave response time to the structure is a significant factor for the response of underground structures such as buried pipes.

(2) Due to the low mass of the pipe and the high dependence of its behavior on the strains that occur in the surrounding soil, it can be stated that the entering velocity spectrum of the pipe is much more critical than the acceleration spectrum.

(3) As the pipe depth increases, the maximum stress, strain, and displacement of the pipe decrease almost linearly. Buried pipes seem to perform better in clay soils and loose sands, respectively, especially while the burial depth of the pipe increases. The reason is that this phenomenon is the higher seismic wave velocity in stiff sandy soils, which is directly related to the modulus of soil elasticity and increases the maximum blast wave compression.

(4) By increasing the blast distance from the tension pipe axis, the maximum strain and displacement of the pipe are significantly reduced. This decreasing trend tends to zero after specific distances (according to environmental conditions, pipes, and explosions); here, it has occurred after 5 meters.

(5) The internal pressure of the pipe and the coefficient of interaction friction between the soil and the pipe have a negligible effect on the response of the pipe.

(6) The larger the diameter and thickness of the pipe, the better the performance of the pipe with increasing the cross-sectional moment of inertia. The relation between the results and the conversions in these parameters is approximately linear.

(7) By increasing the coefficient of internal friction of the soil, the maximum strain and displacement of the pipe decrease. The effectiveness of this parameter is significant compared to other parameters.

(8) While the specific gravity of the soil increases, the maximum pipe stress and strain decrease considerably, but there is no noticeable change in the maximum pipe displacement.

(9) According to the previous results, in the case of buried shell structures, such as pipes, it can be understood that their performance is more affected by the deformation of the structure (such as pipe

bending) than the effects of soil-structure interaction.

Data Availability

The data used to support the findings of this study are available from the corresponding author upon reasonable request.

Conflicts of Interest

The authors declare that there are no conflicts of interest regarding the publication of this paper.

Acknowledgments

The authors of this article are grateful for the valuable guidance of Mr. Abbas Aghasi.

References

[1] A. S. Abedi, N. Hataf, and A. Ghahramani, "Analytical solution of the dynamic response of buried pipelines under blast wave," *International Journal of Rock Mechanics and Mining Sciences*, vol. 88, pp. 301–306, 2016.

[2] K. Wang, Z. Liu, X. Qian, and Y. He, "Dynamic characteristics and damage recognition of blast-induced ground vibration for natural gas transmission pipeline and its integrated systems," *Mechanical Systems and Signal Processing*, vol. 136, Article ID 106472, 2020.

[3] C. Shi, Q. Zhao, M. Lei, and M. Peng, "Vibration velocity control standard of buried pipeline under blast loading of adjacent tunnel," *Soils and Foundations*, vol. 59, no. 6, pp. 2195–2205, 2019.

[4] V. R. Kiran and P. Manoj, "Mechanical analysis of buried gas pipe line of different grades of steel at a depth under the influence of sub-surface blast loading," 2018.

[5] K. Song, Y. Long, C. Ji, F. Gao, and H. Chen, "Experimental and numerical studies on the deformation and tearing of X70 pipelines subjected to localized blast loading," *Thin-Walled Structures*, vol. 107, pp. 156–168, 2016.

[6] L. Ni, J. Lang, and L. Chen, "Numerical simulation on the dynamic response of submarine pipelines under blast loading," *Oil & Gas Storage and Transportation*, vol. 2, p. 17, 2018.

[7] S. Stanković, V. Škrlec, and M. Dobrilović, "Influence of blast-induced ground vibrations on buried transmission pipelines," in *Proceedings of the Seventh International Conference on Advances in Civil, Structural and Mechanical Engineering-CSM*, Rome, Italy, December 2018.

[8] J. Zhang, L. Zhang, and Z. Liang, "Buckling failure of a buried pipeline subjected to ground explosions," *Process Safety and Environmental Protection*, vol. 114, pp. 36–47, 2018.

[9] M. Bai, X. Xu, H. Yang et al., "Safety evaluations of a large-scale facility under blast loading," *Journal of Vibroengineering*, vol. 22, no. 4, pp. 849–867, 2020.

[10] L. Chernin, M. Vilnay, and I. Shufrin, "Blast dynamics of beam-columns via analytical approach," *International Journal of Mechanical Sciences*, vol. 106, pp. 331–345, 2016.

[11] H. Jiang, T. Xu, and D. Zhao, "Dynamic response and limit analysis of buried high-pressure gas pipeline under blasting load based on the Hamilton principle," *Journal of Vibroengineering*, vol. 19, no. 1, pp. 376–393, 2017.

[12] E. Giannaros, T. Kotzakolios, and V. Kostopoulos, "Blast response of composite pipeline structure using finite element techniques," *Journal of Composite Materials*, vol. 50, no. 25, pp. 3459–3476, 2016.

[13] Y.-G. Wang, C. C. Liao, and J. H. Wang, "Numerical investigation of pore pressure effect on blast-induced pipeline-seabed interaction," *Applied Ocean Research*, vol. 77, pp. 61–68, 2018.

[14] P. Vivek, T. G. Sitharam, G. Jagadeesh, and K. P. J. Reddy, "Response of embedded pipeline to surface blast loading," in *Proceedings of the 30th International Symposium On Shock Waves 1*, pp. 749–754, Tel-Aviv, Israel, August 2017.

[15] A. H. I. Sigiuk, "Development of an instantaneous frequency estimation pipeline for compressional and shear wave arrival picking," in *Application to Quarry Blast Data*University of British Columbia, Vancouver, Canada, 2019.

[16] N. Jiang, T. Gao, C. Zhou, and X. Luo, "Effect of excavation blasting vibration on adjacent buried gas pipeline in a metro tunnel," *Tunnelling and Underground Space Technology*, vol. 81, pp. 590–601, 2018.

[17] L. Zardasti, N. Yahaya, A. Valipour, A. S. A. Rashid, and N. M. Noor, "Review on the identification of reputation loss indicators in an onshore pipeline explosion event," *Journal of Loss Prevention in the Process Industries*, vol. 48, pp. 71–86, 2017.

[18] D. Zhong, X. Gong, F. Han, and L. Li, "Monitoring the dynamic response of a buried polyethylene pipe to a blast wave: an experimental study," *Applied Sciences*, vol. 9, no. 8, p. 1663, 2019.

[19] P. Vivek and T. G. Sitharam, "Response of embedded structures in granular material to air-blast wave loading," in *Granular Materials Under Shock and Blast Loading*Springer, Berlin, Germany, 2020.

[20] K. Wang, T. Shi, Y. He, M. Li, and X. Qian, "Case analysis and CFD numerical study on gas explosion and damage processing caused by aging urban subsurface pipeline failures," *Engineering Failure Analysis*, vol. 97, pp. 201–219, 2019.

[21] P. Vazouras, S. A. Karamanos, and P. Dakoulas, "Mechanical behavior of buried steel pipes crossing active strike-slip faults," *Soil Dynamics and Earthquake Engineering*, vol. 41, pp. 164–180, 2012.

[22] S. M. S. Kolbadi, N. Hassani, and M. Safi, "Numerical evaluation on improvement performance of waved connection to reduce damage on buried gas pipeline," *Shock and Vibration*, vol. 2020, Article ID 6680384, 17 pages, 2020.

[23] M. Mirtaheri, S. Sehat, and M. Nazeryan, "Improving the behavior of buckling restrained braces through obtaining optimum steel core length," *Structural Engineering and Mechanics*, vol. 65, pp. 401–408, 2018.

[24] R. K. Mohammadi, M. Mirjalaly, M. Mirtaheri, and M. Nazeryan, "Comparison between uniform deformation method and Genetic Algorithm for optimizing mechanical properties of dampers," *Earthquakes and Structures*, vol. 14, pp. 001–010, 2018.

[25] S. M. Seyed Kolbadi, H. Piri, A. Keyhani, S. M. Seyed-Kolbadi, and M. Mirtaheri, "Nonlinear seismic performance evaluation of flexural slotted connection using endurance time method," *Shock And Vibration*, vol. 2020, Article ID 8842230, , 2020.

[26] S. M. S. Kolbadi and H. Davoodian, "Evaluation of nonlinear behavior of reinforced concrete frames by explosive dynamic loading using finite element method," *Civil Engineering Journal*, vol. 3, pp. 12–20, 2017.

[27] S. Mohammad, S. Kolbadi, N. Hassani, S. M. S. Kolbadi, and M. R. Shiravand, "Effect of ground motions on nonlinear seismic behavior of corroded buried gas pipeline," *American Journal of Civil Engineering*, vol. 3, pp. 9–13, 2015.